3 - Dimensional Simulation of Collective Effects in Particle Accelerators

Andreas Wagner

3-Dimensional Simulation of Collective Effects in Particle Accelerators

these (all eng)

Dissertation zur Erlangung des akademischen Titels
Doktor der technischen Wissenschaften

Vorgelegt der Technisch-Naturwissenschaftlichen Fakultät
der Technischen Universität Graz

Durchgeführt am europäischen Kernforschungszentrum
CERN, CH-1211 Genf, und am Institut für Theoretische
Physik der TU-Graz, A-8010 Graz,

von

Andreas Wagner

Genf und Graz, am 30. Oktober 1997

Abstract

3-Dimensional Simulation of Single Bunch Collective Effects in Particle Accelerators

Collective effects due to the impedance of structures along the vacuum chamber of particle accelerators and storage rings can limit their performance by deteriorating the quality of the beam. In particular in LEP (the CERN Large Electron Positron collider), transverse impedances are restricting single bunch currents in the vertical direction, but also - to a somewhat lesser degree - in the horizontal one. All such previous simulation programs have taken into account only a single transverse dimension.

The 3-dimensional, single-bunch tracking program TRISIM3D was developed, based on its predecessor TRISIM. It allows for the effects of wake potentials in all 3 spatial dimensions, and uses triangular basis functions to represent the particle distribution. The wake potential tables for those basis functions, used as input for TRISIM3D, can in general be precalculated with mesh-programs.

The properties of wake potentials in non-axially symmetric structures were studied intensively. In addition to the dipole wake field, which yields the major transverse contribution in axially symmetric structures, there is also a quadrupole component for those which have no axial symmetry. The major rotationally non-symmetric contributions in LEP, come from the shielded bellows, which are installed in the arc-sections, and from the electrostatic separators, and were computed numerically.

The wake potentials of the LEP structures, which were studied, could only be calculated for bunch lengths which are too long to be used in TRISIM3D. Therefore a novel method (*"Decomposition Method"*) was developed, which allows to calculate the wake potentials of shorter bunches from those of longer ones.

Results of 3-D simulations of LEP, including the effects of the wake potentials for 3-D structures, are presented. The effect of horizontal-vertical coupling in LEP due to wake potentials was investigated and found to be weaker than that due to skew quadrupoles and solenoids. The frequency shifts of horizontal and vertical beam oscillations have a ratio corresponding to measurements, while the somewhat low absolute values of this *tune-shifts* are due to the omission of the resistive wall impedance.

Zusammenfassung

3-Dimensionale Simulation von Kollektiven Effekten von einzelnen Teilchenbündeln in Ringförmigen Teilchenbeschleunigern

Kollektive Effekte durch die Impedanz von Strukturen entlang der Vakuumkammer können den Arbeitsbereich von Teilchenbeschleunigern und Speicherringen begrenzen indem sie die Strahlqualität verschlechtern. Im speziellen in LEP (CERN's Large Electron-Positron Kollisionsmaschine) beschränkt die transversale Impedanz die Intensität von einzelnen Teilchenbündeln (Bunche) in der vertikalen, aber auch - zu einem etwas geringeren Grad - in der horizontalen Richtung. Alle vorhergehenden Simulationsprogramme haben nur eine transversale Dimension berücksichtigt.

Das 3-dimensionale, Einzel-Bunch, Tracking-Programm TRISIM3D wurde neu entwickelt; es basiert auf dem 2-dimensionalen Vorgängerprogramm TRISIM. Das Feld, das der geladene Strahl erzeugt, wird von ihn umgebenden Strukturen der Vakuumkammer, Hohlräume, Bälge usw., verändert; diese Änderungen werden durch Wake-Potentiale (=Kielwasser-Potentiale) beschrieben. TRISIM3D berücksichtigt die Effekte von solchen Wake-Potentialen in allen 3 räumlichen Dimensionen und verwendet dreieckige Basisfunktionen um die Teilchenverteilung zu beschreiben. Die Tabellen der Wake-Potentiale für diese Basisfunktionen, welche als Eingabe für TRISIM3D dienen, können im allgemeinen mit Programmen der finiten Integration der Feldgleichungen auf Gittern (MAFIA und ABCI) im voraus berechnet werden.

Die Eigenschaften von Wake-Potentialen in nicht axialsymmetrischen Strukturen werden eingehend studiert. Zusätzlich zu den Dipol Wake-Feldern, welche den Hauptbeitrag in transversaler Richtung in zylindersymmetrischen Strukturen liefern, gibt es auch eine Quadrupolkomponente für Strukturen ohne Axialsymmetrie. Die nicht axialsymmetrischen Hauptbeiträge in LEP kommen von den abgeschirmten Bälgen, welche in den Bogensektionen installiert sind, und von den elektrostatischen Separatoren, und wurden numerisch berechnet.

Die Wake-Potentiale der untersuchten LEP-Strukturen konnten nur für Bunchlängen berechnet werden, welche zu lang sind um in TRISIM3D direkt verwendet zu werden. Deshalb wurde eine neue Methode (Zerlegungsmethode, "Dekompositionsmethode") entwickelt, welche es erlaubt die Wake-Potentiale kürzerer Bunche aus denen längerer zu berechnen.

Resultate von 3-dimensionalen Simulationen von LEP, unter Berücksichtigung der Effekte der Wake-Potentiale, werden präsentiert. Der Effekt der horizontal-vertikalen Kopplung durch Wake-Potentiale in LEP wurde untersucht; es ergab sich, daß jene kleiner ist als die Kopplung durch verdrehte Quadrupole und Solenoide. Das berechnete Verhältnis der Frequenzänderung der horizontalen und vertikalen Bunchoszillationen (Tune-Shift) stimmt mit der gemessenen überein; während die etwas niedrigen Absolutwerte dieser Frequenzänderungen auf die Vernachlässigung der Impedanz der widerstandsbehafteten Wand ("Resistive Wall") zurückzuführen sind.

Acknowledgements

The author would like to thank his university supervisor Prof. Bernhard Schnizer of the Institut für Theoretische Physik, TU-Graz, and his CERN supervisor Dr. Bruno Zotter, of the SL Divison, Accelerator Physics group, for their guidance of this thesis, for their helpfulness, patience and for many fruitful discussions. He would also like to thank all the members of the AP group, especially Jaques Gareyete, for their hospitality.

Contents

Chapter 1

Introduction

Particle accelerators and storage rings cover a wide range of applications, from purely scientific to medical and industrial ones. Their layout and operational energy may differ widely depending on their purpose, but the fundamental principles of their operation are always the same. Charged particles are moving in electro-magnetic fields which keep them on the desired trajectory, and RF-fields provide the energy needed to accelerate them to the design energy. The particles must be moving in a highly evacuated chamber, in order to avoid collision with molecules of the rest gas, which could lead to blow-up and beam loss.

Usually it is of interest to maximise the number of particles in these machine in order to optimise their performance. Fields are induced by the charged particles in their environment, which are called wake fields. They limit the number of particles and can even cause instabilities. In addition to analytical studies of such *collective effects*, simulation programs have become a valuable tool to investigate them, and their dependence on various parameters. Such studies can be used e.g. to find the optimum working point or to study feed-back systems. Although many simplifications must be made to construct an accelerator model which can be studied with simulation techniques, in general they do not strongly influence the simulation results. The number of structures in an accelerator is usually too high to consider each of them separately, hence one concentrates their effects into fewer elements for an appropriate machine model. Also the number of particles in the accelerator has to be represented by a smaller number of macro-particles, each one consisting of a large number of real particles.

The wake fields induced by a bunch result in kicks on the particles which disturb their trajectories and distribution. An exact solution of this problem

is not possible in a simulation program, since the numerical computation of wake potentials is not fast enough to be repeated at every passage of a bunch through a structure. A possible way to avoid this problem is to expand the distribution into a suitable set of basis functions for which the wake potentials can be precalculated. The wake potential of the actual distribution can then be obtained rapidly from the wake potentials of these basis functions.

An efficient technique to represent the particle distribution by a set of triangular-shaped basis functions[Sab95a], and the steadily increasing performance of computer systems made the development of a 3-dimensional simulation program practical. In order to take the interaction between beam and its environment (vacuum chamber components) properly into account, the fields induced in the various components of an accelerator have to be studied carefully.

The numerical calculation of wake potentials is usually done with mesh - programs. To describe large 3-dimensional structures with a Cartesian mesh with sufficient accuracy one needs typically several million mesh cells. One also should have several mesh lines per characteristic length of the particle distribution in the longitudinal direction. Due to the limitations of available computer resources one cannot make the number of mesh cells arbitrary high, which limits the number of mesh cells in the transverse directions which would be needed to describe the structure with sufficient precision. Also the CPU time for the calculations has to stay within a reasonable range. Taking these requirements into account, the computer resources presently available at CERN allow the calculation of bunch lengths not shorter than 5 mm r.m.s. for Gaussian profiles in the various structures of LEP, the Large Electron-Positron collider at CERN. However, the length of the triangular bunches needed as input for the simulation program is typically 3 to 6 mm. Since the calculation of their wake fields would require even smaller meshes than for Gaussian bunches, a novel method was developed which permits to obtain the wake potentials of shorter distributions from longer ones. We called this the *"Decomposition Method"* which is described in chapter 3.

To understand the fundamental behaviour of wake fields in structures without axial symmetry, a number of some simple geometries have been examined first: "pillbox" cavities with side tubes of circular, quadratic, elliptic and rectangular cross-sections. The wake fields of those 3-dimensional structures were calculated numerically. The main axially non-symmetric structures of LEP, which contribute strongly to the impedance, are the shielded bellows with oval cross section. They have only minor cross section variations, but since they have a small vertical height, and there are a vary large number of them, they contribute significantly to the transverse impedance. Another type of element

without axial symmetry are the electro-static separators consisting of pairs of parallel plates in large tanks. In order to understand the influence of such structures on the motion of the particles, their wake fields have been studied in detail, and the results of these computations are shown in chapter 4.

The 3-dimensional multi-particle tracking program TRISIM3D is based on its predecessors SIMTRAC[Bra84], HERSIM[Nys87], HERSIM2[Wan90] and TRISIM[Sab94b, Sab95a, Sab95b]. The equations of motion used to describe the motion of the particles are presented in chapter 5. The wake field effects are included by expanding the particle distributions into triangular shaped basis functions in all 3 spatial directions. The wake field tables for rotationally symmetric structures have been calculated previously, while those for the unsymmetric structures, were obtained by the decomposition method. Several results of applications of the new program TRISIM3D are shown in chapter 6. However, the main focus of the present thesis is the calculation of wake potentials of non-axially symmetric structures, and their implementation in the simulation program.

Chapter 2

Collective Effects in Particle Accelerators

Here we want to give a short overview of the basic dynamics of particles in high energy accelerators. This field is known as *"accelerator physics"* and includes the study of a particle in the electromagnetic fields used to guide and focus the beams. In particular the effects of non-linearities and resonances can severely limit the parameter space available. However, in this thesis we are concerned with the interactions of the particles with others in the same bunch, usually transmitted through *"wake fields"* excited by particles of the head of the bunch, moving with speeds close to light velocity in the surrounding structures. Such interactions are called *"collective effects"* since they are due to a large number of single particles, and in particular *"coherent"* when their effects are in phase.

2.1 Wake fields, wake potentials, and loss factors

In this section we will introduce the concept of wake potentials, impedances and some related quantities, as far as necessary for the understanding of the present thesis. It is not meant to be exhaustive, for a more detailed and complete description the reader is refered to the literature [Cha93, KZ97].

2.1.1 Wake fields and wake potentials

When traversing the vacuum chamber, a particle beam induces electromagnetic fields wherever the cross-section of the chamber changes. The *wake fields* of an ultra-relativistic[1] bunch can interact with particles of a following bunch or even with the trailing particles of the exciting bunch itself. In cavity-like structures the beam will excite resonant frequencies also called *resonant modes*, which can cause significant energy loss of the beam.

The field lines in a simple "pillbox" like structure with side tubes, excited by a bunched beam with a Gaussian longitudinal profile, are shown in Figure 2.1 for several consecutive time steps, calculated with the mesh-program ABCI [Chi94]. It is assumed that the walls of the cavity are ideal conductors, and that the beam travels with the speed of light. In vacuum, the electric field lines of the beam would be straight lines pointing radially outwards. In the presence of a conducting boundary, the field lines are distorted towards the wall.

Due to such wake fields, a trailing particle experiences a force depending on its spatial position. This *wake force* $\mathbf{F}$ is in general a complicated function of time and position. For charged particles, which move with a speed near to light velocity, the trajectory of the average particle motion remains undisturbed by the wake force. It is therefore useful to introduce the integral over the wake force along the trajectory.

$$\mathbf{W}(\mathbf{r}, \bar{\mathbf{r}}, s) = \int_0^l \mathbf{F}(\mathbf{r}, \bar{\mathbf{r}}, s, z) dz \,, \tag{2.1}$$

where s is the longitudinal distance from the exciting charge, and $\mathbf{r}$ and $\bar{\mathbf{r}}$ are the transverse positions of source and test charges.

The integral over the wake force due to fields excited by a point charge or delta function distribution, normalised by the charge q, is called the *wake function* Since it is also the Green's function for the geometry considered, we call it $G(s)$. The *longitudinal wake function* $\mathbf{G}_{\|}$ is given by

$$G_{\|}(\mathbf{r}, \bar{\mathbf{r}}, s) = -\frac{1}{q} \int_{-\infty}^{\infty} E_z(\mathbf{r}, \bar{\mathbf{r}}, t = \frac{z - s}{c}, z) dz \,. \tag{2.2}$$

[1]The ultra-relativistic assumption is certainly a reasonable approximation for high energy electron machines, e.g. in LEP where $v/c = 1 - 2.7 \cdot 10^{-10}$ at the injection energy of 22 GeV, and even closer to unity at the higher operational energies.

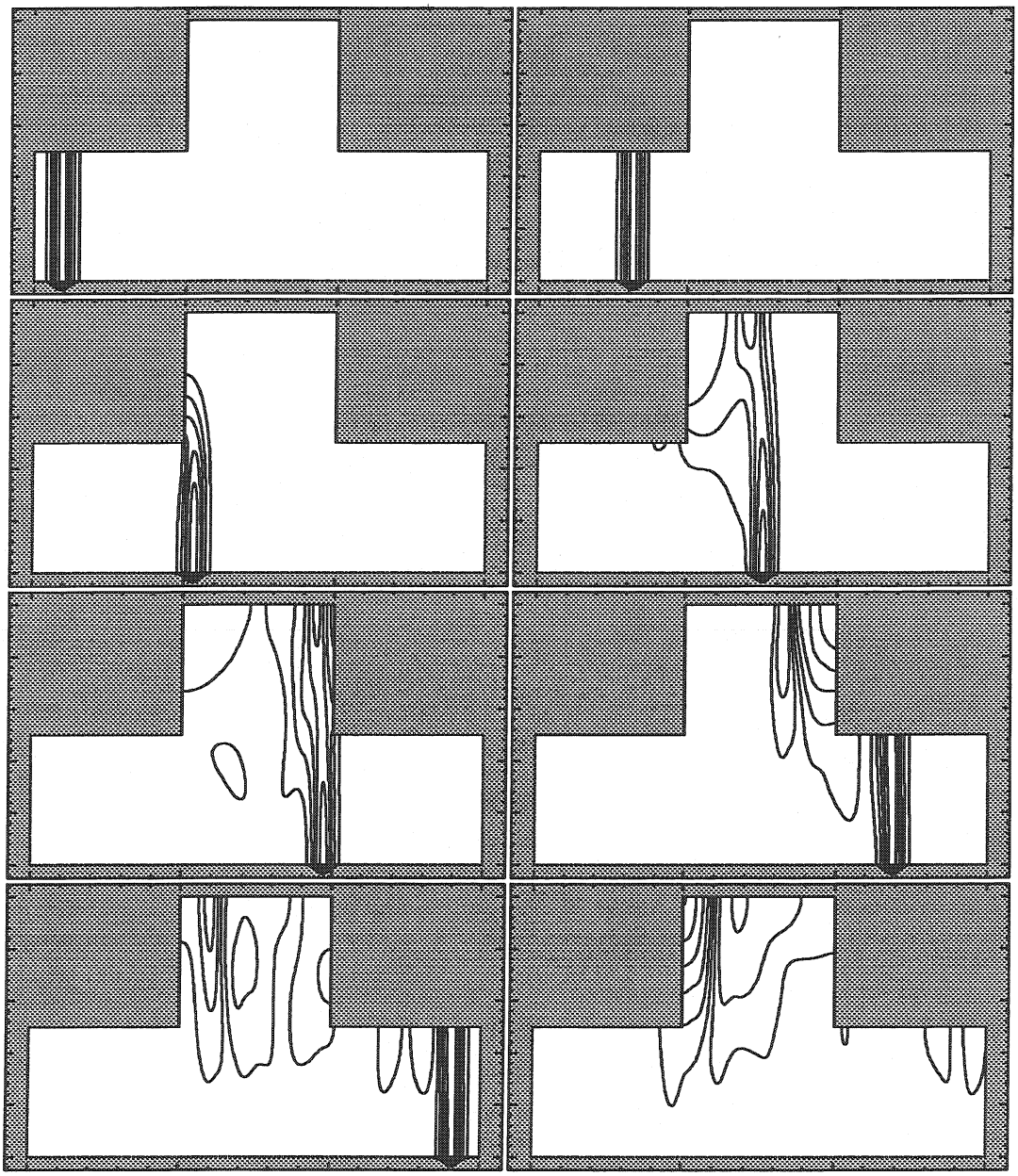

Figure 2.1: Electric field lines in a "pillbox" cavity with side tubes, induced by a passing Gaussian charge distribution.

where E_z is the electric field component in direction of the particle propagation. There is no contribution of the magnetic force, since it is at a right angle to the direction of the particle motion. The minus sign makes the wake function

positive when it has a decelerating effect. A trailing particle with charge e behind a point charge q will experience an energy loss

$$\Delta E(s) = e\,q\,\mathrm{G}_{\|}(s). \tag{2.3}$$

When the exciting charge distribution has a finite length, the *longitudinal wake potential* is given by the convolution of the longitudinal wake function with the normalised line charge density $\lambda(s)$ of the distribution

$$W_{\|}(s) = \int_0^{\infty} G_{\|}(s-z)\lambda(z)dz. \tag{2.4}$$

The longitudinal wake potential has dimensions V/C.

Analogous to the longitudinal one, the *transverse wake function*, can be defined as the integral over the transverse electro-magnetic force along a straight path at a distance s behind an exciting point charge travelling with constant velocity $v \approx c$

$$G_{\perp}(s) = \frac{1}{q}\int_{-\infty}^{z} (\mathbf{E} + \mathbf{v} \times \mathbf{B})dz\,. \tag{2.5}$$

Here $\mathbf{E}$ and $\mathbf{B}$ are the electric and the magnetic fields, and $\mathbf{v}$ the particle velocity vector. If the transverse wake function is known, the *transverse wake potential* can be found as its convolution with the particle distribution.

$$W_{\perp}(s) = \int_0^{\infty} G_{\perp}(s-z)\lambda(z)dz. \tag{2.6}$$

Using this definition, the transverse wake potential also has the dimensions V/C. However, since the transverse wake potential in axially symmetric structures is dominated by the dipole moment (m=1), it is quite common to redefine the transverse wake function and potential as normalised by the dipole moment of the distribution. Their units become then V/Cm.

In rotationally symmetric structures, the transverse wake potentials always deflect a transversely displaced particle near the source further outwards, its effect is therefore always defocusing. If a structure is non-axially symmetric, the transverse wake potential can also have a focusing effect in one of the transverse directions.

2.1.2 Loss factor

To simplify the calculation of the energy lost by bunched beams passing through vacuum chamber components, the concept of a the *"loss factor"* was introduced by the definition

$$k_{\parallel} = -\frac{U}{q^2}. \tag{2.7}$$

Here U is the energy lost by the bunch and q its charge. If the longitudinal wake potential is given, the longitudinal loss factor can be obtained directly by integrating the product of the wake potential $W_{\parallel}(s)$ and the line density $\lambda(s)$ of the charge distribution

$$k_{\parallel} = \int W_{\parallel}(s)\lambda(s)ds. \tag{2.8}$$

It is measure for the longitudinal energy loss of the charge distribution during the passage through a structure.

The concept of a loss factor has been generalised to include the change of energy loss with transverse displacement of the bunch. The *transverse loss* or *kick factor* is defined by

$$k_{\perp} = \int W_{\perp}(s)\lambda(s)ds. \tag{2.9}$$

In the following chapters we will often refer to the transverse energy loss of an offset bunch somewhat losely as transverse loss. The difference is that those values are not normalised w.r.t. the offset of the beam.

2.1.3 Numerical calculation of wake potentials

The methods to calculate wake fields analytically are limited to a few simplified structures. To obtain the wake potentials induced in real accelerator structures one has to use numerical methods. There are numerous computer programs which incorporate these methods. Depending on the geometry of the structure one has to use 2-D or 3-D programs. An overview over these programs can be found in the book *Impedances and Wakes* [KZ97], §11A) and the compendium about computer programs in accelerator physics by the Los Alamos Accelerator Code Group [Gro90]. Two basic methods exist to solve the Maxwell equations numerically. The first one is called *Finite Difference*

(FD) Method or *Finite Integral Technique (FIT)*, the second one is the *Finite Element (FE) Method.* In both cases the physical problem is reduced to a set of linear equations which can be solved in an efficient way numerically. Nevertheless, the actual algorithms of the two methods are quite different. Since presently there are no *FE* programs available which allow to calculate transient time domain problems, i.e. excitation by a traversing charge distribution, all calculations for this thesis were done using programs based on the FD method.

Chapter 3

Decomposition of Wake Potentials

3.1 General principle

The calculation of wake potentials of short bunches in large 3-dimensional structures requires very large computer memories and CPU times and often even exceeds the available computer resources. A sufficiently accurate description of such 3-D structures leads typically to several million mesh cells. The size of the mesh steps in the direction of particle propagation can not be chosen arbitrarily large, but is determined by the bunch length. To obtain accurate results, about 10 mesh cells per σ of the bunch are required. The calculation of bunch shapes with discontinuities in their derivatives, like triangles, requires even smaller mesh sizes in the longitudinal direction [Mei97]. Since the total number of mesh points is limited by the resources, the description of a structure in transverse direction suffers.

To overcome this limitation, a method was developed which permits to calculate the wake potential of a short bunch from the wake potential of a longer one. The *Expansion Method for Calculating Wake Potentials* as described in [WZ89] uses a Hermite polynomial expansion which leads to good results for the calculation of wake potentials for longer bunches, but cannot be used to calculate those of shorter bunches. Another possibility would be to work in frequency domain and to calculate the wake potential of the longer bunch up to a quite long distance behind the bunch to obtain an accurate Fourier transform, divide by by the Fourier transform of the bunch and transform back into the time domain to obtain the wake function. This method requires also large computer resources, and is of limited accuracy. On the other hand the

decomposition method does not require a long wake potential which saves a lot of computing time and, with some restrictions, can be used to get an estimate of the wake potential of shorter bunches from those of longer bunches. The frequencies which are excited by a bunch are inversely proportional to its length. Figure 3.1 shows the frequency spectra of a Gaussian bunch with $\sigma = 5$ mm and triangular bunches with 10 and 20 ps half-width. The triangular bunches have somewhat higher frequency content and additional maxima at higher frequencies. Since a shorter bunch excites those higher frequencies, the decomposed wake potential calculated from a longer bunch can not contain this high frequency information.

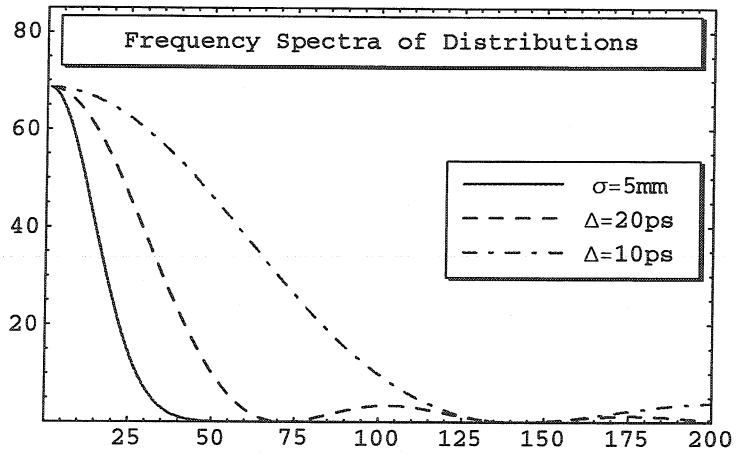

Figure 3.1: Frequency spectra of a Gaussian bunch with $\sigma = 5$ mm and Triangles with 10 and 20 ps half-width.

Nevertheless, this method is very useful when this high frequency information is not required, e.g. for the decomposition of longer bunches. Furthermore it is necessary if the minimum bunch length directly calculable is not sufficiently small. For the axially non-symmetric structures which will be studied in the following chapter, i.e. the shielded bellows and the separators in LEP, this minimum bunch length is presently 5 mm, using a longitudinal mesh step size of 0.5 mm. This limit was determined by the available computer resources of $\approx$ 500 MByte memory. In the multi-particle simulation program *TRISIM3D*, the triangular basis functions used to describe arbitrary bunch configurations are typically 10 ps and 20 ps long, which would require even smaller longitudinal meshes than 0.5 mm to obtain numerically accurate results. However, since these basis functions are used to reconstruct longer bunches in the range of 10 mm and above, the missing high frequency information is not very important.

3.2 Decomposition and Reconstruction

An arbitrary charge distribution can be well approximated by a superposition of a sufficiently large number of linear (i.e. triangular) basis functions as shown in Figure 3.2,

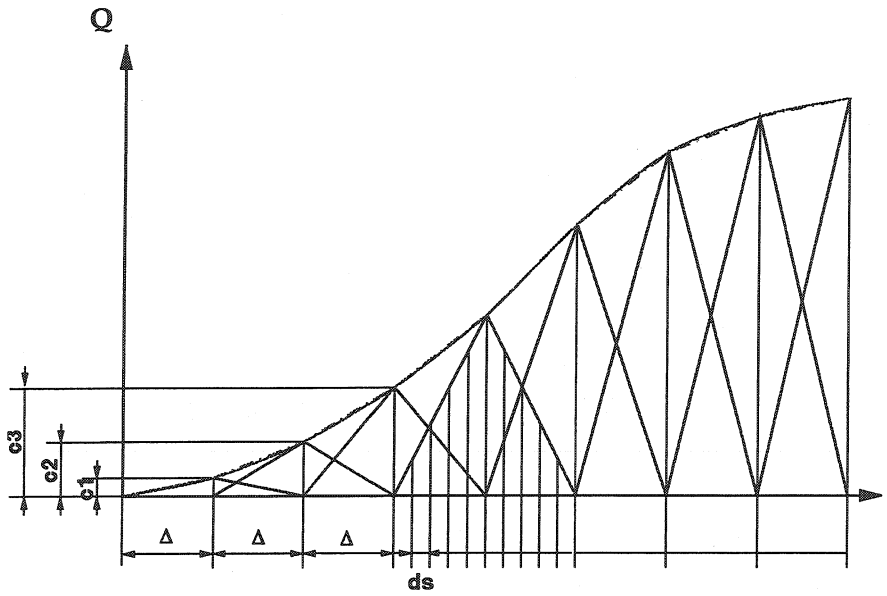

Figure 3.2: Linear expansion of a charge distribution using triangular shaped basis functions.

where Δ is the half-width of the triangles, ds the longitudinal mesh step, and c_1, c_2, c_3, ... c_n are the expansion coefficients of the linear expansion of the charge distribution. Given the total length l_c of the charge distribution, one needs

$$\hat{n} = \frac{l_c}{\Delta} + 1 \tag{3.1}$$

triangular basis functions to describe the distribution. Due to the linearity of Maxwell's equations, also the wake potential w_n^g of a Gaussian bunch can be expressed as a superposition of the wake potentials w_n^Δ of those triangular basis functions with the same expansion coefficients. The index n in the following equations refers to the n-th point of the wake potential, i.e. $w_n^g = w^g((n-1)ds)$.

$$
\begin{aligned}
w_1^g &= c_1 w_1^\Delta \\
w_2^g &= c_1 w_2^\Delta \\
&\vdots = \vdots \\
w_{k-1}^g &= c_1 w_{k-1}^\Delta \\
w_k^g &= c_1 w_k^\Delta + c_2 w_1^\Delta \\
w_{k+1}^g &= c_1 w_{k+1}^\Delta + c_2 w_2^\Delta \\
&\vdots = \vdots \\
w_{\hat{n}\cdot k}^g &= c_1 w_{\hat{n}\cdot k}^\Delta + c_2 w_{(\hat{n}-1)k}^\Delta + \cdots + c_{\hat{n}} w_k^\Delta
\end{aligned}
\tag{3.2}
$$

where the following symbols have been used:

k	... number of wake potential points in a half-width of the triangular basis function (Δ),
$\hat{n}$	... number of triangles used to represent the Gaussian charge distribution,
$c_1 \ldots c_{\hat{n}}$	... expansion coefficients of the linear expansion of the Gaussian charge distribution.

Carrying on this thread, the wake potential of a Gaussian bunch obtained with a mesh program can be seen as superposition of wake potentials of triangular charge distributions with a half-width equal to the mesh size in the longitudinal direction. The charge distribution taken into account for wake field calculations usually extends over a range of $\pm 5\,\sigma$ where about 10 mesh points per σ is a good value to obtain numerically accurate results. Therefore the wake potential of the Gaussian charge distribution can be seen as consisting of the contributions of 100 mesh-step-sized triangles (Fig. 3.3).

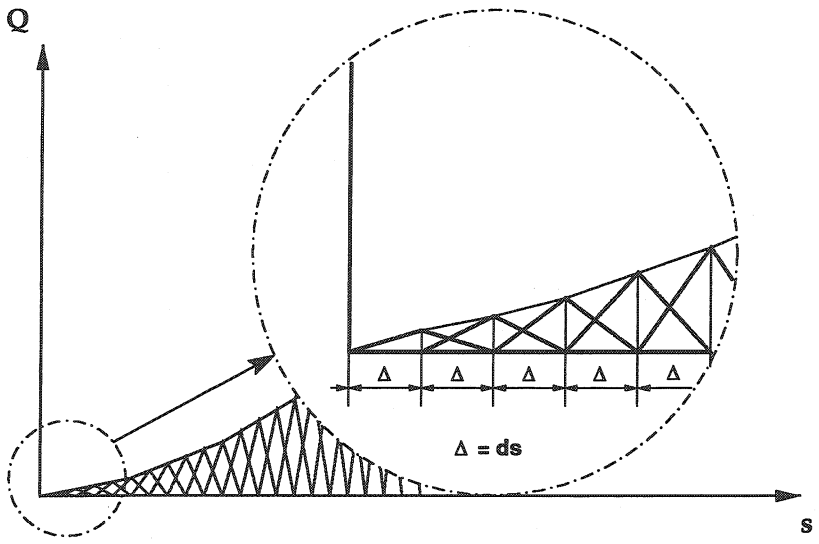

Figure 3.3: Linear expansion of a charge distribution using mesh-step sized triangular basis functions

The equations (3.2) can then be written as ($k = 1$, $c_k = 0$ for $k > \hat{n}$, $n_p \ldots$ number of wake potential points)

$$
\begin{array}{lllllllll}
w_1^g & = c_1 w_1^\Delta & & & & & & & \\
w_2^g & = c_1 w_2^\Delta & + c_2 w_1^\Delta & & & & & & \\
w_3^g & = c_1 w_3^\Delta & + c_2 w_2^\Delta & + c_3 w_1^\Delta & & & & & \\
\vdots & = & \vdots & & & \ddots & & & \\
w_{\hat{n}-1}^g & = c_1 w_{\hat{n}-1}^\Delta & + c_2 w_{\hat{n}-2}^\Delta & + \cdots + & c_{\hat{n}-1} w_1^\Delta & & & & \\
w_{\hat{n}}^g & = c_1 w_{\hat{n}}^\Delta & + c_2 w_{\hat{n}-1}^\Delta & + \cdots + & c_{\hat{n}-1} w_2^\Delta & + & c_{\hat{n}} w_1^\Delta & & \\
w_{\hat{n}+1}^g & = c_1 w_{\hat{n}+1}^\Delta & + c_2 w_{\hat{n}}^\Delta & + \cdots + & c_{\hat{n}-1} w_3^\Delta & + & c_{\hat{n}} w_2^\Delta & & \\
w_{\hat{n}+2}^g & = c_1 w_{\hat{n}+2}^\Delta & + c_2 w_{\hat{n}+1}^\Delta & + \cdots + & c_{\hat{n}-1} w_4^\Delta & + & c_{\hat{n}} w_3^\Delta & & \\
\vdots & = & \vdots & & & & & & \\
w_{n_p}^g & = c_1 w_{n_p}^\Delta & + c_2 w_{n_p-1}^\Delta & + \cdots + & c_{\hat{n}-1} w_{n_p-\hat{n}+1}^\Delta & + & c_{\hat{n}} w_{n_p-\hat{n}}^\Delta & &
\end{array}
\tag{3.3}
$$

Sorting by increasing index n of the w_n^Δ leads readily to

$$
\begin{array}{rcl}
w_1^g & = & c_1 w_1^\Delta \\
w_2^g & = & c_2 w_1^\Delta + c_1 w_2^\Delta \\
w_3^g & = & c_3 w_1^\Delta + c_2 w_2^\Delta + c_1 w_3^\Delta \\
\vdots & = & \vdots \qquad\qquad\qquad\qquad \ddots \\
w_{\hat{n}-1}^g & = & c_{\hat{n}-1} w_1^\Delta + c_{\hat{n}-2} w_2^\Delta + c_{\hat{n}-3} w_3^\Delta + \cdots + c_1 w_{\hat{n}-1}^\Delta \\
w_{\hat{n}}^g & = & c_{\hat{n}} w_1^\Delta + c_{\hat{n}-1} w_2^\Delta + c_{\hat{n}-2} w_3^\Delta + \cdots + c_2 w_{\hat{n}-1}^\Delta + c_1 w_{\hat{n}}^\Delta \\
w_{\hat{n}+1}^g & = & c_{\hat{n}} w_2^\Delta + c_{\hat{n}-1} w_3^\Delta + \cdots + c_3 w_{\hat{n}-2}^\Delta + c_2 w_{\hat{n}-1}^\Delta + c_1 w_{\hat{n}}^\Delta \\
\vdots & = & \vdots
\end{array}
\tag{3.4}
$$

which is a linear system of n_p equations, where n_p is the number of wake potential points. Defining the vectors

$$
\mathbf{w^g} = \left(w_1^g, w_2^g, \cdots, w_{n_p}^g\right), \qquad \mathbf{w}^\Delta = \left(w_1^\Delta, w_2^\Delta, \cdots, w_{n_p}^\Delta\right), \tag{3.5}
$$

where $\mathbf{w^g}$ is the wake potential of the Gaussian charge distribution and $\mathbf{w}^\Delta$ is the one of the triangular basis function, on can write the equations (3.4) in matrix form as

$$
\mathbf{w^g} = \mathbf{C} \cdot \mathbf{w}^\Delta \tag{3.6}
$$

where the following matrix of coefficients $\mathbf{C}$ has been introduced:

$$
\mathbf{C} = \begin{pmatrix}
c_1 & 0 & 0 & \cdots & 0 & 0 & 0 & 0 & \cdots \\
c_2 & c_1 & 0 & \cdots & 0 & 0 & 0 & 0 & \cdots \\
c_3 & c_2 & c_1 & \cdots & 0 & 0 & 0 & 0 & \cdots \\
\vdots & \vdots & \vdots & \ddots & 0 & 0 & 0 & 0 & \cdots \\
c_{\hat{n}} & c_{\hat{n}-1} & c_{\hat{n}-2} & \cdots & c_1 & 0 & 0 & 0 & \cdots \\
0 & c_{\hat{n}} & c_{\hat{n}-1} & c_{\hat{n}-2} & \cdots & c_1 & 0 & 0 & \cdots \\
0 & 0 & c_{\hat{n}} & c_{\hat{n}-1} & c_{\hat{n}-2} & \cdots & c_1 & 0 & \cdots \\
0 & 0 & 0 & c_{\hat{n}} & c_{\hat{n}-1} & c_{\hat{n}-2} & \cdots & c_1 & \cdots \\
\vdots & \vdots & \vdots & \vdots & \vdots & \vdots & \vdots & \vdots & \ddots
\end{pmatrix}
\tag{3.7}
$$

The wake-potential of this mesh-sized triangular interpolating function is then obviously given by

$$\mathbf{w}^{\Delta} = \mathbf{C}^{-1} \cdot \mathbf{w}^{g}. \tag{3.8}$$

To calculate the wake potential of a second charge distribution one simply has to multiply the wake potential of the mesh-sized triangle with the matrix $\mathbf{D}$ of the expansion coefficients of the new distribution

$$\mathbf{w}^{g} = \mathbf{D} \cdot \mathbf{w}^{\Delta}. \tag{3.9}$$

The calculation of $\mathbf{C}^{-1}$ (the inverse of $\mathbf{C}$) might lead in practice to numerical problems, due to the factor $c_1^{-n_p}$ in the calculation of the inverse Matrix. Therefore a recursive formula following directly from Eqn. (3.4) is better suited for application of the decomposition method.

$$\tilde{w}_n^{\Delta} = \frac{1}{c_1}\left(w_n^g - \sum_{k=2}^{n} c_k\, \tilde{w}_{n-k+1}^{\Delta}\right) \tag{3.10}$$

In fact this form is much better suited for implementation in a program. Nevertheless there are still some numerical constraints which one has to take into account.

3.3 Numerical considerations

To optimise the calculation of the inverse of the matrix **C** one can take advantage of the properties of **C**. The coefficients c_n of the matrix **C** are defined by the magnitude of the Gaussian distribution at the positions of the mesh lines,

$$c_n = \frac{1}{\sqrt{2\pi}\sigma} e^{-\frac{((n-1)\,dz - i_\sigma\,\sigma)^2}{2\sigma^2}}, \tag{3.11}$$

where dz is the mesh-size in longitudinal direction and i_σ is half the length of the distribution in units of σ. These coefficients extend over several orders of magnitude. The ratio of maximum to minimum coefficient is given by the relation

$$\frac{c_{max}}{c_1} = e^{\frac{i_\sigma^2}{2}}, \tag{3.12}$$

and depends only on the value of i_σ. The matrix **C** for a Gaussian bunch ($\sigma = 5$ mm) is shown in Figure 3.4, where the hatching indicates regions outside the $\pm$ 5 σ range of the charge distribution, where the coefficients c_n are zero by definition.

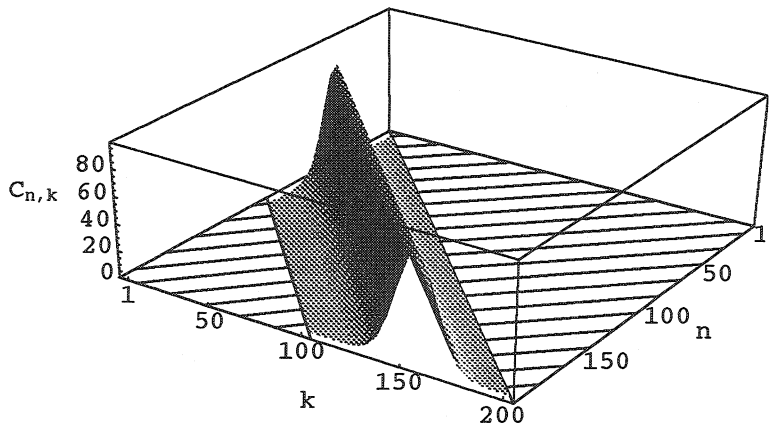

Figure 3.4: Matrix of coefficients **C** for a $\sigma = 5\,mm$ Gaussian bunch and a longitudinal mesh step size of $ds = 0.5$ mm.

The inverse matrix of this triangular matrix is again a triangular matrix and the components $\tilde{c}_n$ of this matrix can be calculated using the recursive relation

$$\tilde{c}_1 = \frac{1}{c_1}; \qquad \tilde{c}_n = -\frac{1}{c_1}\sum_{k=1}^{n-1}(\tilde{c}_k \cdot c_{n-k+1}) \quad \text{for} \quad n \geq 2. \tag{3.13}$$

The order of the coefficients of the matrix $\mathbf{C^{-1}}$ is the same as for $\mathbf{C}$. Their absolute values for a Gaussian bunch with $\sigma = 5$ mm are shown in Figure 3.5. The vertical scale of this plot is pseudo-logarithmic, i.e. the logarithm of the absolute values are multiplied by the sign of the original value.

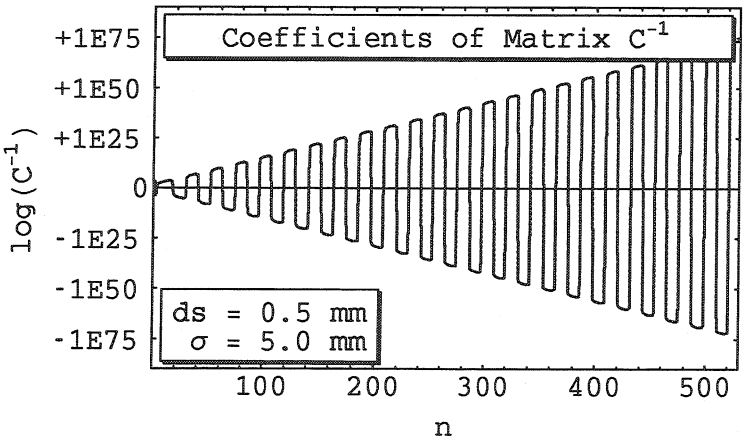

Figure 3.5: Logarithmic plot of the coefficients of the inverse matrix $\mathbf{C^{-1}}$ for a Gaussian bunch ($\sigma = 5$ mm).

The values of the coefficients $\tilde{c}_n$ extend over many orders of magnitude and show a strong exponential growth with the index n. This growth leads to numerical problems when the inverted matrix is used to calculated the wake potential of the short triangle. In order to avoid errors due to differences of very large numbers one has to know the original wake potential with a very high numerical precision in the order of hundred digits, which is nowadays practically not possible to obtain.

One way to circumvent this difficulty is to suppress the first part of the wake potential. This corresponds also to a suppression of the first part of the charge distribution, where the density is very low anyhow. The index of the first point of the distribution taken into account will be refered to as *start-index* n_0 of the decomposition. A shift of the start-index to values $n_0 > 1$ reduces the ratio c_{max}/c_1 of the matrix coefficients and the exponential growth of the

coefficients of the inverse matrix $\mathbf{C^{-1}}$ becomes smaller. Figure 3.6 shows the maxima of the absolute values of the coefficients $\tilde{c}_n$ for different values of the start-index n_0. For a $\sigma = 5$ mm Gaussian bunch and a longitudinal mesh step size of $ds = 0.5$ mm, the variation is smallest for values of n_0 between 30 and 35. The impact of the reduction of the length of the charge distribution is that the first n_0 points of the wake potential are ignored. This leads to a few percent loss of accuracy as will be shown for the examples in the next section.

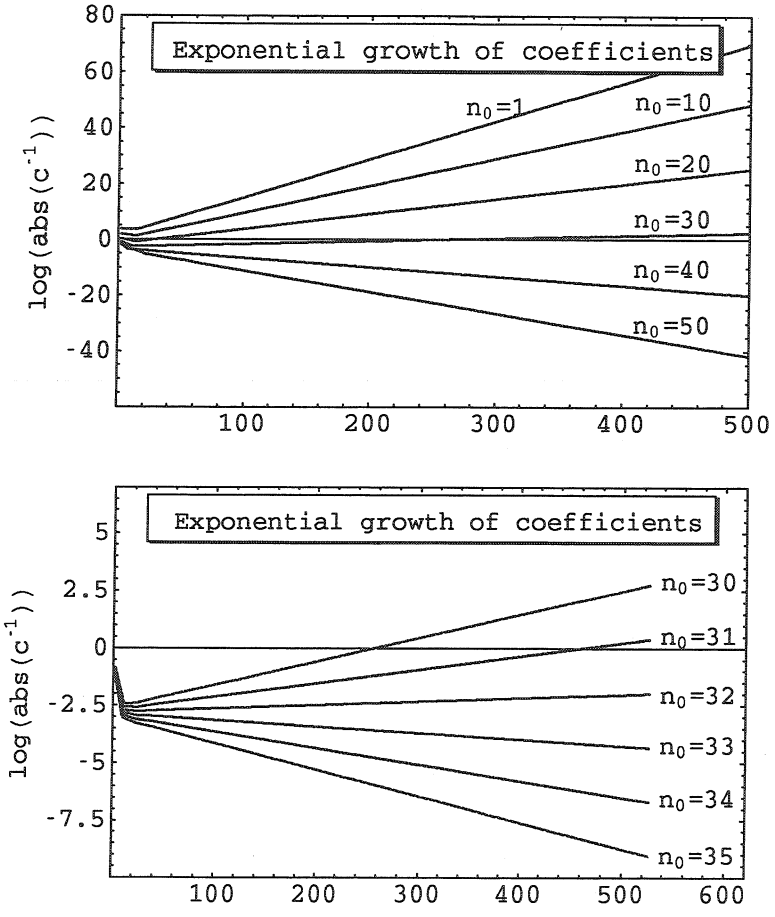

Figure 3.6: Logarithmic growth of the coefficients of the matrix $\mathbf{C^{-1}}$ for a Gaussian bunch ($\sigma = 5$ mm) as function of the start-index n_0.

3.4 Applications of the Decomposition Method

3.4.1 Example Pillbox Cavity

The decomposition of wake potentials will be tested first on a simple circular cylindrical "pillbox" cavity. This geometry was chosen to allow a fast calculation of the wake potentials for various bunch lengths. The geometry of this test-structure is shown in Figure 3.7.

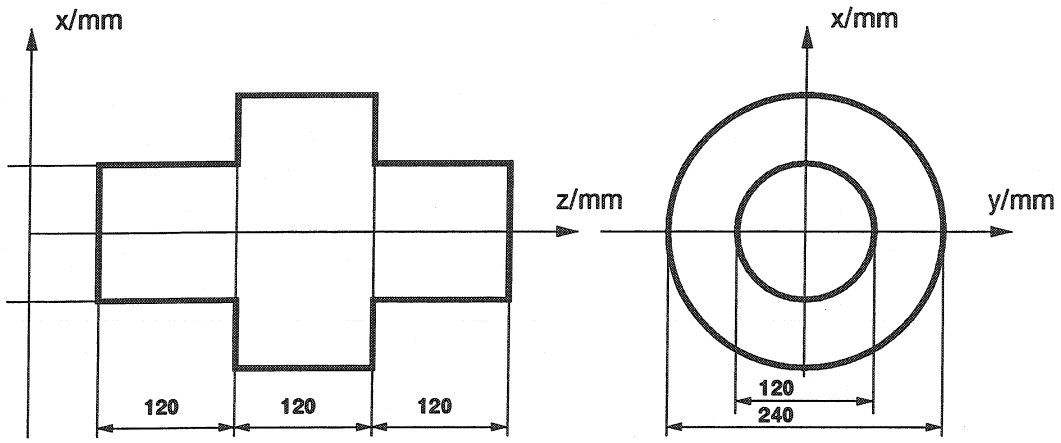

Figure 3.7: Geometry of the "pillbox" cavity with side tubes.

The impedance of this structure does not contain strong high frequency components and is therefore well suited for a first test of the decomposition method. The wake potentials for Gaussian bunches of various lengths (σ = 40, 20, 10, 5 mm) and for triangular bunches with 10 and 20 ps half-width were calculated using *ABCI*[Chi94]. As a measure of the accuracy of the decomposition and reconstruction the following 3 quantities are used:

- Relative error of loss-factor

$$\Delta k = \frac{k_{g,0} - k_{g,r}}{k_{g,0}} \tag{3.14}$$

- Relative maximum local error

$$\Delta w^{mlr} = \frac{\max(\mathbf{w}^{g,0}(s) - \mathbf{w}^{g,r}(s))}{\max(\mathbf{w}^{g,0}(s))} \tag{3.15}$$

- Relative integrated error

$$\Delta w^{int} = \frac{\int |\mathbf{w}^{\mathbf{g},\mathbf{0}}(s) - \mathbf{w}^{\mathbf{g},\mathbf{r}}(s)|\, ds}{\int |\mathbf{w}^{\mathbf{g},\mathbf{0}}(s)|\, ds} \tag{3.16}$$

The *relative error of the loss-factor* is the difference between the loss-factors calculated from the reconstructed and directly calculated wake potential, normalised by the value of the latter. This error is a measure for the precision of the short range wake potential, while the following two errors weight the hole calculation range. The *relative maximum local error* is defined as the maximum difference of the two wake potentials normalised by maximum value of the directly calculated one. The *relative integrated error* refers to the area between the two wakes wrt. the integral of the absolute value of the directly calculated wake.

The wake potential for the mesh-sized ($dz = 0.5$ mm) triangular distribution[1] calculated from the wake potential of a $\sigma = 5$ mm Gaussian bunch is shown in Figure 3.8 for $n_0 = 1$. The exponential growth of the coefficients of the inverse matrix $\mathbf{C^{-1}}$, mentioned in the previous section, induces the exponential growth of the basis wake, which can be seen clearly.

If one chooses the numerical precision high enough, e.g. about 100 digits for 600 wake potential points, the error of the reconstruction of the original wake potential remains insignificant, i.e. well below the accuracy of the original wake potential (Fig. 3.9).

On the contrary, the reconstruction even of longer charge distributions fails completely for $n_0 = 1$ (Fig. 3.10). This can be understood by taking into account the exponential growth of the elements of the inverted matrix (see previous section). Due to this growth the first points of the original wake potential are weighted the stronger the longer the reconstructed wake potential gets.

A shift of the starting point n_0 of the decomposition reduces the exponential growth of the basis-wake of the mesh-step-sized basis-function and therefore also the reconstruction of wakes for longer bunch lengths converges. The errors of the reconstruction - defined in Eqns. (3.14)-(3.16) - are shown in Figure 3.11

[1] The wake potentials of these mesh-sized triangles will be refered to as *basis-wake* of the decomposition and the symbol $\mathbf{w}^{\mathbf{B},\mathbf{bl}}_{\mathbf{n_0}}$ will be used (n_0 refers to the start-index and *bl* to the bunch length from which the basis-wake was derived, e.g. g5 ... Gaussian bunch with $\sigma = 5$ mm).

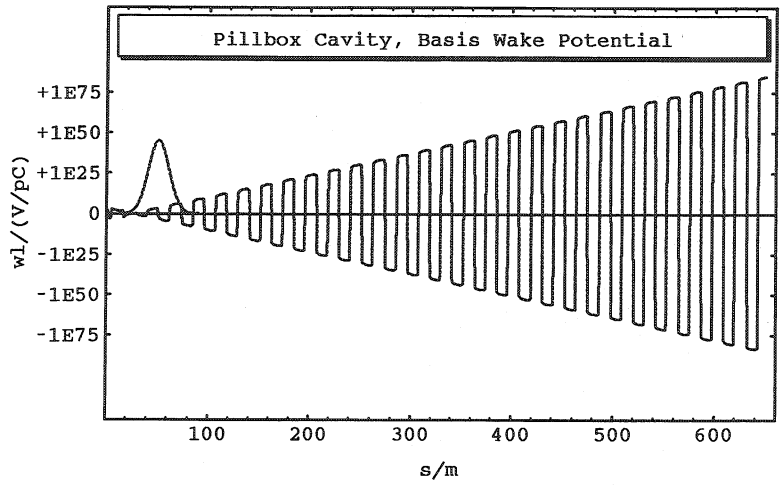

Figure 3.8: Basis-wake Wake potential of 0.5 mm mesh-sized triangular distribution calculated from the wake potential of a 5 mm Gaussian bunch.

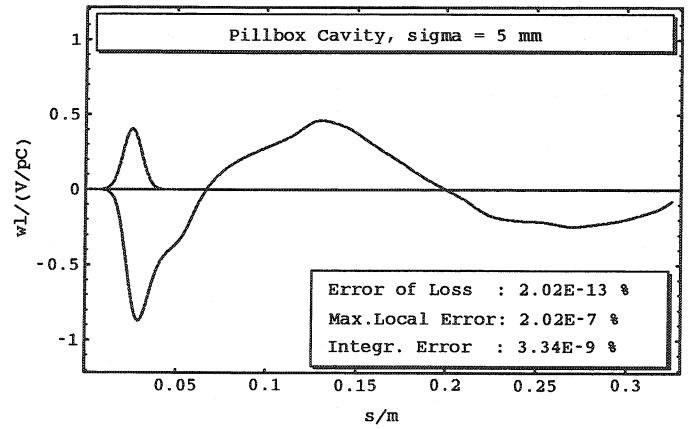

Figure 3.9: Accuracy of reconstruction (numerical precision = 200, $n_0 = 1$).

for a Gaussian bunch ($\sigma = 5$ mm) as function of the start-index n_0, i.e the first wake potential point taken into account.

The minima of the maximum local and the integrated errors occur, as can be expected from the numerical considerations, between $n_0 \approx 30 - 35$ while the error of the loss-factor has its minimum already at $n_0 \approx 20$. The same dependence of the errors on the start-index can be found for other bunch lengths. The reason for the different minima of the errors is the loss of information

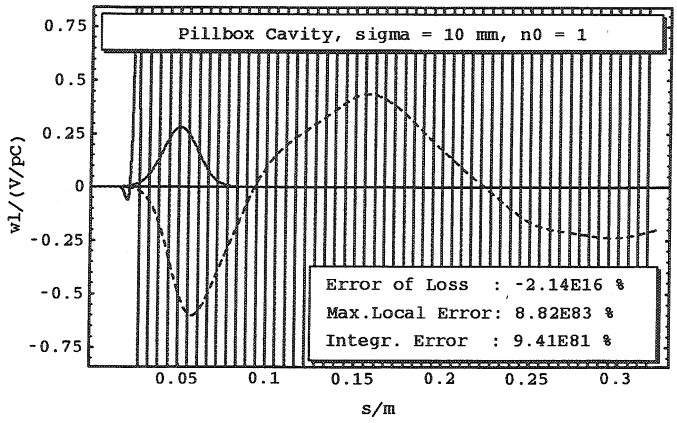

Figure 3.10: Wake potential of a 10 mm Gaussian bunch reconstructed from $\mathbf{w_1^{B,g5}}$ i.e. derived from a $\sigma = 5\,\mathrm{mm}$ Gaussian bunch for $n_0 = 1$.

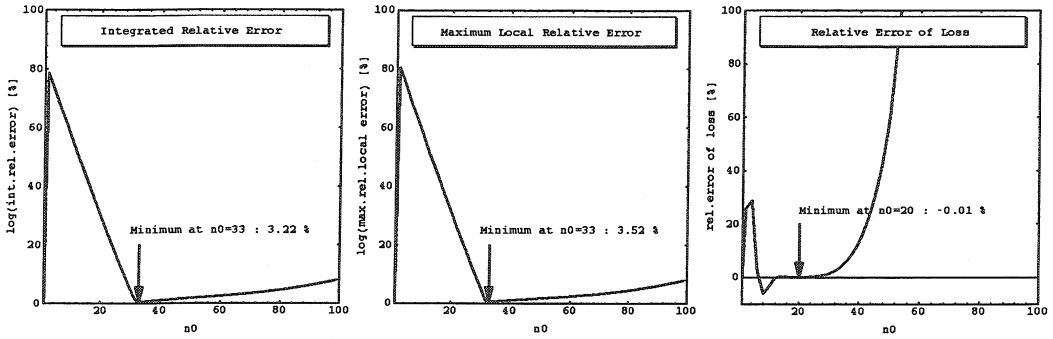

Figure 3.11: Errors of the wake potential of a Gaussian bunch ($\sigma = 5$ mm) (reconstructed from basis-wake $\mathbf{w_{n_0}^{B,g5}}$ derived from the same Gaussian bunch) as function of the start-index n_0.

due to the shift of the start-index.[2] For wake potentials which contain not too high frequency components the error of the loss-factor for start-indices n_0 around $30 - 35$ is still sufficiently low. The reconstructed wake potentials and their errors for various bunch lengths, calculated from the basis wake $\mathbf{w_{35}^{B,g5}}$ are shown in Figure 3.12. The accuracy of the reconstructed wake potentials of the Gaussian bunches is within a few per-cent. Also the accuracy of the wake potential of the 20 ps triangle is still acceptable, while the one of the 10 ps triangle has already errors well above 10%.

[2]One can improve the accuracy of the decomposition by linear combination of basis-wakes derived for different start-index n_0. This will be applied in the next example (§3.4.2: example shielded bellows.)

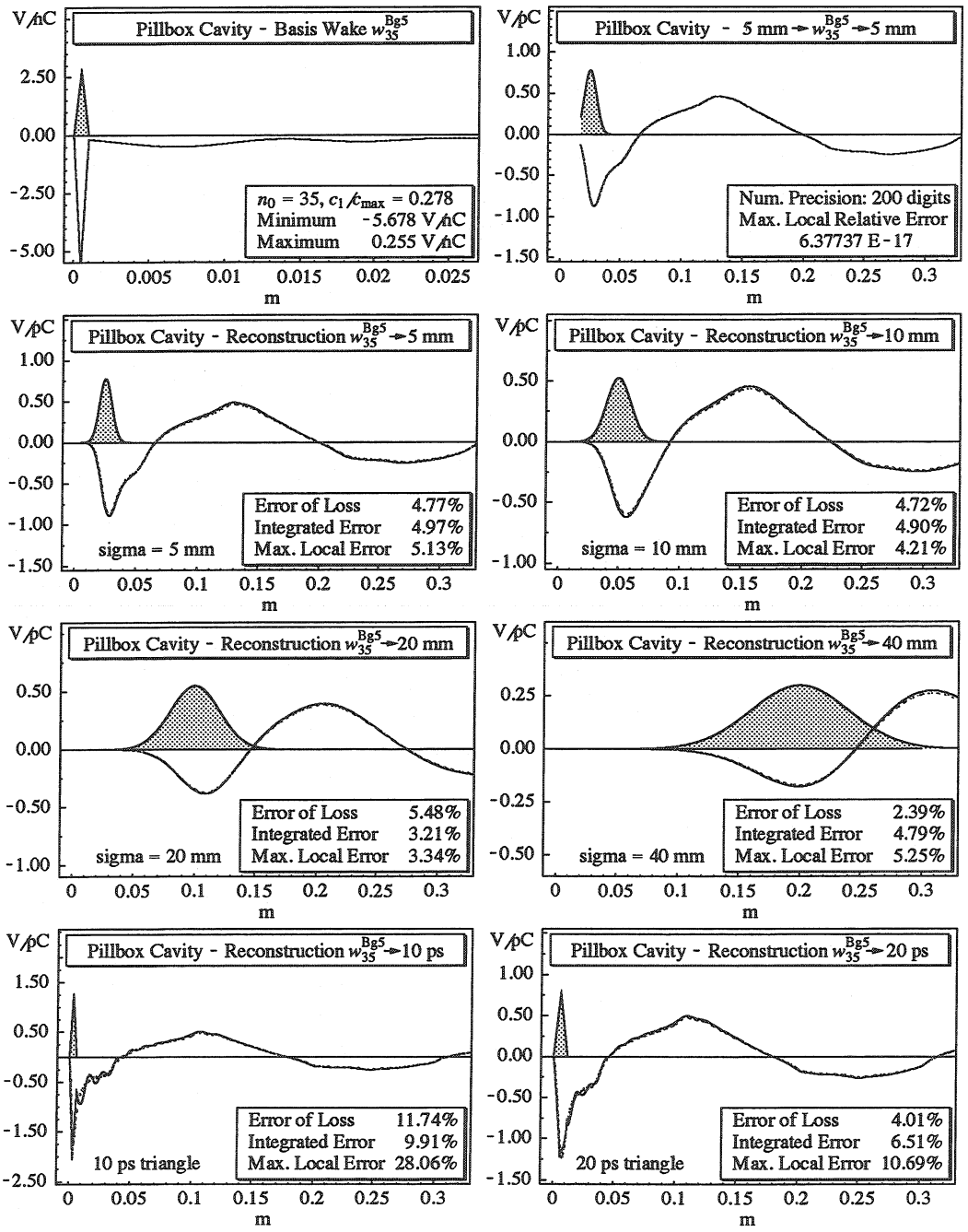

Figure 3.12: Wake potentials of Gaussian bunches ($\sigma = 5, 10, 20, 40$ mm) resp. triangular bunches (10, 20 ps) reconstructed from the basis wake $\mathbf{w_{35}^{B,g5}}$ (—) compared with directly computed wakes (- - -).

3.4.2 Example Shielded Bellows

As a next application example of the *decomposition method* an elliptic model of the LEP shielded bellows will be used. The details of the geometric properties of this structure are described in section 4.4.2. To test the accuracy of the decomposition the directly computed wakes of Gaussian bunches ($\sigma = 5, 10$ mm) will be used. Both wake potentials and the loss factors are shown in Figure 3.13. The basis-wake will be derived from the 5 mm Gaussian bunch.

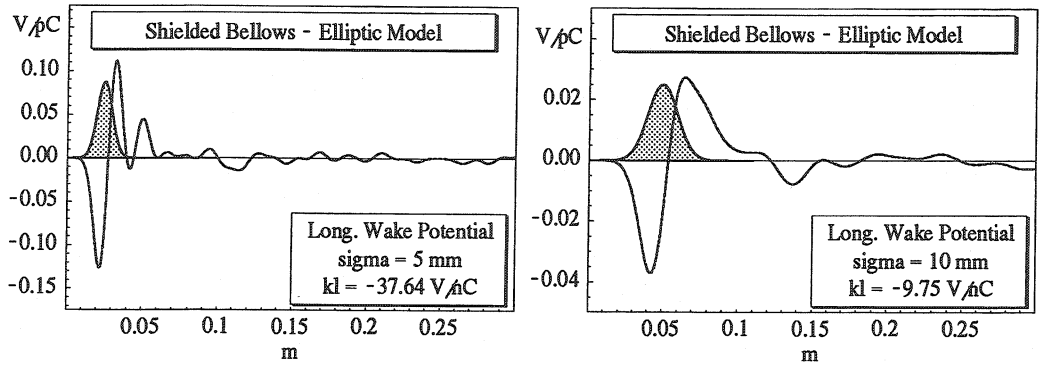

Figure 3.13: Longitudinal wake potentials of Gaussian bunches.

The reconstruction of wake potentials from the basis-wake for varying initial shift n_0 results in a large difference between the minima of the errors of the loss factors and the maximum local resp. the integrated errors (Fig. 3.14).

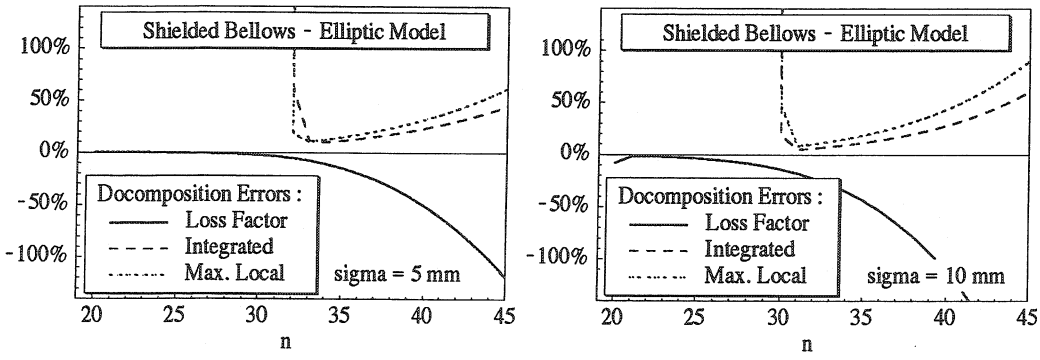

Figure 3.14: Errors of the wake potentials of Gaussian bunches ($\sigma = 5, 10$ mm) as function of the start-index n_0 reconstructed from the basis-wake $\mathbf{w}_{\mathbf{n_0}}^{\mathbf{B,g5}}$.

As for the pillbox cavity, the minima for the errors of the loss factors occur

for lower values of n_0 than the minima of the integrated and maximum local errors. The information lost due to the shift of n_0 causes this difference in the positions of the minima. While for the pillbox cavity the errors of the loss factors remained still quite low when exceeding the optimum value of n_0, these errors become now quite big for the bellows. As can be easily seen, there is no satisfying compromise concerning all errors by simply varying the starting point n_0. Either the error of the loss factor or the integrated error and the maximum local error become too big (Fig. 3.15). Furthermore, the individual optimum values are different for different bunch lengths, which makes the obtained basis-wakes not very applicable for the reconstruction of arbitrary distributions. One would have to recalculate the basis-wake every time with n_0 adjusted to the actual bunch length.

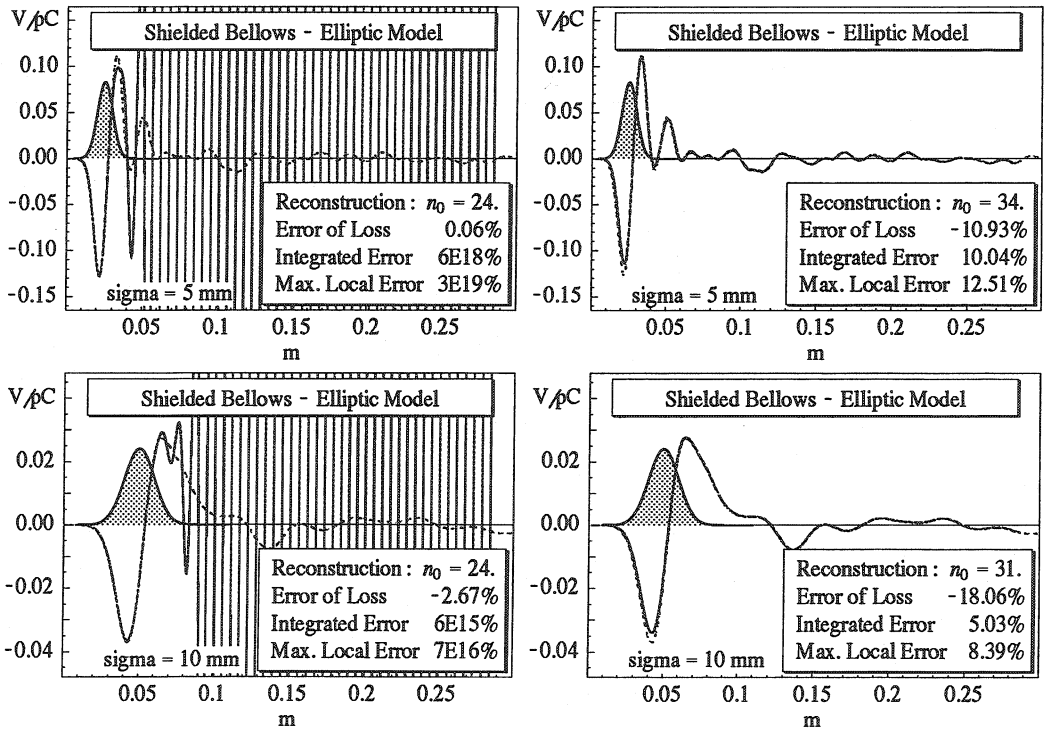

Figure 3.15: Reconstructed wake potentials for the start-index n_0 optimised with respect to the different errors (left side: minimum error of loss factor, right side minimum error for long range wake potential).

The early part of the wake potentials can be better described using basis-wakes with lower n_0 while the long range parts of those wakes demand a somewhat higher n_0. This general behaviour makes it self-evident to try to combine

different basis-wakes (obtained for different start-index n_0) in a proper way. Linear and higher order combinations of various basis-wakes were studied. The results obtained with linear combination of basis-wakes were found to give the best results. Using the following linear combination function f_c

$$\begin{aligned} f_c(n, n_{comb}) &= \frac{n-1}{n_{comb}} \quad \text{for} \quad n \leq n_{comb} \\ f_c(n, n_{comb}) &= 1 \quad \text{for} \quad n > n_{comb} \end{aligned} \tag{3.17}$$

two basis-wakes, $\mathbf{w}^{\mathbf{B,bl}}_{\mathbf{n_1}}$ and $\mathbf{w}^{\mathbf{B,bl}}_{\mathbf{n_1}}$, are combined as follows

$$\mathbf{w}^{\mathbf{B,bl}}_{\mathbf{comb}}(n) = (1 - f_c(n, n_{comb}))\, \mathbf{w}^{\mathbf{B,bl}}_{\mathbf{n_1}}(n) + f_c(n, n_{comb}) \mathbf{w}^{\mathbf{B,bl}}_{\mathbf{n_2}}(n), \tag{3.18}$$

up to the combination length n_{comb}, i.e. the linear combination starts at the first point, where the basis-wake obtained for the lower values of n_0 has full strength and ends at n_{comb} where only the basis-wake with higher n_0 contributes anymore. The dependence of the errors on this combination length n_{comb} can be seen in Figure 3.16.

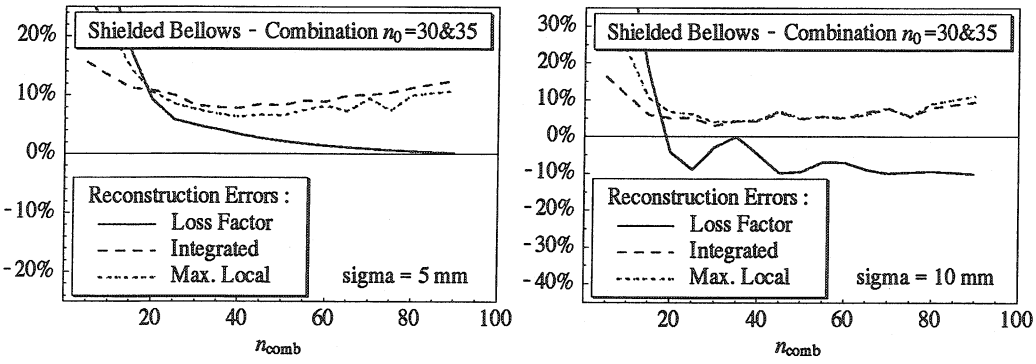

Figure 3.16: Errors of the reconstructed wake potentials of Gaussian bunches ($\sigma = 5, 10$ mm) as function of the length n_{comb} of the linear combination of the basis-wakes $\mathbf{w}^{\mathbf{B,g5}}_{\mathbf{30}}$ and $\mathbf{w}^{\mathbf{B,g5}}_{\mathbf{35}}$.

The integrated and the maximum local errors show a flat minimum for combination lengths around $n_{comb} = 30$ to 40. The errors of the loss-factors are also sufficiently low in this region. The resulting reconstructed wake potentials for three bunch lengths and the basis-wake used to obtain these potentials are shown in Figure 3.17. The basis-wake potential was derived by a linear combination of the basis-wakes for starting values $n_0 = 30$ and $n_0 = 35$ up to a distance of $n_{comb} = 36$ points from the beginning of the first basis-wake

potential. The values of the errors for all 3 bunch lengths remain sufficiently low. Since the combination of basis-wakes leads to a significant improvement, this method will be applied for all upcoming applications of the decomposition method, i.e. decomposition of 5 mm Gaussian bunches to derive the wake potentials of 10 and 20 ps triangles, which will be used in the simulation program TRISIM3D.

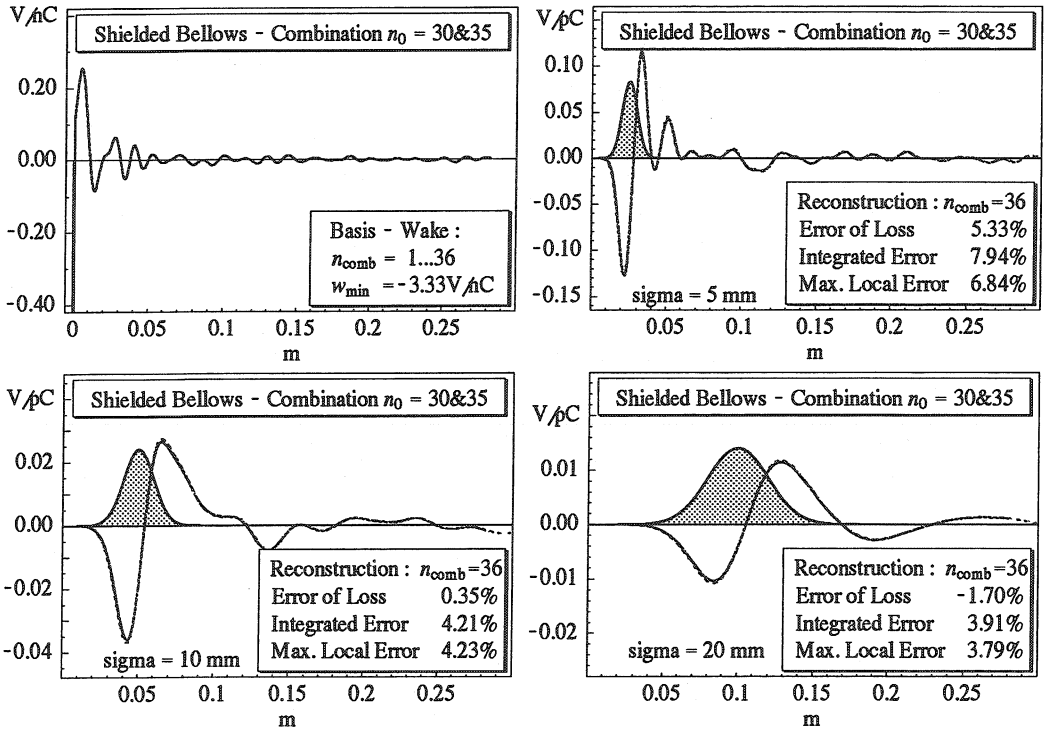

Figure 3.17: Combined basis-wake and reconstructed wake potentials of Gaussian bunches with $\sigma = 5, 10, 20$ mm (—) compared with directly computed wake potentials (- - -)

3.4.3 Example Pillbox Cavity (II)

The combination of basis-wakes was successfully introduced to minimise the otherwise large errors of the decomposition for the shielded bellows. Since the improvement was quite significant it will now be also applied to the pillbox cavity of §3.4.1. The combination basis-wake used for the pillbox cavity was derived using the same parameters as those used in the previous section i.e. a linear combination of $\mathbf{w}_{30}^{B,g5}$ and $\mathbf{w}_{35}^{B,g5}$ up to $n_{comb} = 36$. Comparison of the

resulting errors with those of the decomposition without combination of basis-wakes (Fig. 3.12) indicates a substantial improvement. The wake potentials of several Gaussian bunches (σ=5, 10, 20, 40 mm) and 10 resp. 20 ps triangles were reconstructed using this combination basis-wake potential (Fig. 3.18).

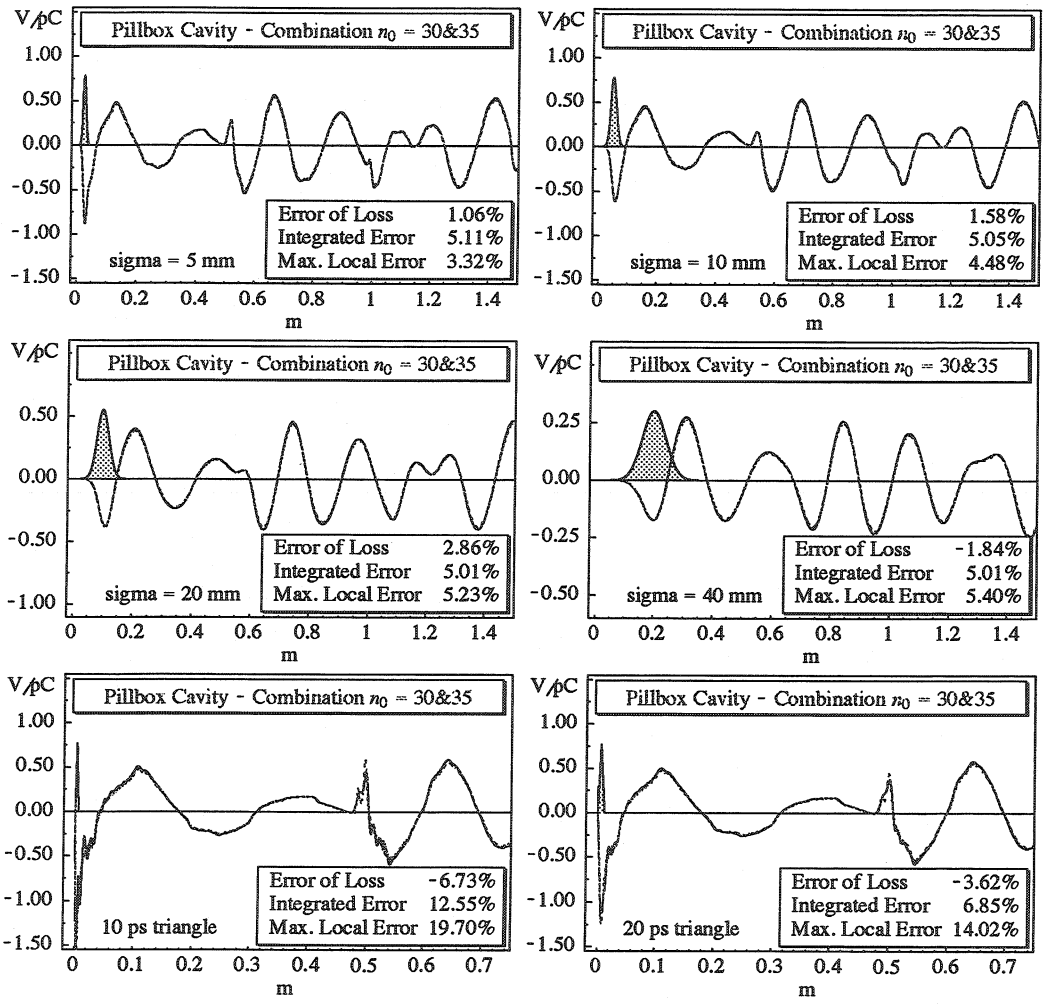

Figure 3.18: Pillbox Cavity - Wake potentials for Gaussian and triangular bunches derived from the combined basis-wake $\mathbf{w}^{\mathbf{B,g5}}_{\mathbf{30,35}}$(– – –) , compared with directly computed wakes (- - -).

At the same time, the short range as well as the long range precision are very good for all longer bunches. The maximum local and integrated errors are around 5% and the errors of the loss factors are smaller than 3%. For the shorter, triangular bunches the situation is not quite as good. For the 20 ps triangle the max. local error still exceeds 10% and the same error for

the 10 ps triangle reaches almost 20%. But these are peak values and the integrated errors for both triangles are already better and the errors of the loss factors have values below 7% resp. 4%, i.e. much better than before. Anyway, these wake potentials will be used in TRISIM3D to reconstruct bunch distributions having a typical length of 10 mm and longer. Since there is practically no loss of precision when expanding the actual distribution with triangular basis functions, the errors of the decomposition for the 10 mm and 20 mm Gaussian bunches are more relevant. To emphasise this statement the wake potentials of these two bunch lengths were reconstructed using the 10 resp. 20 ps triangular wakes which were derived from the combined basis-wake (Fig. 3.19). There is certainly no significant increase of the errors compared to the direct reconstruction of these wake potentials from the basis-wake.

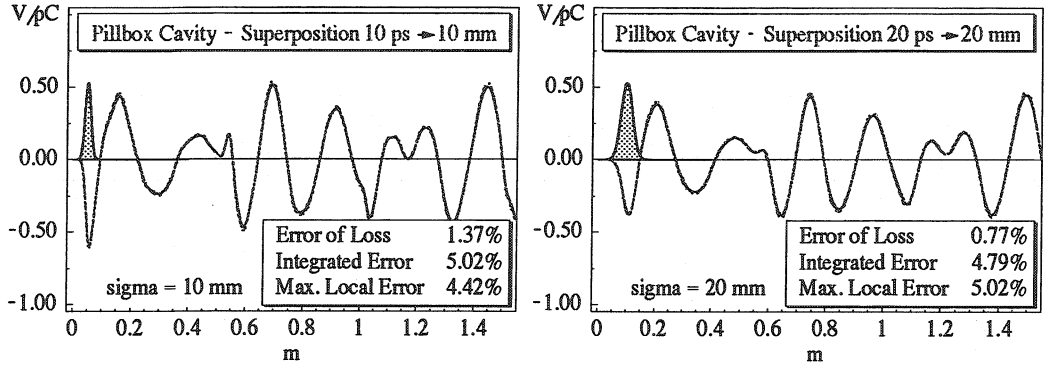

Figure 3.19: Wake potential of Gaussian bunches by superposition of triangular wake potentials resulting from decomposition, compared with directly computed wakes (- - -).

Chapter 4

Wake Potentials of 3-Dimensional Structures

4.1 Structures with Symmetry Planes

Most of the rotationally unsymmetric vacuum components used in accelerators have two, or at least one, symmetry planes. In the calculation of wake potentials this fact can be used to reduce the computational effort by limiting the calculation to only a part of the structure.

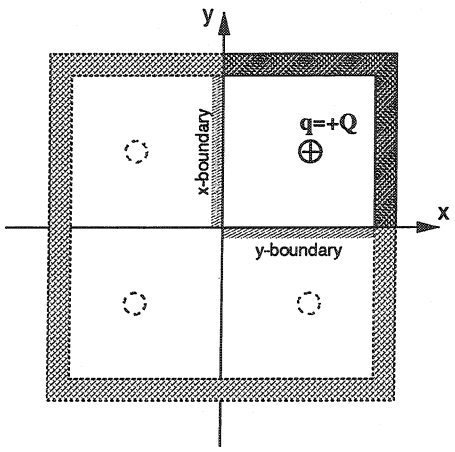

Figure 4.1: Image charges due to the transverse boundary conditions in a 3-dimensional structure with 2 symmetry planes.

When a structure has such symmetry planes only half or a quarter of it are needed for wake field calculations. The boundary conditions of the fractional

part need to be defined, and the resulting wake potentials must be combined properly.

When one uses only a quarter of a structure, there are naturally 4 possible arrangements of the electric resp. magnetic boundaries of the model. The image charges due to these boundary conditions, induced by a charge with non-zero horizontal and vertical offset are shown in Figure 4.2. These image charges also induce fields in the structure and have therefore to be taken into account.

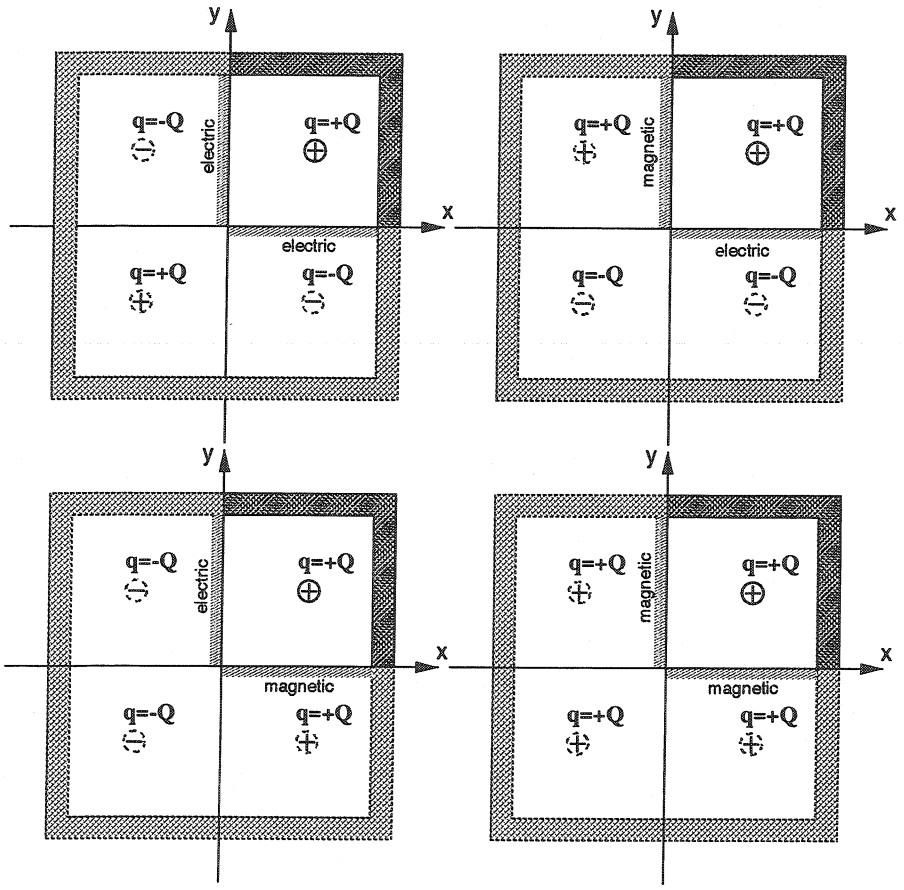

Figure 4.2: Image charges for the 4 combinations of electric and magnetic boundary conditions for a structure with 2 symmetry planes.

For the case of a non-zero beam-offset in both transverse directions this leads to the necessity of 4 independent calculations as shown in Figure 4.2. The results of the individual calculations can then be combined to get those for the full structure. If either the horizontal or the vertical beam offset is zero, only 2 calculations are needed, since the other boundary configurations yield no

contribution (Fig. 4.1). For an on-axis beam only the case with two magnetic boundaries has to be considered.

The combinations of the boundary conditions which lead to non vanishing fields are listed in the Table 4.1, where the corresponding combination of the wake potentials are also shown.

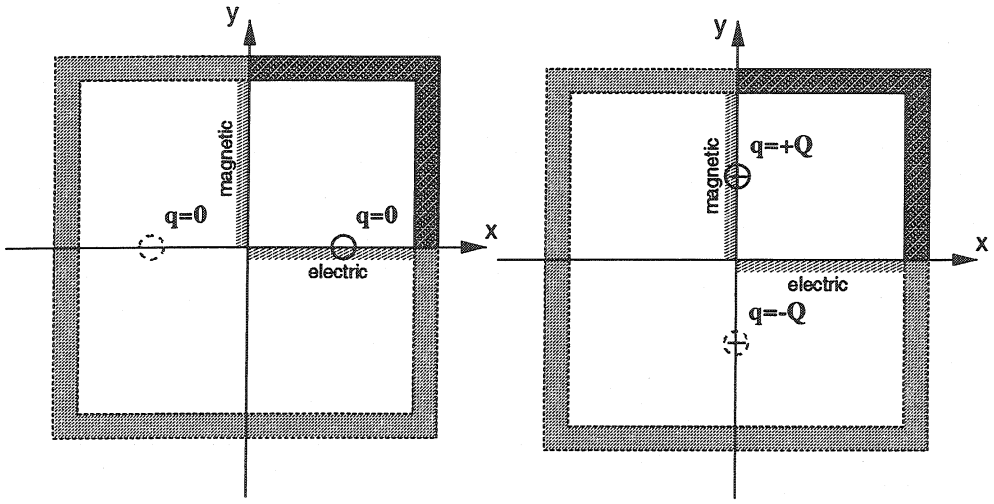

Figure 4.3: Image charges for vanishing horizontal resp. vertical beam-offset in a structure with 2 symmetry planes.

beam offset		xy boundaries				combination for
Δx	Δy	*ee*	*em*	*me*	*mm*	full structure
>0	>0	$\neq 0$	$\neq 0$	$\neq 0$	$\neq 0$	$w = (w_{ee} + w_{em} + w_{me} + w_{mm})/4$
$=0$	>0	$=0$	$\neq 0$	$=0$	$\neq 0$	$w = (w_{em} + w_{mm})/2$
>0	$=0$	$=0$	$=0$	$\neq 0$	$\neq 0$	$w = (w_{me} + w_{mm})/2$
$=0$	$=0$	$=0$	$=0$	$=0$	$\neq 0$	$w = w_{mm}$

Table 4.1: Combination of wake fields for different beam positions.

The results of the calculations with the full and the quarter structure for a cylindrical "pillbox" cavity with side-tubes are compared in Table 4.2. As expected, the agreement between full and quarter structure is very good. However, if one uses only part of a structure the post-processing effort increases, since one has to combine the resulting wake potentials resp. loss factors after the actual wake potential computation.

The wake potentials for transverse beam offsets which are outside the consid-

ered section can be obtained directly from symmetry considerations. Consider a beam offset of (x_a, y_a): The longitudinal wake potential for beam offsets of $(\pm x_a, \pm y_a)$ has the same magnitude and sign as the one for (x_a, y_a). The transverse wake potentials have to be multiplied by the sign of the corresponding offset, e.g the vertical wake potential changes its sign for negative vertical beam offsets, while it is independent of the sign of the horizontal offset.

Except for the 4 basic geometries, described in the next section, for which models of the full structures have been used[1], all structures investigated in later sections were computed taking advantage of their symmetry properties. This allows a more accurate modelling of the transverse profile, because for a given length of the traversing charge distribution, the longitudinal mesh size cannot be chosen arbitrary small, since one has to use several mesh-lines per r.m.s. length. For a given maximum number of total mesh-points, which is determined by the available computer resources, the transverse shape of the structure can be described more accurately using the symmetry properties of a structure, which leads to a better accuracy for the wake potentials.

[1]The size of the meshes for those full structures of those basic geometries are rather small. Therefore it was found advantageous to avoid the additional book keeping effort required for fractional meshes.

horizontal energy loss							
beam offset		quarter structure					full structure
Δx	Δy	$k_{x,ee}$	$k_{x,em}$	$k_{x,me}$	$k_{x,mm}$	k_x	k_x
mm	mm	V/C	V/C	V/C	V/C	V/C	V/C
0	0	0.000E+00	0.000E+00	0.000E+00	0.000E+00	0.000E+00	-1.698E-4
0	10	0.000E+00	0.000E+00	0.000E+00	0.000E+00	0.000E+00	-6.062E-4
10	10	2.202E+10	2.270E+11	-8.996E+09	-9.950E+09	5.571E+10	5.751E+10
vertical energy loss							
beam offset		quarter structure					full structure
Δx	Δy	$k_{x,ee}$	$k_{x,em}$	$k_{x,me}$	$k_{x,mm}$	k_x	k_x
mm	mm	V/C	V/C	V/C	V/C	V/C	V/C
0	0	0.000E+00	0.000E+00	0.000E+00	0.000E+00	0.000E+00	7.295E-04
0	10	0.000E+00	0.000E+00	1.214E+11	1.251E+10	6.693E+10	6.693E+10
10	10	2.202E+10	-8.996E+09	2.270E+11	-9.950E+09	5.571E+10	5.751E+10
longitudinal energy loss							
beam offset		quarter structure					full structure
Δx	Δy	$k_{x,ee}$	$k_{x,em}$	$k_{x,me}$	$k_{x,mm}$	k_x	k_x
mm	mm	V/C	V/C	V/C	V/C	V/C	V/C
0	0	0.000E+00	0.000E+00	0.000E+00	-2.070E+11	-2.070E+11	-2.070E+11
0	10	0.000E+00	0.000E+00	-2.532E+10	-4.148E+11	-2.201E+11	-2.201E+11
10	10	-2.179E+09	-4.835E+10	-4.835E+10	-8.255E+11	-2.311E+11	-2.311E+11

Table 4.2: Energy loss in a quadratic cavity (2 symmetry planes)

4.2 Basic Geometries

To understand the fundamental properties of wake potentials in 3 dimensional, non-rotationally-symmetric structures, four basic geometries were investigated. These structures are simple cavities with circular, quadratic, elliptic and rectangular cross-sections. The horizontal-to-vertical axis ratio of the elliptic and the rectangular cavity was chosen to be 2. The geometrical parameters are shown in Figure 4.4, the length of the cavities is 100 mm and the fields are excited by a Gaussian charge distribution with $\sigma = 20$ mm.

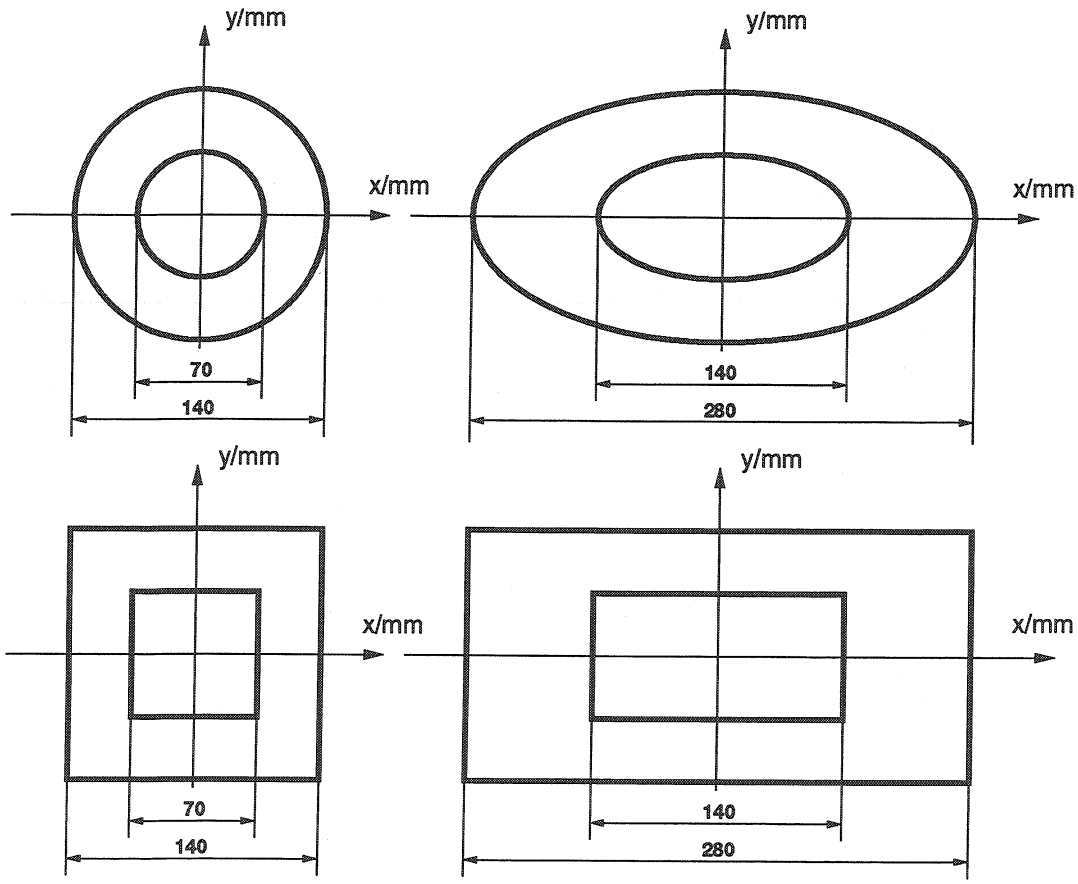

Figure 4.4: Basic geometries of "pillbox" cavity with side-tubes.

All wake field calculations for these and for the 3-dimensional structures in the following chapters were done with MAFIA[CST96] module T3 (3-dimensional time domain solver). The charge distribution used as excitation is shaped like a needle i.e. has no transverse extension. Therefore also higher multipole moments of the electromagnetic fields are excited. However, only the lowest

order field components yield significant contributions. This can be shown easily for axially symmetric structures, where the effects of the wake fields scale like $(b/a)^{2m}$ for the longitudinal and like $(b/a)^{2m-1}$ for the transverse case. Here a is the beam offset, b the beam pipe radius and m the order of the multipole component ([Cha93],§2.2).

The calculations were done for a number of horizontal and vertical offsets of the charge distribution. Depending on the number of offsets in the two transverse directions, one can calculate several multipole components of the resulting fields.

4.2.1 Circular Cross-Section

The geometry of the circular cavity is shown in Figure 4.5, and the parameters of the calculations are listed in Table 4.3. The longitudinal and transverse energy loss of a Gaussian beam for those beam-offsets are listed in Table 4.4 (page 41), and their graphical representations are shown on pages 42 and 43.

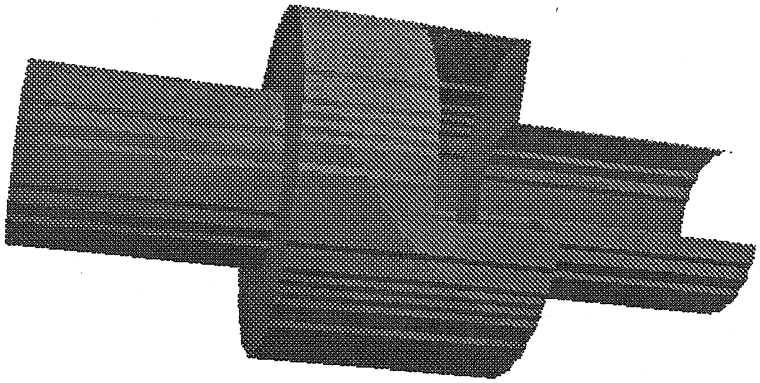

Figure 4.5: Cavity with circular cross section

Circular Cavity	
radius	70 mm
length	100 mm
Beam-pipe	
radius	35 mm
z_{in}	100 mm
z_{out}	100 mm
Beam	
σ	20 mm
total	$\pm 5\,\sigma$
offset	$\pm 0, 2.5, \ldots 10$mm

Table 4.3: Geometric properties

horizontal energy loss vs. transverse beam offset [V/nC]									
offset	x [mm]								
y [mm]	-10.	-7.5	-5.	-2.5	0	2.5	5.	7.5	10.
10.	-77.07	-55.94	-36.46	-17.99	0	17.99	36.46	55.94	77.07
7.5	-74.18	-53.86	-35.11	-17.33	0	17.33	35.11	53.86	74.18
5.	-72.17	-52.44	-34.19	-16.88	0	16.88	34.19	52.44	72.17
2.5	-70.98	-51.6	-33.66	-16.61	0	16.61	33.66	51.6	70.98
0	-70.59	-51.32	-33.48	-16.53	0	16.53	33.48	51.32	70.59
-2.5	-70.98	-51.6	-33.66	-16.61	0	16.61	33.66	51.6	70.98
-5.	-72.17	-52.44	-34.19	-16.88	0	16.88	34.19	52.44	72.17
-7.5	-74.18	-53.86	-35.11	-17.33	0	17.33	35.11	53.86	74.18
-10.	-77.07	-55.94	-36.46	-17.99	0	17.99	36.46	55.94	77.07
vertical energy loss vs. transverse beam offset [V/nC]									
offset	x [mm]								
y [mm]	-10.	-7.5	-5.	-2.5	0	2.5	5.	7.5	10.
10.	77.07	74.18	72.17	70.98	70.59	70.98	72.17	74.18	77.07
7.5	55.94	53.86	52.44	51.6	51.32	51.6	52.44	53.86	55.94
5.	36.46	35.11	34.19	33.66	33.48	33.66	34.19	35.11	36.46
2.5	17.99	17.33	16.88	16.61	16.53	16.61	16.88	17.33	17.99
0	0	0	0	0	0	0	0	0	0
-2.5	-17.99	-17.33	-16.88	-16.61	-16.53	-16.61	-16.88	-17.33	-17.99
-5.	-36.46	-35.11	-34.19	-33.66	-33.48	-33.66	-34.19	-35.11	-36.46
-7.5	-55.94	-53.86	-52.44	-51.6	-51.32	-51.6	-52.44	-53.86	-55.94
-10.	-77.07	-74.18	-72.17	-70.98	-70.59	-70.98	-72.17	-74.18	-77.07
longitudinal loss factor vs. transverse beam offset [V/nC]									
offset	x [mm]								
y [mm]	-10.	-7.5	-5.	-2.5	0	2.5	5.	7.5	10.
10.	-233.4	-227.7	-223.7	-221.3	-220.5	-221.3	-223.7	-227.7	-233.4
7.5	-227.7	-222.1	-218.2	-215.8	-215.1	-215.8	-218.2	-222.1	-227.7
5.	-223.7	-218.2	-214.3	-212.	-211.2	-212.	-214.3	-218.2	-223.7
2.5	-221.3	-215.8	-212.	-209.7	-208.9	-209.7	-212.	-215.8	-221.3
0	-220.5	-215.1	-211.2	-208.9	-208.1	-208.9	-211.2	-215.1	-220.5
-2.5	-221.3	-215.8	-212.	-209.7	-208.9	-209.7	-212.	-215.8	-221.3
-5.	-223.7	-218.2	-214.3	-212.	-211.2	-212.	-214.3	-218.2	-223.7
-7.5	-227.7	-222.1	-218.2	-215.8	-215.1	-215.8	-218.2	-222.1	-227.7
-10.	-233.4	-227.7	-223.7	-221.3	-220.5	-221.3	-223.7	-227.7	-233.4

Table 4.4: Longitudinal and transverse energy loss vs. transverse beam offset for a Gaussian bunch ($\sigma = 20$ mm) for a pillbox cavity with circular cross-section.

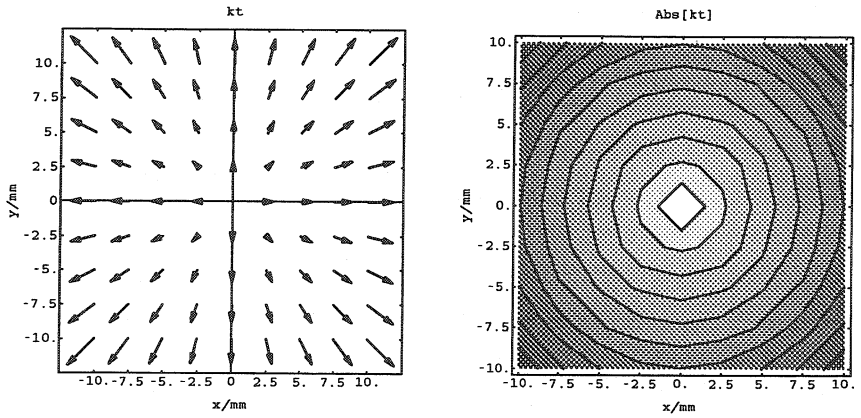

Figure 4.6: Circular cavity: vector- & contour-plot of transverse energy loss

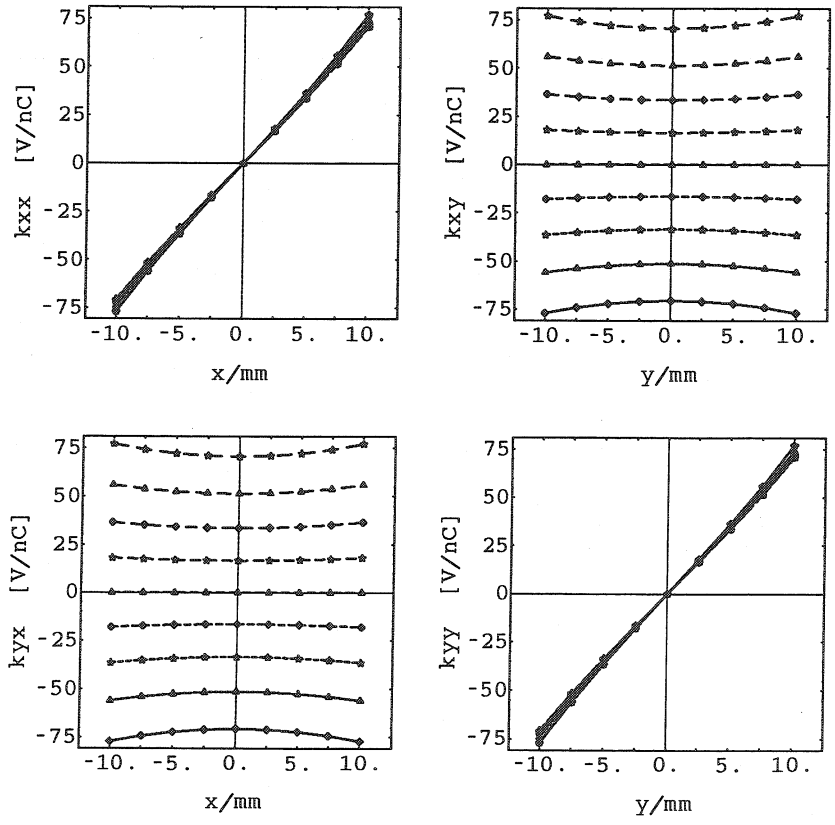

Figure 4.7: Circular cavity: transverse energy loss

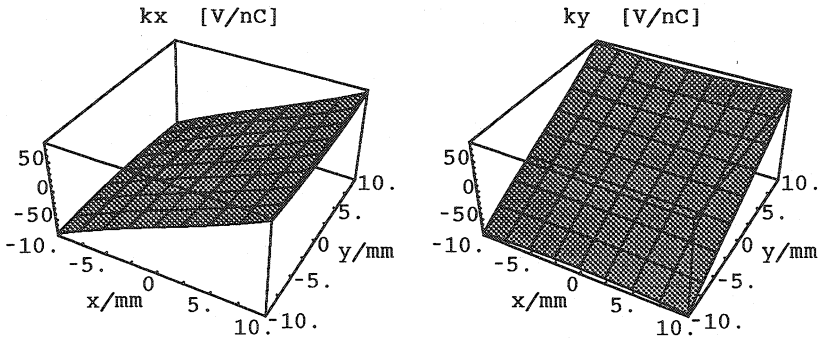

Figure 4.8: Circular cavity: horiz. and vert. energy loss (3-D)

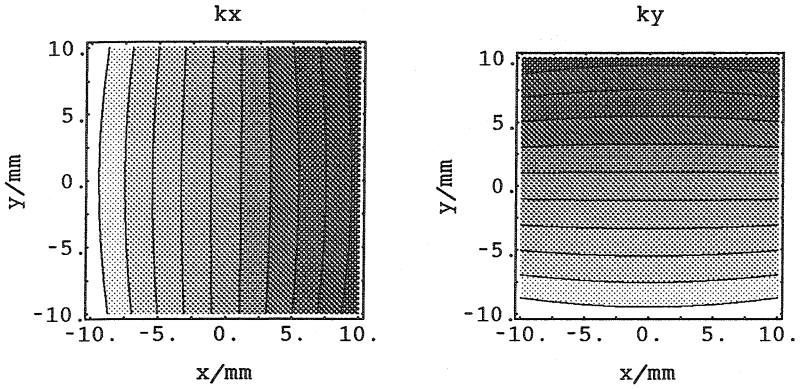

Figure 4.9: Circular cavity: horiz. and vert. energy loss (contour)

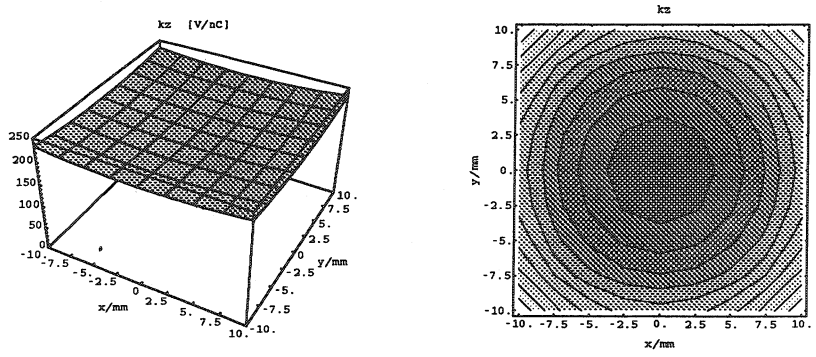

Figure 4.10: Circular cavity: longitudinal energy loss (3-D & contour)

4.2.2 Quadratic Cross-Section

The geometry of the quadratic cavity is shown in Figure 4.11, and the parameters of the calculations are listed in Table 4.5. The longitudinal and transverse energy loss of a Gaussian beam for those beam-offsets are listed in Table 4.6 (page 45), and their graphical representations are shown on pages 46 and 47.

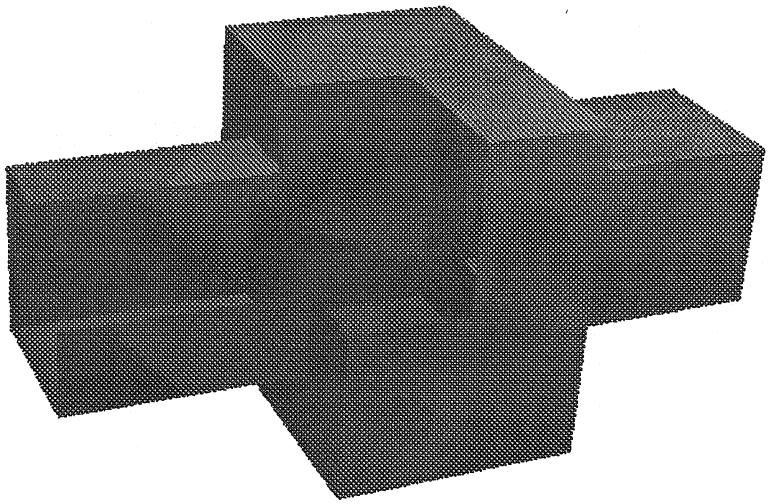

Figure 4.11: Cavity with quadratic cross section

Quadratic Cavity	
width	70 mm
length	100 mm
Beam-pipe	
width	35 mm
z_{in}	100 mm
z_{out}	100 mm
Beam	
σ	20 mm
total	$\pm 5\,\sigma$
offset	$\pm 0, 2.5, \ldots 10$mm

Table 4.5: Geometric properties

horizontal energy loss vs. transverse beam offset [V/nC]									
offset	x [mm]								
y [mm]	-10.	-7.5	-5.	-2.5	0	2.5	5.	7.5	10.
10.	-57.51	-40.27	-25.53	-12.38	0	12.38	25.53	40.27	57.51
7.5	-61.66	-43.36	-27.58	-13.4	0	13.4	27.58	43.36	61.66
5.	-64.59	-45.56	-29.04	-14.13	0	14.13	29.04	45.56	64.59
2.5	-66.34	-46.87	-29.92	-14.57	0	14.57	29.92	46.87	66.34
0	-66.93	-47.31	-30.21	-14.71	0	14.71	30.21	47.31	66.93
-2.5	-66.34	-46.87	-29.92	-14.57	0	14.57	29.92	46.87	66.34
-5.	-64.59	-45.56	-29.04	-14.13	0	14.13	29.04	45.56	64.59
-7.5	-61.66	-43.36	-27.58	-13.4	0	13.4	27.58	43.36	61.66
-10.	-57.51	-40.27	-25.53	-12.38	0	12.38	25.53	40.27	57.51
vertical energy loss vs. transverse beam offset [V/nC]									
offset	x [mm]								
y [mm]	-10.	-7.5	-5.	-2.5	0	2.5	5.	7.5	10.
10.	57.51	61.66	64.59	66.34	66.93	66.34	64.59	61.66	57.51
7.5	40.27	43.36	45.56	46.87	47.31	46.87	45.56	43.36	40.27
5.	25.53	27.58	29.04	29.92	30.21	29.92	29.04	27.58	25.53
2.5	12.38	13.4	14.13	14.57	14.71	14.57	14.13	13.4	12.38
0	0	0	0	0	0	0	0	0	0
-2.5	-12.38	-13.4	-14.13	-14.57	-14.71	-14.57	-14.13	-13.4	-12.38
-5.	-25.53	-27.58	-29.04	-29.92	-30.21	-29.92	-29.04	-27.58	-25.53
-7.5	-40.27	-43.36	-45.56	-46.87	-47.31	-46.87	-45.56	-43.36	-40.27
-10.	-57.51	-61.66	-64.59	-66.34	-66.93	-66.34	-64.59	-61.66	-57.51
longitudinal energy loss vs. transverse beam offset [V/nC]									
offset	x [mm]								
y [mm]	-10.	-7.5	-5.	-2.5	0	2.5	5.	7.5	10.
10.	-231.1	-226.1	-222.7	-220.7	-220.1	-220.7	-222.7	-226.1	-231.1
7.5	-226.1	-220.7	-217.1	-214.9	-214.2	-214.9	-217.1	-220.7	-226.1
5.	-222.7	-217.1	-213.2	-210.9	-210.1	-210.9	-213.2	-217.1	-222.7
2.5	-220.7	-214.9	-210.9	-208.5	-207.8	-208.5	-210.9	-214.9	-220.7
0	-220.1	-214.2	-210.1	-207.8	-207.	-207.8	-210.1	-214.2	-220.1
-2.5	-220.7	-214.9	-210.9	-208.5	-207.8	-208.5	-210.9	-214.9	-220.7
-5.	-222.7	-217.1	-213.2	-210.9	-210.1	-210.9	-213.2	-217.1	-222.7
-7.5	-226.1	-220.7	-217.1	-214.9	-214.2	-214.9	-217.1	-220.7	-226.1
-10.	-231.1	-226.1	-222.7	-220.7	-220.1	-220.7	-222.7	-226.1	-231.1

Table 4.6: Longitudinal and transverse energy loss vs. transverse beam offset for a Gaussian bunch ($\sigma = 20$ mm) for a pillbox cavity with quadratic cross-section.

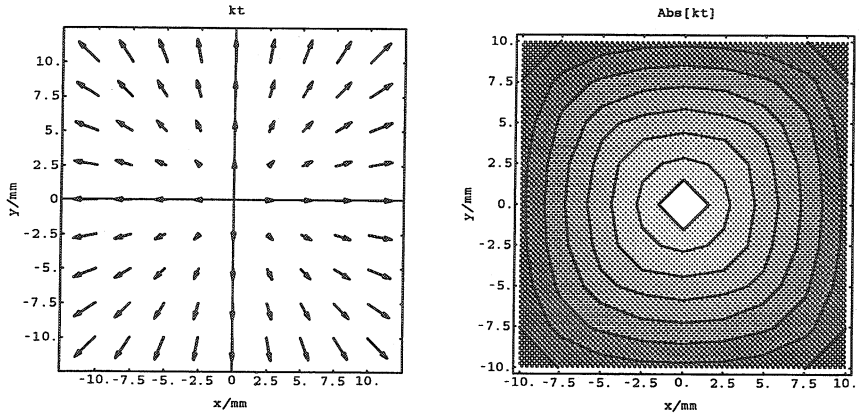

Figure 4.12: Quadr. cavity: vector & contour-plot of transverse energy loss

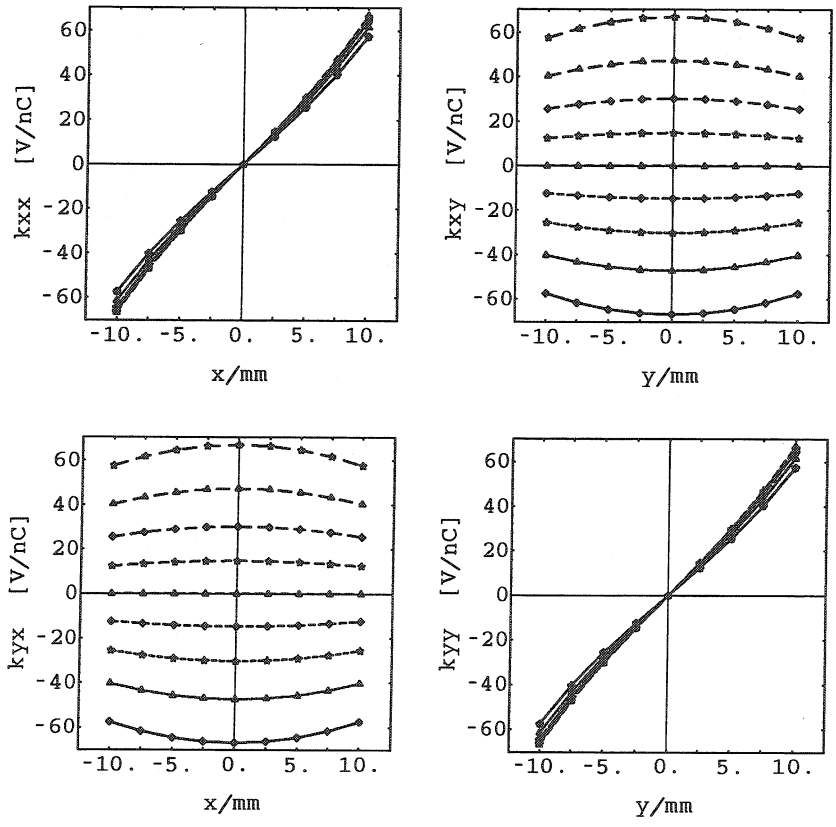

Figure 4.13: Quadratic cavity: transverse energy loss

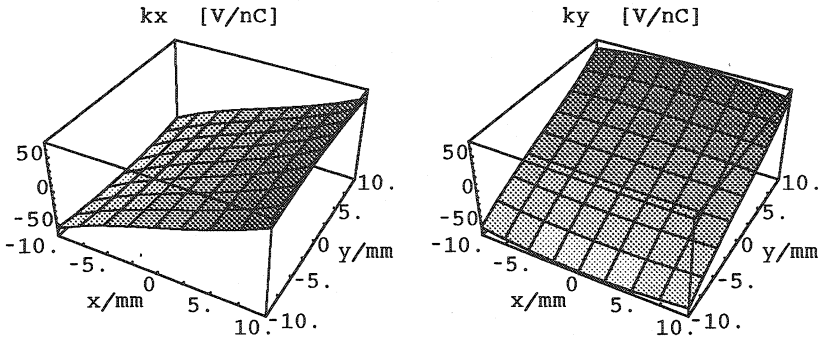

Figure 4.14: Quadratic cavity: horiz. & vert. energy loss (3-D)

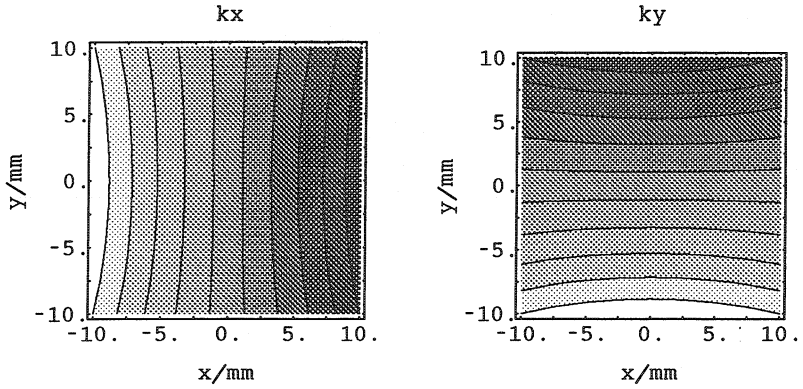

Figure 4.15: Quadratic cavity: horiz. & vert. energy loss (contour)

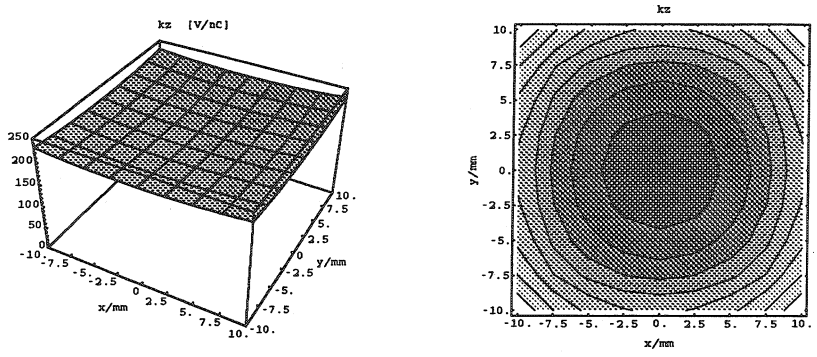

Figure 4.16: Quadratic cavity: longitudinal energy loss (3-D & contour)

4.2.3 Elliptic Cross-Section

The geometry of the elliptic cavity is shown in Figure 4.17, and the parameters of the calculations are listed in Table 4.7. The longitudinal and transverse loss of a Gaussian beam for those beam-offsets are listed in Table 4.8 (page 49), and their graphical representations are shown on pages 50 and 51.

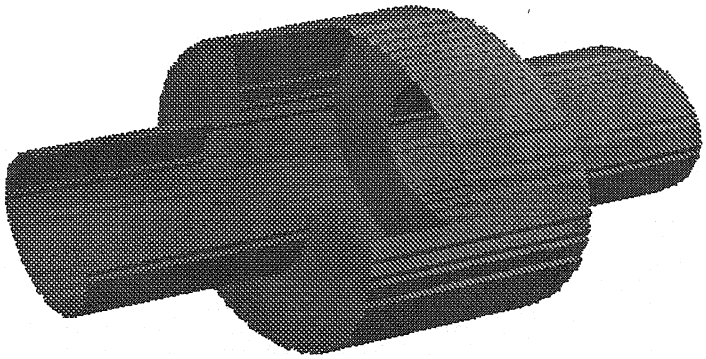

Figure 4.17: Cavity with elliptic cross section

Elliptic Cavity	
(x,y) - half axis	(140, 70) mm
length	100 mm
Beam-pipe	
(x,y) - half axis	(70, 35) mm
z_{in}	100 mm
z_{out}	100 mm
Beam	
σ	20 mm
total	$\pm 5\,\sigma$
offset	$\pm 0, 2.5, \ldots 10$mm

Table 4.7: Geometric properties

horizontal energy loss vs. transverse beam offset [V/nC]									
offset	x [mm]								
y [mm]	-10.	-7.5	-5.	-2.5	0	2.5	5.	7.5	10.
10.	-15.11	-11.16	-7.35	-3.65	0	3.65	7.35	11.16	15.11
7.5	-13.94	-10.33	-6.82	-3.39	0	3.39	6.82	10.33	13.94
5.	-13.14	-9.74	-6.44	-3.2	0	3.2	6.44	9.74	13.14
2.5	-12.67	-9.4	-6.22	-3.09	0	3.09	6.22	9.4	12.67
0	-12.51	-9.29	-6.14	-3.06	0	3.06	6.14	9.29	12.51
-2.5	-12.67	-9.4	-6.22	-3.09	0	3.09	6.22	9.4	12.67
-5.	-13.14	-9.74	-6.44	-3.2	0	3.2	6.44	9.74	13.14
-7.5	-13.94	-10.33	-6.82	-3.39	0	3.39	6.82	10.33	13.94
-10.	-15.11	-11.16	-7.35	-3.65	0	3.65	7.35	11.16	15.11
vertical energy loss vs. transverse beam offset [V/nC]									
offset	x [mm]								
y [mm]	-10.	-7.5	-5.	-2.5	0	2.5	5.	7.5	10.
10.	87.13	85.96	85.18	84.74	84.59	84.74	85.18	85.96	87.13
7.5	63.58	62.74	62.16	61.82	61.72	61.82	62.16	62.74	63.58
5.	41.59	41.04	40.66	40.44	40.36	40.44	40.66	41.04	41.59
2.5	20.56	20.29	20.1	19.99	19.95	19.99	20.1	20.29	20.56
0	0	0	0	0	0	0	0	0	0
-2.5	-20.56	-20.29	-20.1	-19.99	-19.95	-19.99	-20.1	-20.29	-20.56
-5.	-41.59	-41.04	-40.66	-40.44	-40.36	-40.44	-40.66	-41.04	-41.59
-7.5	-63.58	-62.74	-62.16	-61.82	-61.72	-61.82	-62.16	-62.74	-63.58
-10.	-87.13	-85.96	-85.18	-84.74	-84.59	-84.74	-85.18	-85.96	-87.13
longitudinal energy loss vs. transverse beam offset [V/nC]									
offset	x [mm]								
y [mm]	-10.	-7.5	-5.	-2.5	0	2.5	5.	7.5	10.
10.	-214.8	-212.8	-211.4	-210.6	-210.3	-210.6	-211.4	-212.8	-214.8
7.5	-206.8	-204.9	-203.6	-202.8	-202.5	-202.8	-203.6	-204.9	-206.8
5.	-201.2	-199.3	-198.1	-197.3	-197.	-197.3	-198.1	-199.3	-201.2
2.5	-197.8	-196.	-194.8	-194.	-193.8	-194.	-194.8	-196.	-197.8
0	-196.7	-194.9	-193.7	-192.9	-192.7	-192.9	-193.7	-194.9	-196.7
-2.5	-197.8	-196.	-194.8	-194.	-193.8	-194.	-194.8	-196.	-197.8
-5.	-201.2	-199.3	-198.1	-197.3	-197.	-197.3	-198.1	-199.3	-201.2
-7.5	-206.8	-204.9	-203.6	-202.8	-202.5	-202.8	-203.6	-204.9	-206.8
-10.	-214.8	-212.8	-211.4	-210.6	-210.3	-210.6	-211.4	-212.8	-214.8

Table 4.8: Longitudinal and transverse energy loss vs. transverse beam offset for a Gaussian bunch ($\sigma = 20$ mm) for a pillbox cavity with elliptic cross-section.

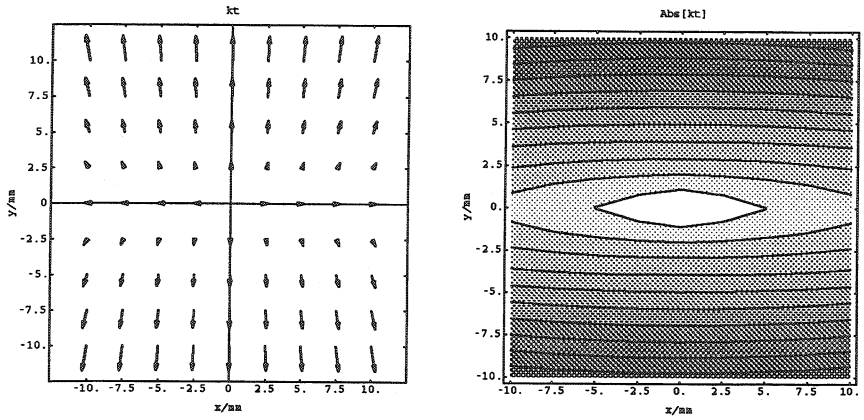

Figure 4.18: Elliptic cavity: vector- & contourplot of transverse energy loss

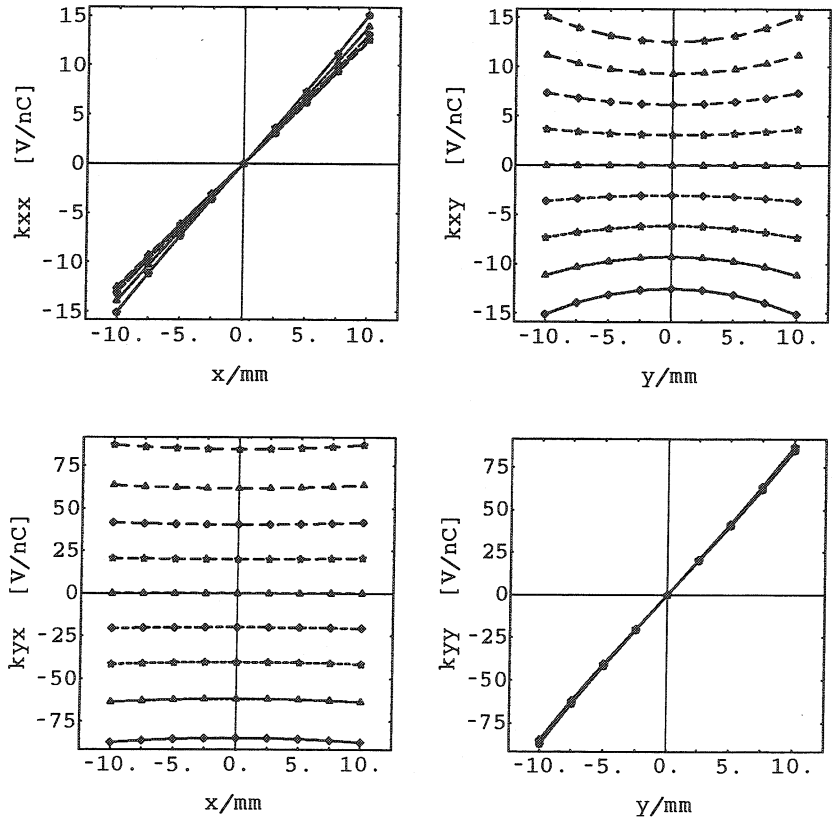

Figure 4.19: Elliptic cavity: transverse energy loss

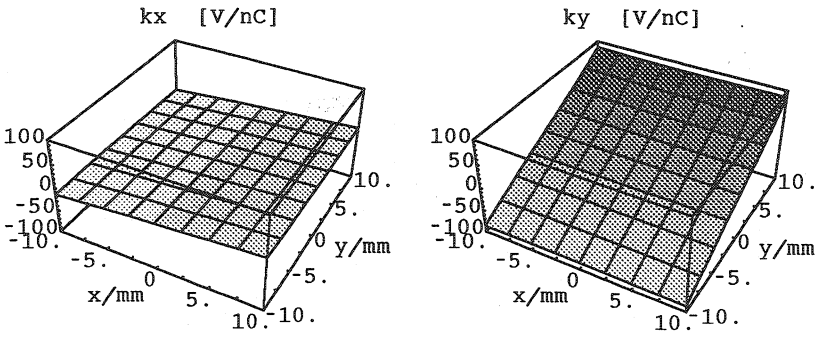

Figure 4.20: Elliptic cavity: horiz. & vert. energy loss (3-D)

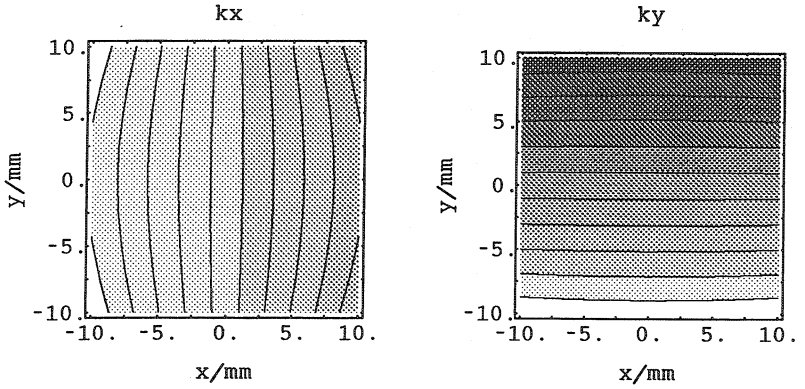

Figure 4.21: Elliptic cavity: horiz. & vert. energy loss (contour)

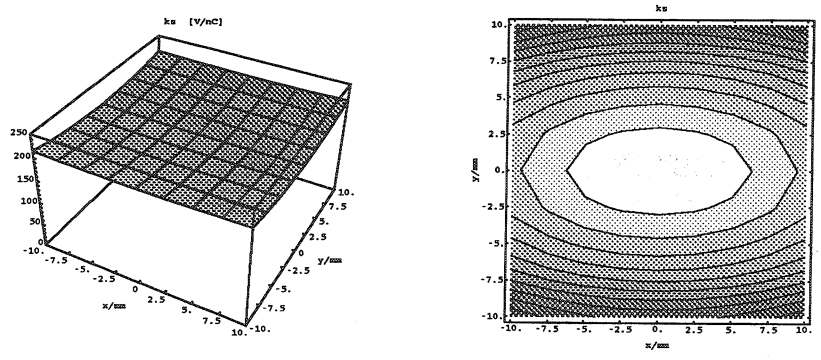

Figure 4.22: Elliptic cavity: longitudinal energy loss (3-D & contour)

4.2.4 Rectangular Cross-Section

The geometry of the rectangular cavity is shown in Figure 4.23, and the parameters of the calculations are listed in Table 4.9. The longitudinal and transverse loss of a Gaussian beam for those beam-offsets are listed in Table 4.10 (page 53), and their graphical representations are shown on pages 54 and 55.

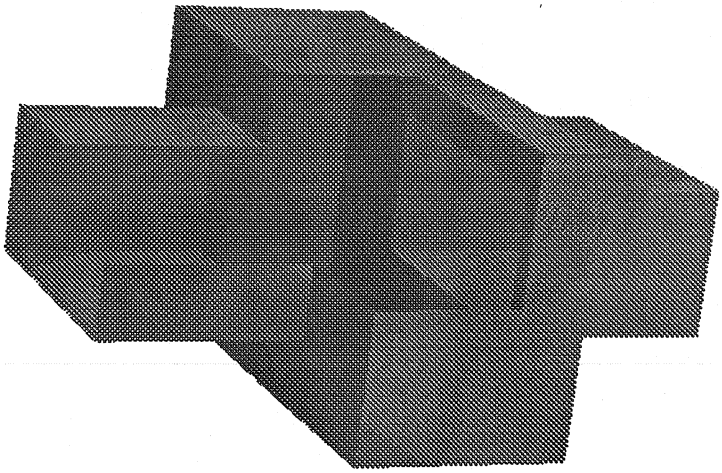

Figure 4.23: Cavity with rectangular cross section

Rectangular Cavity	
(x,y) - width	$(140, 70)$ mm
length	100 mm
Beam-pipe	
(x,y) - width	$(70, 35)$ mm
z_{in}	100 mm
z_{out}	100 mm
Beam	
σ	20 mm
total	$\pm 5\,\sigma$
offset	$\pm 0, 2.5, \ldots 10$mm

Table 4.9: Geometric properties

horizontal energy loss vs. transverse beam offset [V/nC]									
offset	x [mm]								
y [mm]	-10.	-7.5	-5.	-2.5	0	2.5	5.	7.5	10.
10.	-1.13	-0.72	-0.42	-0.19	0	0.19	0.42	0.72	1.13
7.5	-1.39	-0.9	-0.54	-0.25	0	0.25	0.54	0.9	1.39
5.	-1.59	-1.04	-0.63	-0.29	0	0.29	0.63	1.04	1.59
2.5	-1.71	-1.13	-0.68	-0.32	0	0.32	0.68	1.13	1.71
0	-1.75	-1.16	-0.7	-0.33	0	0.33	0.7	1.16	1.75
-2.5	-1.71	-1.13	-0.68	-0.32	0	0.32	0.68	1.13	1.71
-5.	-1.59	-1.04	-0.63	-0.29	0	0.29	0.63	1.04	1.59
-7.5	-1.39	-0.9	-0.54	-0.25	0	0.25	0.54	0.9	1.39
-10.	-1.13	-0.72	-0.42	-0.19	0	0.19	0.42	0.72	1.13
vertical energy loss vs. transverse beam offset [V/nC]									
offset	x [mm]								
y [mm]	-10.	-7.5	-5.	-2.5	0	2.5	5.	7.5	10.
10.	87.42	87.67	87.83	87.93	87.96	87.93	87.83	87.67	87.42
7.5	63.58	63.77	63.9	63.98	64.01	63.98	63.9	63.77	63.58
5.	41.48	41.61	41.71	41.76	41.78	41.76	41.71	41.61	41.48
2.5	20.47	20.54	20.59	20.62	20.63	20.62	20.59	20.54	20.47
0	0	0	0	0	0	0	0	0	0
-2.5	-20.47	-20.54	-20.59	-20.62	-20.63	-20.62	-20.59	-20.54	-20.47
-5.	-41.48	-41.61	-41.71	-41.76	-41.78	-41.76	-41.71	-41.61	-41.48
-7.5	-63.58	-63.77	-63.9	-63.98	-64.01	-63.98	-63.9	-63.77	-63.58
-10.	-87.42	-87.67	-87.83	-87.93	-87.96	-87.93	-87.83	-87.67	-87.42
longitudinal energy loss vs. transverse beam offset [V/nC]									
offset	x [mm]								
y [mm]	-10.	-7.5	-5.	-2.5	0	2.5	5.	7.5	10.
10.	-205.4	-205.	-204.7	-204.6	-204.5	-204.6	-204.7	-205.	-205.4
7.5	-197.1	-196.6	-196.3	-196.2	-196.1	-196.2	-196.3	-196.6	-197.1
5.	-191.3	-190.8	-190.5	-190.3	-190.2	-190.3	-190.5	-190.8	-191.3
2.5	-187.8	-187.3	-187.	-186.8	-186.7	-186.8	-187.	-187.3	-187.8
0	-186.6	-186.1	-185.8	-185.6	-185.5	-185.6	-185.8	-186.1	-186.6
-2.5	-187.8	-187.3	-187.	-186.8	-186.7	-186.8	-187.	-187.3	-187.8
-5.	-191.3	-190.8	-190.5	-190.3	-190.2	-190.3	-190.5	-190.8	-191.3
-7.5	-197.1	-196.6	-196.3	-196.2	-196.1	-196.2	-196.3	-196.6	-197.1
-10.	-205.4	-205.	-204.7	-204.6	-204.5	-204.6	-204.7	-205.	-205.4

Table 4.10: Longitudinal and transverse energy losses vs. transverse beam offset for a Gaussian bunch ($\sigma = 20$ mm) for a pillbox cavity with rectangular cross-section.

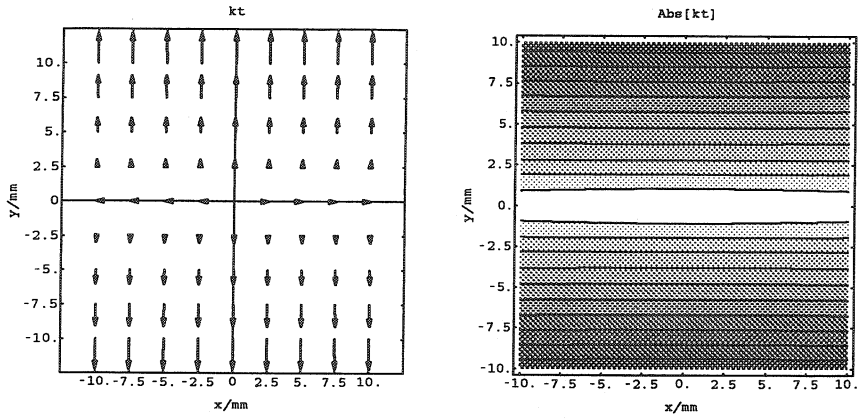

Figure 4.24: Rect. cavity: vector- & contour-plot of transverse energy loss

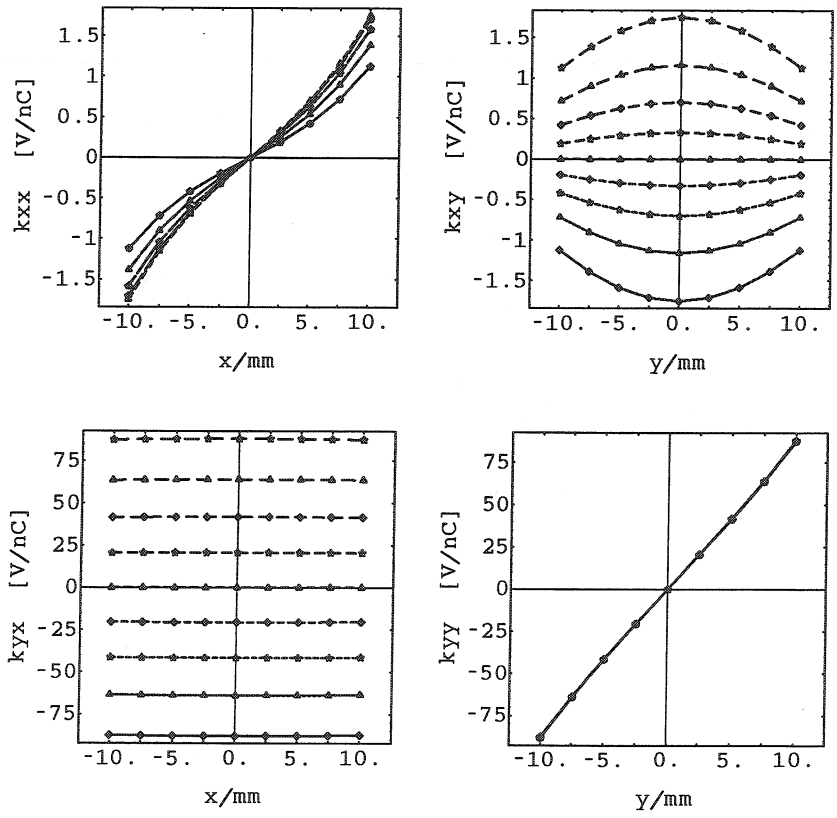

Figure 4.25: Rectangular cavity: transverse energy loss

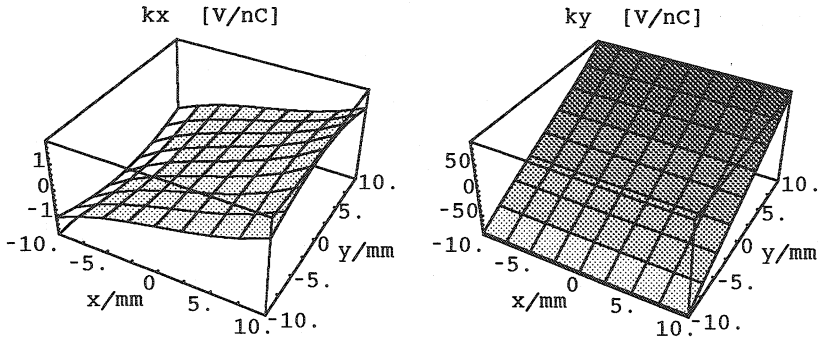

Figure 4.26: Rectangular cavity: horiz. & vert. energy loss (3-D)

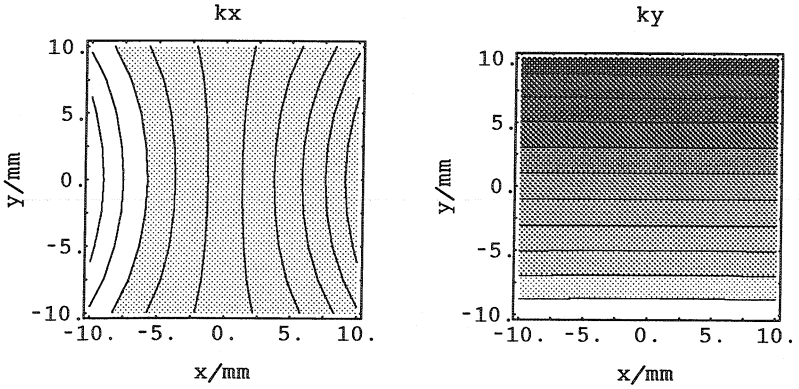

Figure 4.27: Rectangular cavity: horiz. & vert. energy loss (contour)

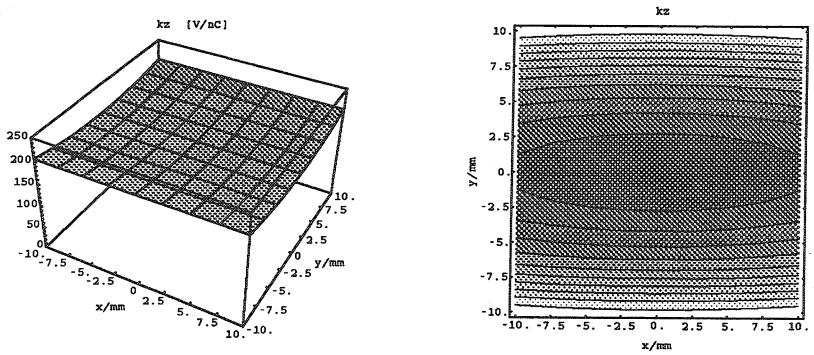

Figure 4.28: Rectangular cavity: longitudinal energy loss (3-D & contour)

4.2.5 Comparison of the 4 Basic Geometries

Comparison of the loss factors

The main components of the loss factors in the 3 spatial dimensions for the 4 basic geometries are summarised in Table 4.11. The loss factors for the cylinder symmetric (circular) structure calculated with ABCI[Chi94] are quoted for comparison (indicated as 2-D). Taking into account that the structure modelled using a Cartesian mesh can describe it only approximately, the agreement between the 2-D and 3-D calculation is quite good.

	main loss factor components								
basic	horizontal			vertical			longitudinal		
geom.	k_x	k_{x^3}	k_{xy^2}	k_y	k_{y^3}	k_{yx^2}	$k_{\parallel}$	$k_{\parallel x^2}$	$k_{\parallel y^2}$
	V/pCm	V/pCm^3	V/pCm^3	V/pCm	V/pCm^3	V/pCm^3	V/pC	V/pCm^2	V/pCm^2
circ.(3-D)	6.580	3796.2	5577.5	6.580	3796.2	5577.5	0.2081	122.5	122.5
circ.(2-D)	6.488	—	—	6.488	—	—	0.2065	120.4	120.4
quad.	5.830	7389.5	-9298.2	5.830	7389.5	-9298.2	0.2070	124.6	124.6
elli.	1.221	305.4	2281.0	7.948	3877.7	2295.1	0.1927	39.8	173.8
rect.	0.129	399.6	-588.5	8.214	4615.7	-585.9	0.1855	-10.36	-185.8

Table 4.11: Main components of loss factor for the basic geometries

The loss factor components k_x, k_y resp. $k_{\parallel}$ are equivalent to the transverse loss factor $k_{\perp}$ (azimuthal order $m = 1$) resp. the longitudinal loss factor (azimuthal order $m = 0$). The longitudinal components $k_{\parallel x^2}$ and $k_{\parallel y^2}$ correspond to the longitudinal loss of the dipole component $m = 1$. The strongest transverse components, besides the linear loss factors, were found to be k_{x^3}, k_{y^3} and k_{xy^2}, k_{yx^2} for all geometries. These last two terms take into account the wake field coupling between the two transverse planes. The values of those components, as well as the relative contributions of the main components, to the losses of a beam with a (x, y) offset of $(5, 5)$ mm, are shown in Figure 4.29. The contributions of the remaining components are below a few per-mil, and for better visibility only the main contributions are displayed.

As can be seen from Table 4.11, the variation of the longitudinal loss factor for the 4 geometries is within a range of only 5%. The vertical loss k_y shows already a quite significant variation of about 30%, whereas the horizontal loss and the higher order transverse components of the loss shows almost no correlation. The transverse cross coupling terms k_{xy^2}, k_{yx^2} even change sign depending on the specific geometry, but they have almost the same value for both transverse

directions for each geometry.

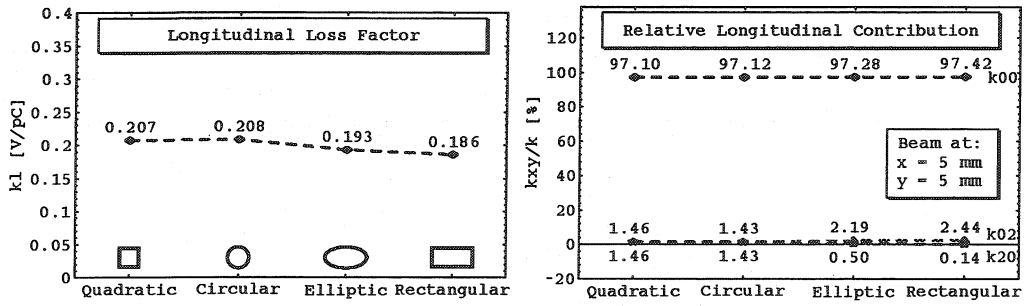

Figure 4.29: Longitudinal loss factors of the 4 basic geometries and relative contributions to the longitudinal losses for $(5, 5)$ mm (x, y) beam offset.

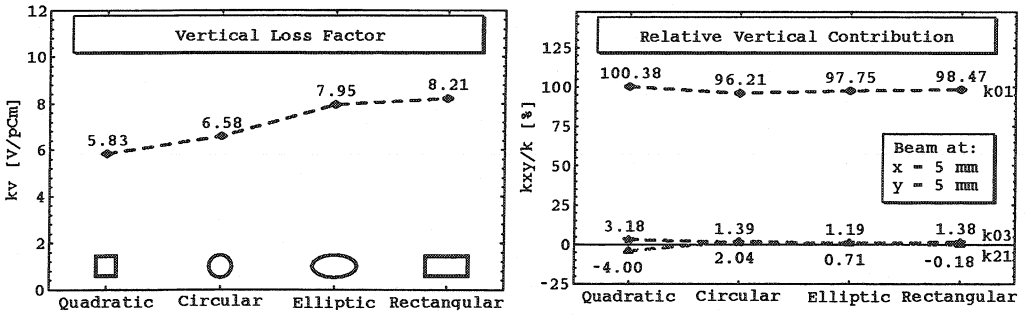

Figure 4.30: Vertical loss factors of the 4 basic geometries and relative contributions to the vertical losses for $(5, 5)$ mm (x, y) beam offset.

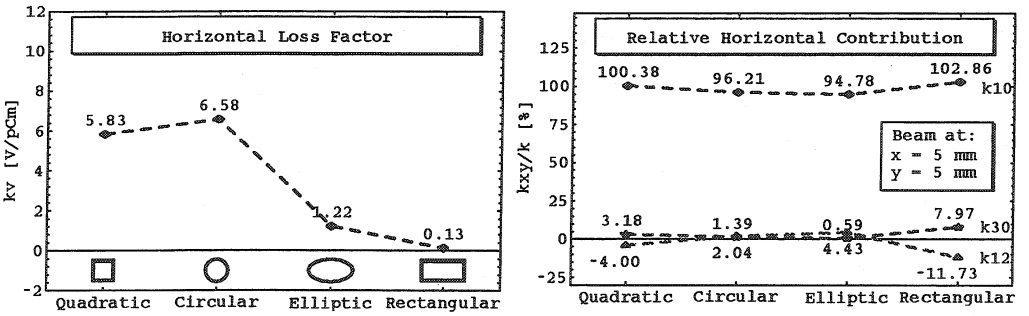

Figure 4.31: Horizontal loss factors of the 4 basic geometries and relative contributions to their horizontal losses for $(5, 5)$ mm (x, y) beam offset.

Comparison of the wake potentials

The loss factors for the 4 basic geometries were compared in the last section. To point out the differences of those geometries, the wake-potentials yield further information. Even though the longitudinal loss factors were not very different for the 4 structures, the corresponding wake potentials (shown in Figure 4.32 show quite significant differences in their long range behaviour. The wake

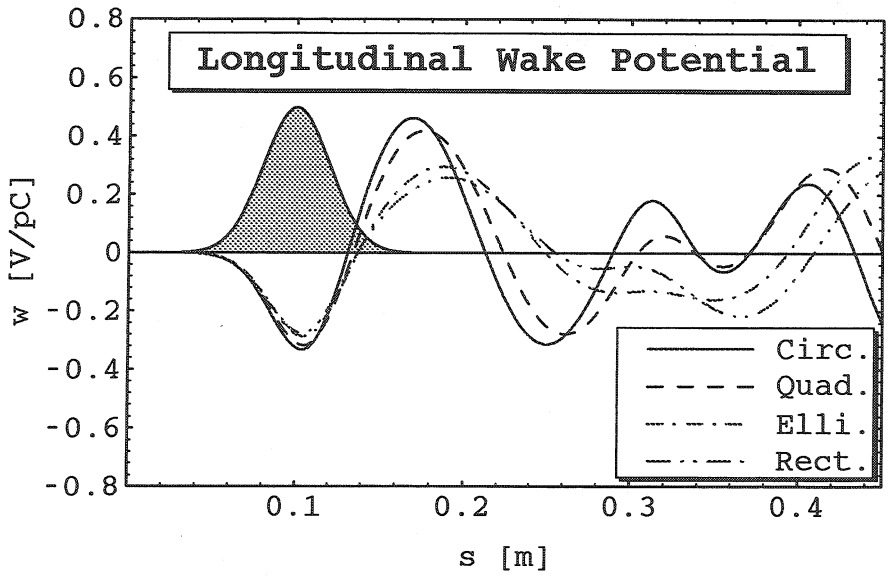

Figure 4.32: Longitudinal wake potentials of the 4 basic geometries.

potentials of the circular and the quadratic structures on the one hand, and those of the elliptic and rectangular structures on the other hand, are quite similar to each other. Since the longitudinal wake potential is approximately proportional to the volume of a structure this is not too surprising. Therefore one can deduce that for longitudinal impedance considerations the results do not depend critically on the geometry as long as the volume stays about the same. This argument does not hold any longer for the transverse effects. Here the wake potentials depend more critically on the actual transverse shape. Especially the horizontal wake potential cannot be estimated easily from 2-D calculations. This can be seen in Figure 4.33.

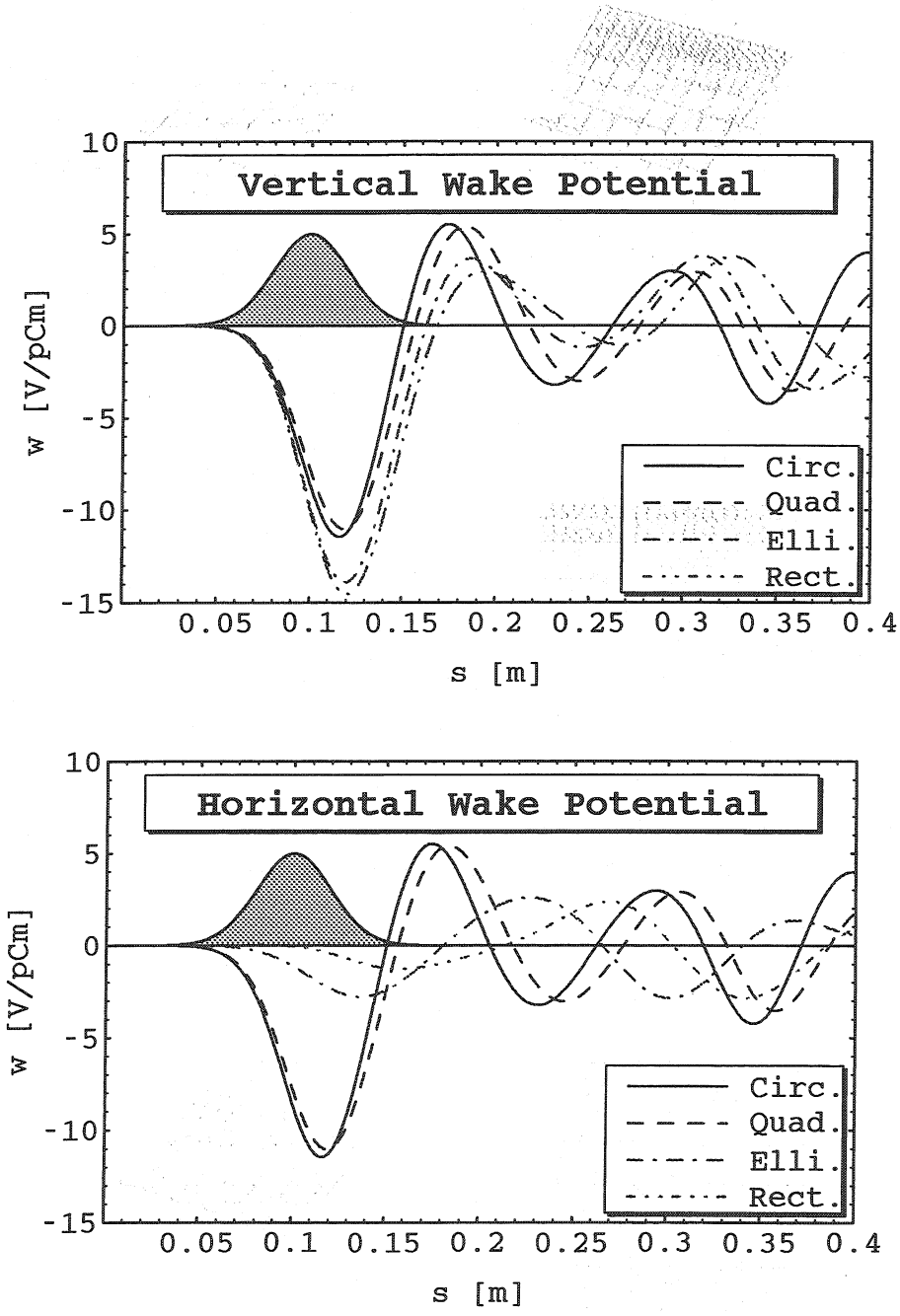

Figure 4.33: Transverse wake potentials of the 4 basic geometries.

4.3 Rectangular Cavity - Varying Axes Ratio

For these basic geometries, the ratio of horizontal to vertical loss factor varies over a wide range, depending on the cross section of the structure. To examine the behaviour of the wake potentials, a rectangular cavity with quadratic side-tubes was investigated. The quadratic side-tubes (beam pipe) have a width of 50 mm and a length of 100 mm. The horizontal and vertical cavity depth will be varied over a range of 0 to 100 mm in steps of 2 mm.

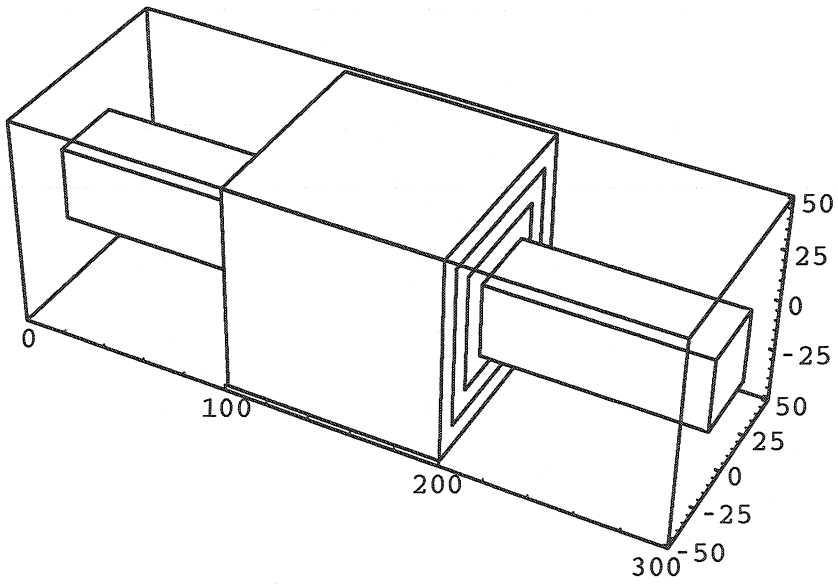

Figure 4.34: Rectangular "pillbox" cavity - varying size.

4.3.1 Loss Factors as Function of the Cavity Depth

The loss factors in the 3 transverse dimensions for the different axis ratios of the rectangular cavity are shown in Fig. 4.36. The loss factor in one transverse direction may become negative if the cavity depth is smaller in this direction. The magnitude of the negative loss factor is largest for zero cavity depth in

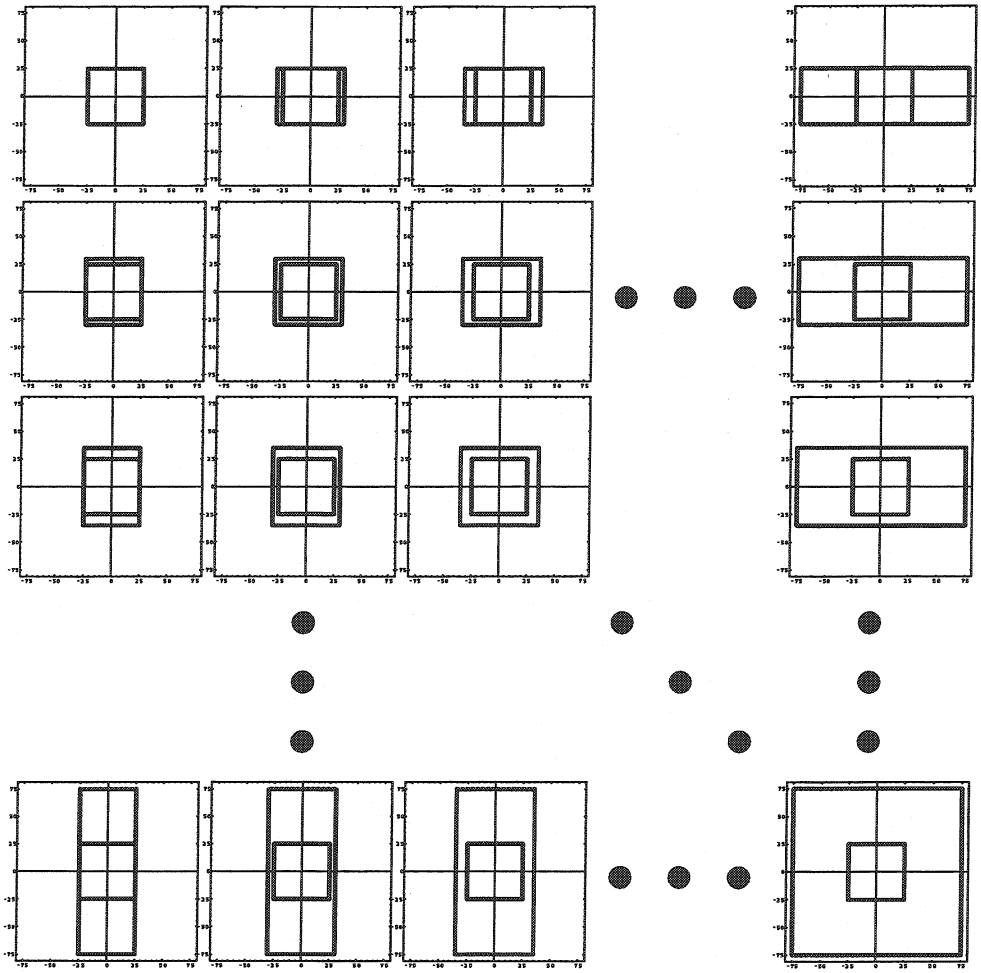

Figure 4.35: Rectangular cavity - varying transverse cavity depth.

the corresponding direction. For a small cavity depth in one direction also the longitudinal loss factor stays rather small.

For accelerators whose performance is limited due to transverse impedance, this limitation usually occurs only in one of the two transverse directions, such as the vertical one for LEP. By installing elements, with geometries optimised to achieve a large negative loss factor in the problematic direction, one could thus actually reduce the total loss factors in the vertical direction, and thereby increase the threshold current of the vertical transverse mode coupling instability (TMCI).

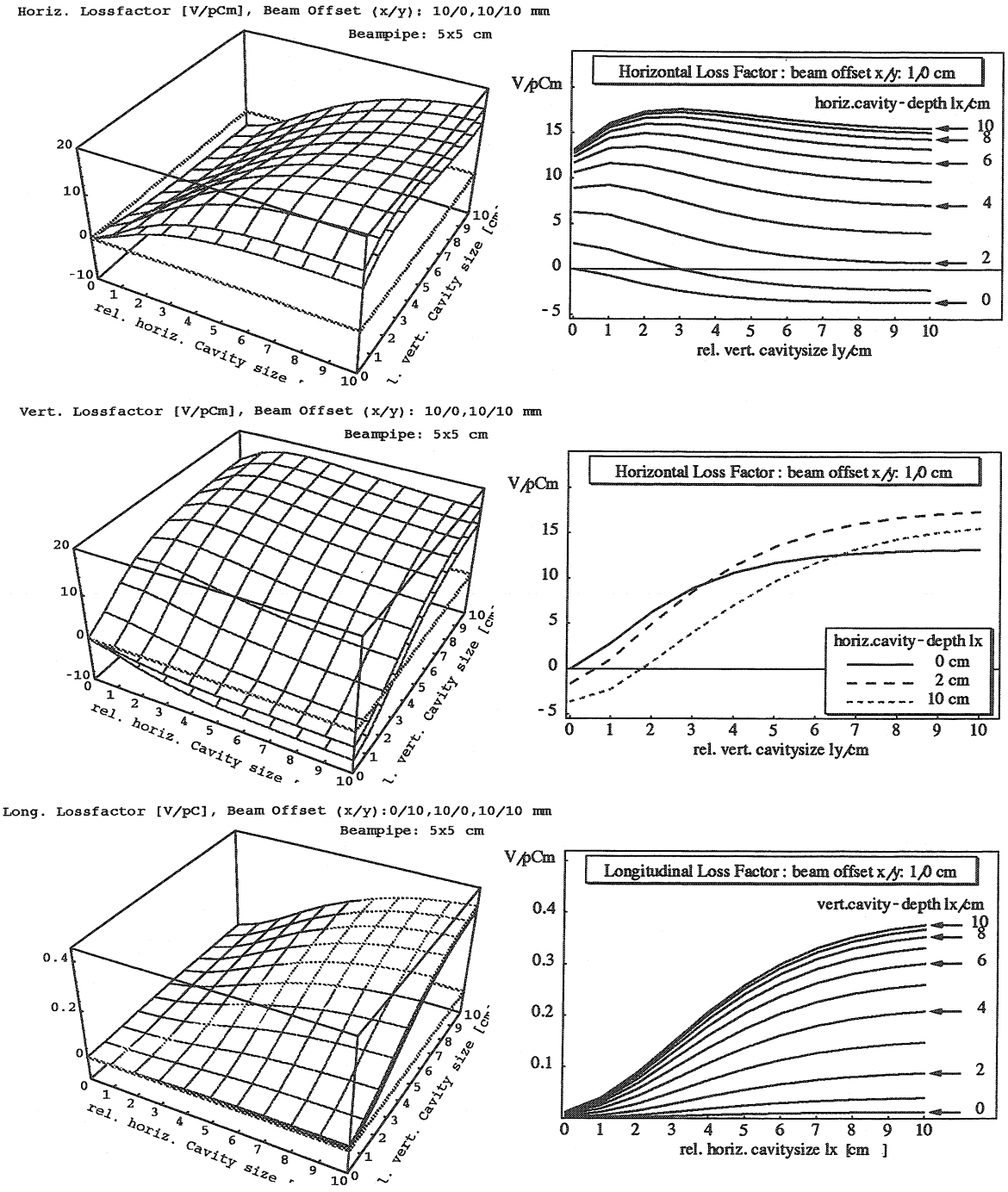

Figure 4.36: Loss factors of a rectangular cavity as function of horizontal and vertical cavity depth for a Gaussian bunch $\sigma = 20$ mm.

4.4 LEP - Shielded Bellows

The RF-shields of the elliptic bellows in the arc-sections of LEP have a rather small cross section variation. Their transverse wake potentials are therefore rather small. Nevertheless, since they are very numerous their contribution to the vertical impedance of LEP is important ([WE96] §5).

To study the influence of the slots between the *sliding fingers* of the bellows shielding, a rectangular model was used first. This geometry was chosen to allow a more accurate description of the slots.

4.4.1 Rectangular Model of LEP-Bellows

The geometry of the rectangular model of the bellows is shown in Figure 4.37. This figure shows the vertical dimensions of the structure. In the horizontal plane the width of the beam-pipe is larger (130 mm) while the variation of the bellows shielding is the same. The length of the slots is 70 mm, and their

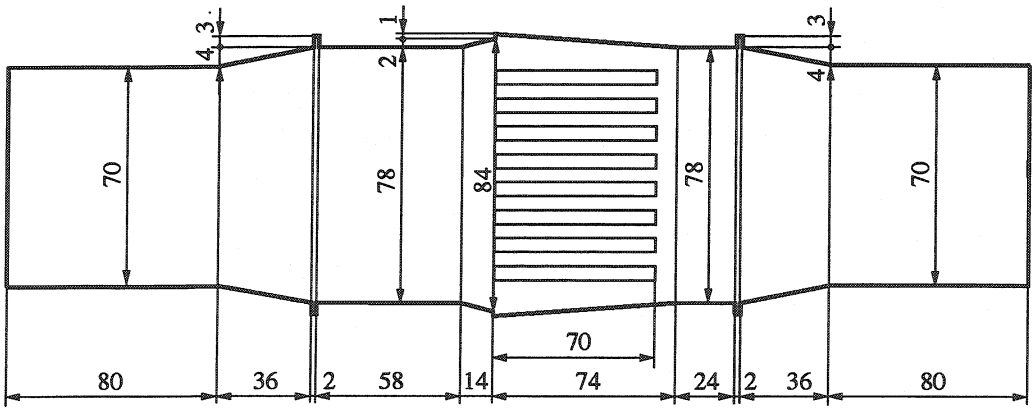

Figure 4.37: Rectangular model used to investigate the influence of the slots between the sliding contact fingers of the shielded bellows.

longitudinal location can be seen in Figure 4.37. The number of slots is varied, while the total area remains the same (i.e. the fewer the slots the bigger their width). The transverse positions of the slots along the cross sections of the 4 models are shown in Figure 4.38. The exact positions of the slots are specified in Table 4.12.

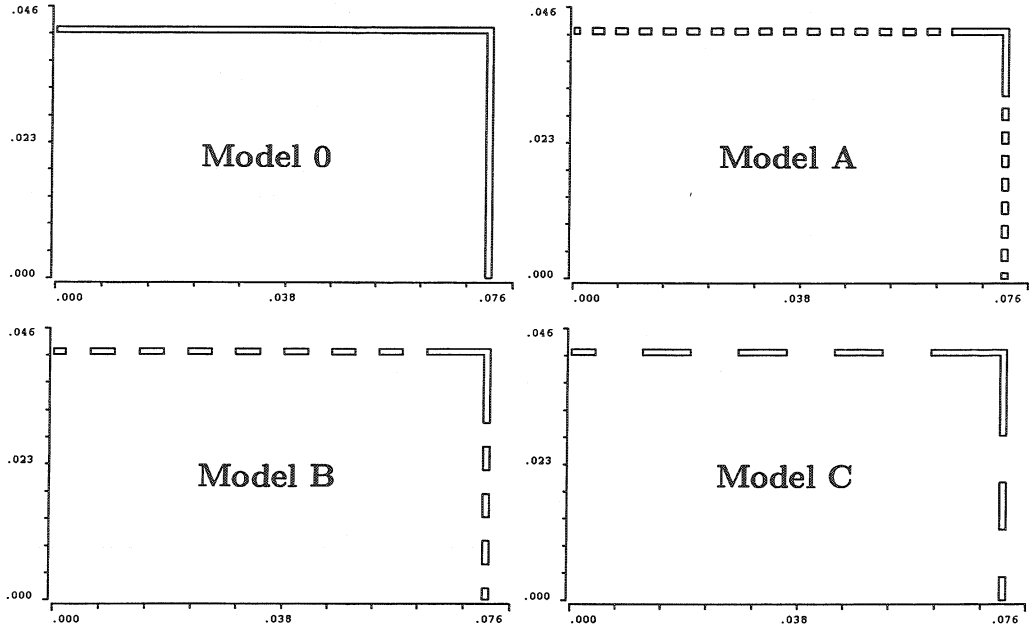

Figure 4.38: Cross sections of the 4 rectangular bellows models.

	horizontal slots				vertical slots			
bellows model	nr.	width	first	interval	nr.	width	first	interval
	—	x_s/mm	x_1/mm	dx/mm	—	y_s/mm	y_1/mm	dy/mm
Model C	8	8	±8	16	4	8	±8	16
Model B	16	4	±4	8	8	4	±4	8
Model A	32	2	±2	4	16	2	±2	4
Model 0	0	—	—	—	0	—	—	—

Table 4.12: Transverse position, width and intervals of the slots between the *sliding fingers* for the rectangular shielded bellows models.

Model 0 without slots: transverse energy loss vs. beam offset

The losses of a Gaussian beam of $\sigma = 20$ mm for horizontal resp. vertical beam offsets from -6 to $+6$ mm in steps of 2 mm were calculated for the 4 rectangular models. Since the absolute values and the offset-dependence of the losses for those 4 models are very similar, this dependence is shown only for the rectangular model without slots (i.e. Model 0). The results for the 3 other models can be seen below when the 4 models are compared with each other.

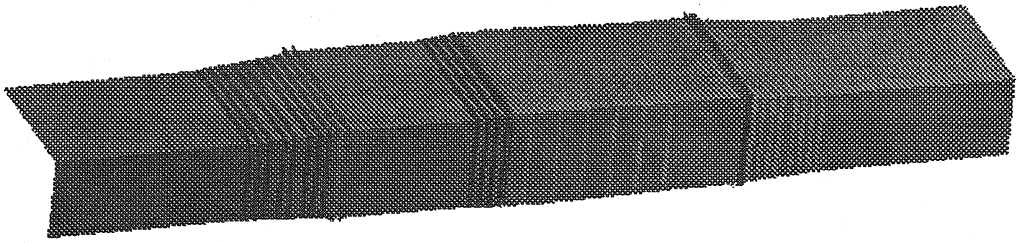

Figure 4.39: Rectangular model of LEP shielded bellows without slots.

The transverse energy loss in the 3 spatial directions for a Gaussian beam with $\sigma = 20mm$ are listed in Table 4.13 on page 66, the horizontal resp. vertical beam offsets vary from -6 to 6 mm in steps of 2 mm. The graphical representations are shown in Figures 4.40 - 4.43 on pages 67 and 68.

An interesting phenomenon can be seen clearly in the vector-plot of the transverse energy loss (Fig. 4.40). The horizontal kicks point inwards, which means that the energy loss has a negative sign, which corresponds to a focusing effect of the horizontal wake fields. This interesting effect can appear for non axially symmetric structures and is further examined in the section 4.3.

horizontal energy loss vs. transverse beam offset [V/nC]							
offset	x [mm]						
y [mm]	-6.0	-4.0	-2.0	0.0	2.0	4.0	6.0
6.0	0.236	0.172	0.093	0.000	-0.093	-0.172	-0.236
4.0	0.228	0.166	0.089	0.000	-0.089	-0.166	-0.228
2.0	0.223	0.162	0.087	0.000	-0.087	-0.162	-0.223
0.0	0.221	0.161	0.087	0.000	-0.087	-0.161	-0.221
-2.0	0.223	0.162	0.087	0.000	-0.087	-0.162	-0.223
-4.0	0.228	0.166	0.089	0.000	-0.089	-0.166	-0.228
-6.0	0.236	0.172	0.093	0.000	-0.093	-0.172	-0.236
vertical energy loss vs. transverse beam offset [V/nC]							
offset	x [mm]						
y [mm]	-6.0	-4.0	-2.0	0.0	2.0	4.0	6.0
6.0	2.459	2.469	2.475	2.478	2.475	2.469	2.459
4.0	1.584	1.590	1.594	1.596	1.594	1.590	1.584
2.0	0.772	0.775	0.776	0.777	0.776	0.775	0.772
0.0	0.000	0.000	0.000	0.000	0.000	0.000	0.000
-2.0	-0.772	-0.775	-0.776	-0.777	-0.776	-0.775	-0.772
-4.0	-1.584	-1.590	-1.594	-1.596	-1.594	-1.590	-1.584
-6.0	-2.459	-2.469	-2.475	-2.478	-2.475	-2.469	-2.459
longitudinal energy loss vs. transverse beam offset [V/nC]							
offset	x [mm]						
y [mm]	-6.0	-4.0	-2.0	0.0	2.0	4.0	6.0
6.0	2.279	2.291	2.299	2.302	2.299	2.291	2.279
4.0	2.211	2.223	2.231	2.234	2.231	2.223	2.211
2.0	2.171	2.183	2.191	2.193	2.191	2.183	2.171
0.0	2.158	2.170	2.178	2.180	2.178	2.170	2.158
-2.0	2.171	2.183	2.191	2.193	2.191	2.183	2.171
-4.0	2.211	2.223	2.231	2.234	2.231	2.223	2.211
-6.0	2.279	2.291	2.299	2.302	2.299	2.291	2.279

Table 4.13: Rectangular shielded bellows without slots : longitudinal and transverse energy loss as function of the transverse beam offset for a Gaussian bunch of $\sigma = 20$ mm.

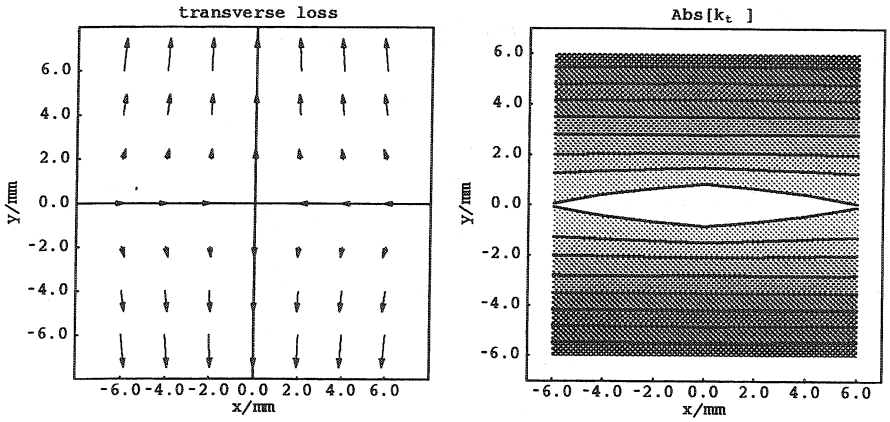

Figure 4.40: Rectangular shielded bellows Model 0: vector- & contour-plot of transverse energy loss vs. beam offset ($\sigma = 20$ mm).

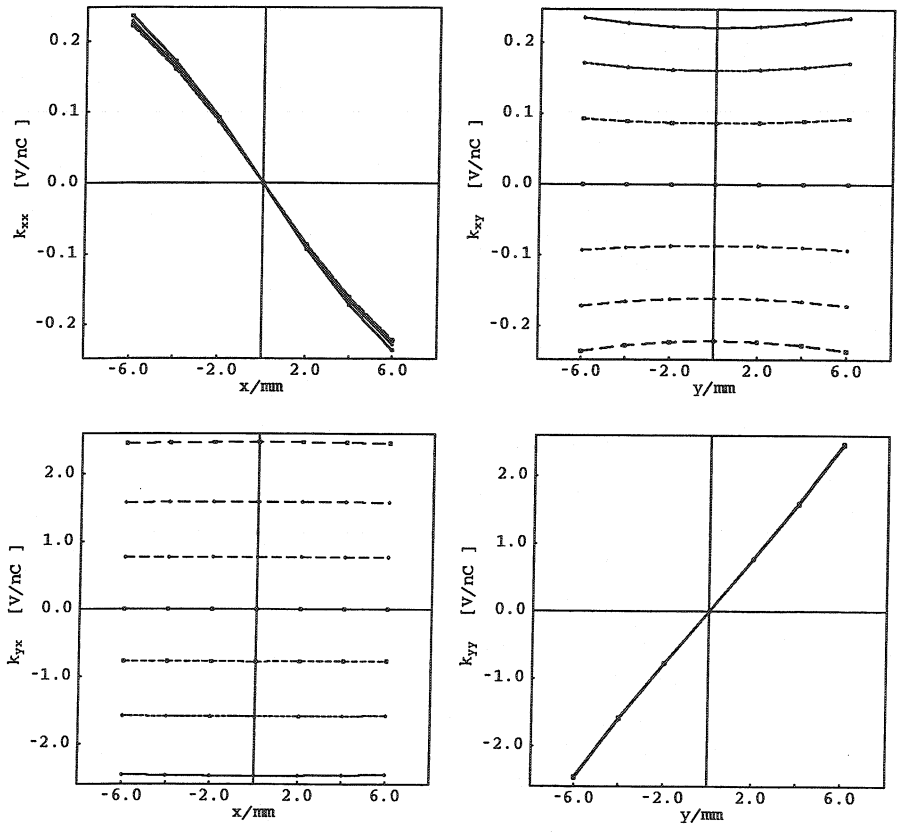

Figure 4.41: Rectangular shielded bellows Model 0: horizontal and vertical energy loss as function of the horizontal and vertical beam offset for a Gaussian beam (σ=20 mm).

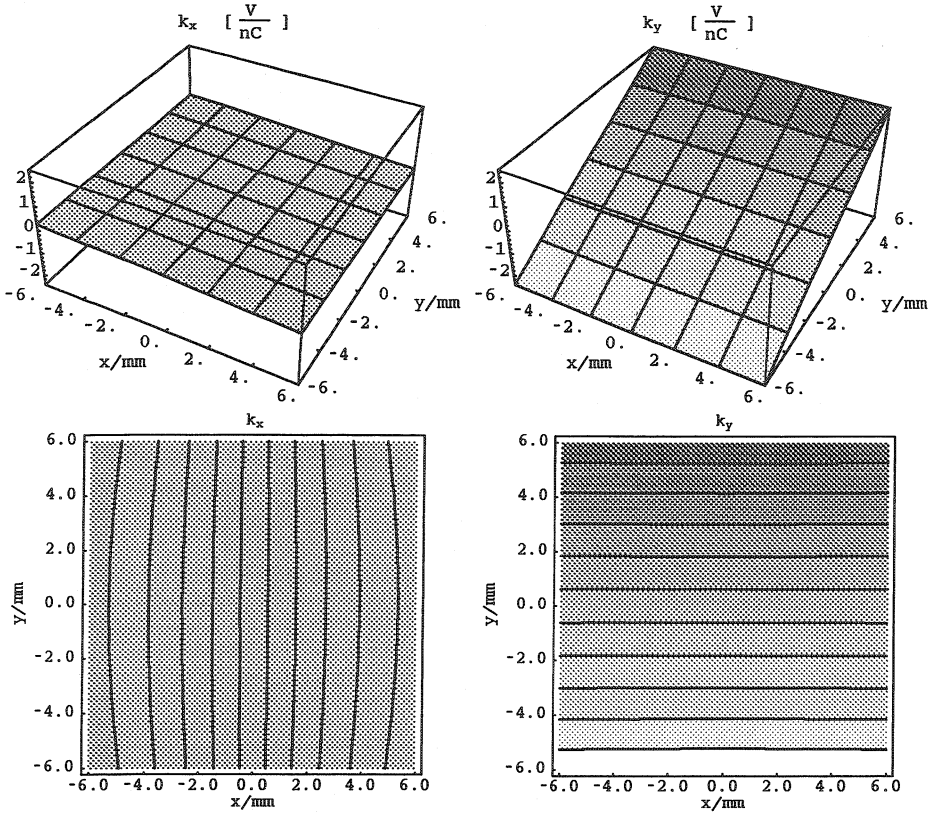

Figure 4.42: Rectangular shielded bellows: horizontal and vertical energy loss as function of the transverse beam position ($\sigma = 20$ mm).

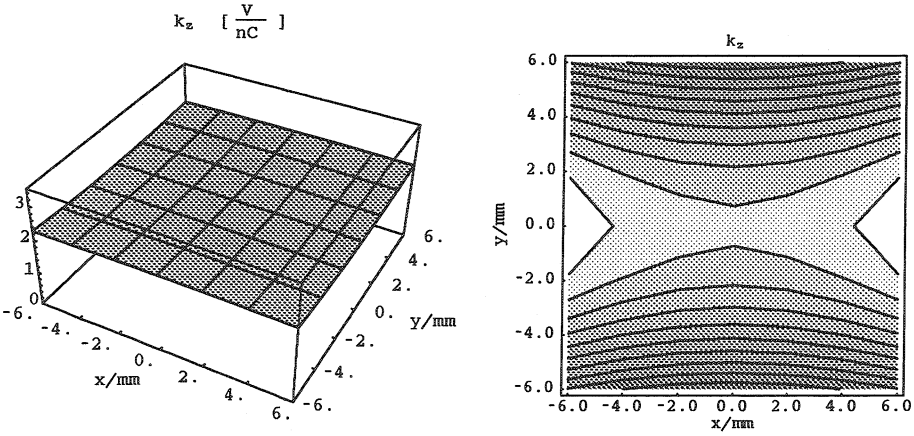

Figure 4.43: Rectangular shielded bellows Model 0: longitudinal energy loss as function of the transverse beam position ($\sigma = 20$ mm).

Comparison of the Rectangular bellows models

The longitudinal loss factors and the main components of the longitudinal energy loss for the rectangular bellows models with different slot configuration are shown in Figure 4.44.

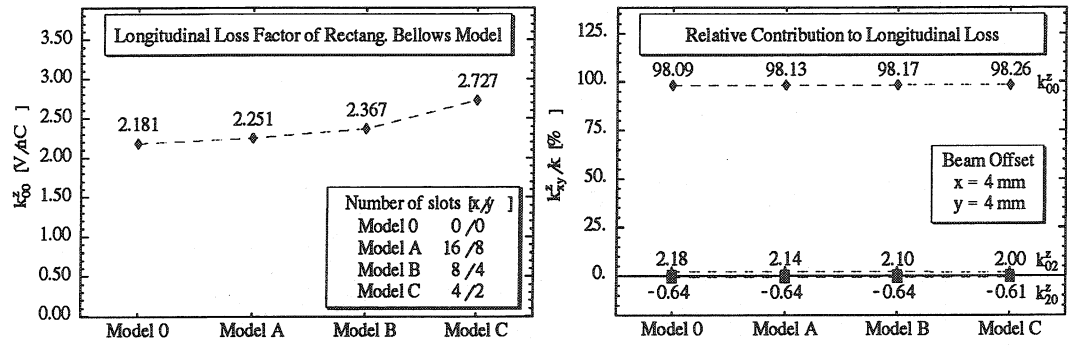

Figure 4.44: Longitudinal loss factor of the rectangular bellows models and relative contributions to the longitudinal energy loss for a $\sigma =$ 20 mm Gaussian bunch and a (x,y) beam-offset of $(4, 4)$ mm.

When the number of slots is increased and their width reduced, the values for the loss factors converge to the one of the model without slots, i.e. from Model C to Model 0. For a rather large beam offset of 4 mm in each transverse direction, the contribution of the higher order components comes mainly from $k^{(z)}_{0,2}$ and $k^{(z)}_{2,0}$, but they yield only a small contribution.

The same dependence on the slot configuration can be seen for the transverse loss factors in Figure 4.45 and 4.46. Especially the values of the loss factor components $k^{(x)}_{1,2}$ and $k^{(y)}_{2,1}$, which represent the main source of wake field coupling of the two transverse planes converge to the values for the model without slots i.e. Model 0. Therefore one can assume that the influence of the slots between the sliding fingers is quite weak and can be neglected for further calculations. The slots are only important if one is interested in very high frequencies.

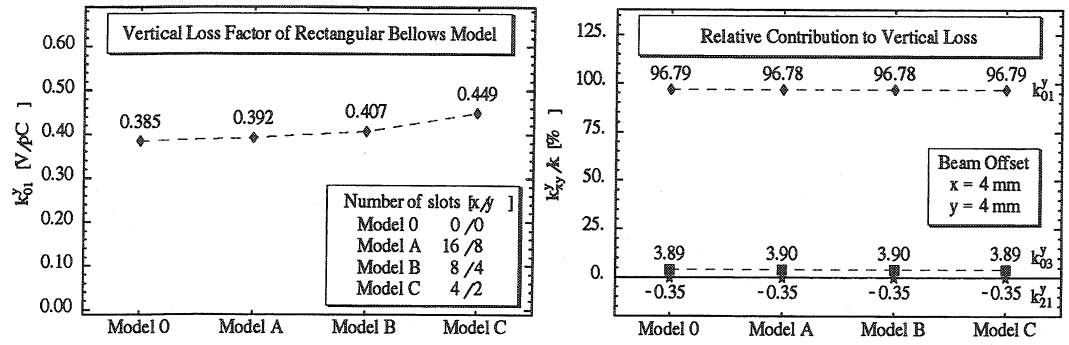

Figure 4.45: Vertical loss factors of the rectangular bellows models and relative contributions to the vertical loss factor for a $\sigma = 20$ mm Gaussian bunch and a (x,y) beam-offset of $(4, 4)$ mm.

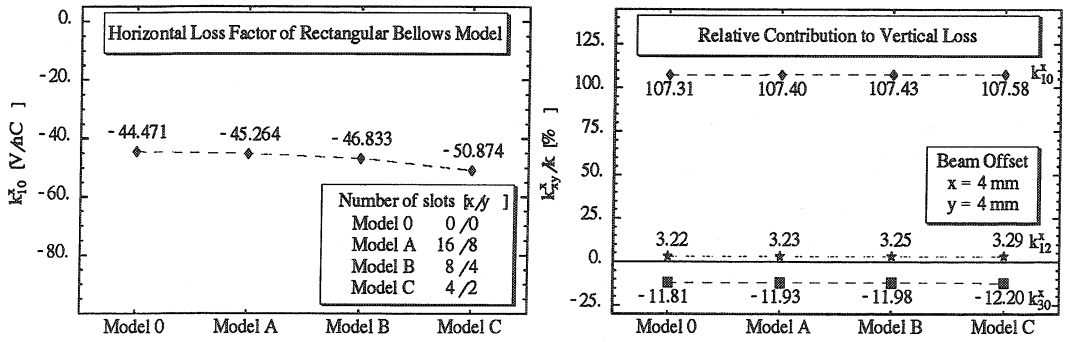

Figure 4.46: Horizontal loss factors of the rectangular bellows models and relative contributions to the horizontal loss factor for a $\sigma = 20$ mm Gaussian bunch and a (x,y) beam-offset of $(4, 4)$ mm.

4.4.2 Elliptic Model of LEP Shielded Bellows

In the last section the influence on the wake fields of the slots between the sliding contact fingers of the LEP shielded bellows was examined. Since the influence of these slots was found to be small, a more realistic elliptic model without slots will be used to calculate the wake potentials, which have later been used in the multi particle simulation program TRISIM3D (§5). Apart from the different cross section, the progression of the geometry in longitudinal direction is the same as for the rectangular model (see Fig. 4.37).

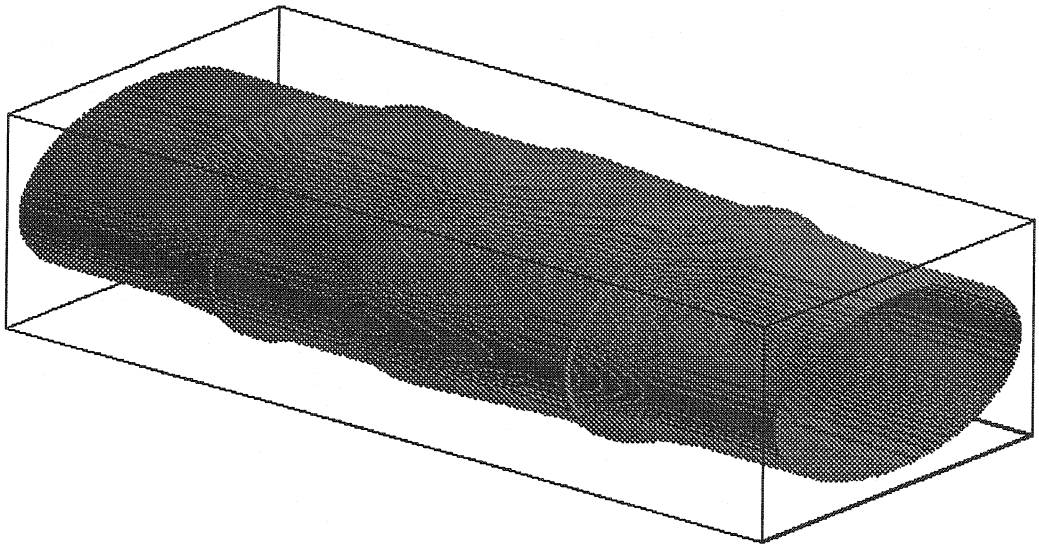

Figure 4.47: Elliptic model of LEP shielded bellows

Loss factors as function of the beam offset

The loss factors of a Gaussian beam of $\sigma = 5$ mm for horizontal resp. vertical beam offsets from 0 to +10 mm in steps of 2 mm were calculated for the elliptic model. The values of the longitudinal and transverse energy loss (Table 4.14) and their graphical representations are shown on the following pages (p. 72 - 74).

horizontal energy loss vs. transverse beam offset [V/nC]						
offset	x [mm]					
y [mm]	0.0	2.0	4.0	6.0	8.0	10.0
10.0	0.000	0.071	0.153	0.257	0.390	0.561
8.0	0.000	0.068	0.145	0.239	0.357	0.506
6.0	0.000	0.065	0.137	0.224	0.331	0.464
4.0	0.000	0.063	0.132	0.213	0.312	0.435
2.0	0.000	0.061	0.128	0.206	0.301	0.417
0.0	0.000	0.061	0.127	0.204	0.297	0.411
vertical energy loss vs. transverse beam offset [V/nC]						
offset	x [mm]					
y [mm]	0.0	2.0	4.0	6.0	8.0	10.0
10.0	17.267	17.268	17.273	17.287	17.315	17.365
8.0	13.216	13.217	13.223	13.235	13.258	13.297
6.0	9.586	9.588	9.592	9.602	9.620	9.648
4.0	6.243	6.244	6.248	6.254	6.266	6.285
2.0	3.079	3.079	3.081	3.085	3.091	3.100
0.0	0.000	0.000	0.000	0.000	0.000	0.000
longitudinal energy loss vs. transverse beam offset [V/nC]						
offset	x [mm]					
y [mm]	0.0	2.0	4.0	6.0	8.0	10.0
10.0	51.07	51.08	51.10	51.15	51.23	51.34
8.0	48.49	48.50	48.53	48.58	48.66	48.76
6.0	46.55	46.56	46.59	46.64	46.72	46.82
4.0	45.19	45.20	45.23	45.28	45.36	45.46
2.0	44.39	44.40	44.43	44.48	44.56	44.66
0.0	44.12	44.13	44.16	44.22	44.29	44.39

Table 4.14: Elliptic shielded bellows: longitudinal and transverse energy loss as function of the transverse beam-offset for a Gaussian bunch ($\sigma = 5$ mm).

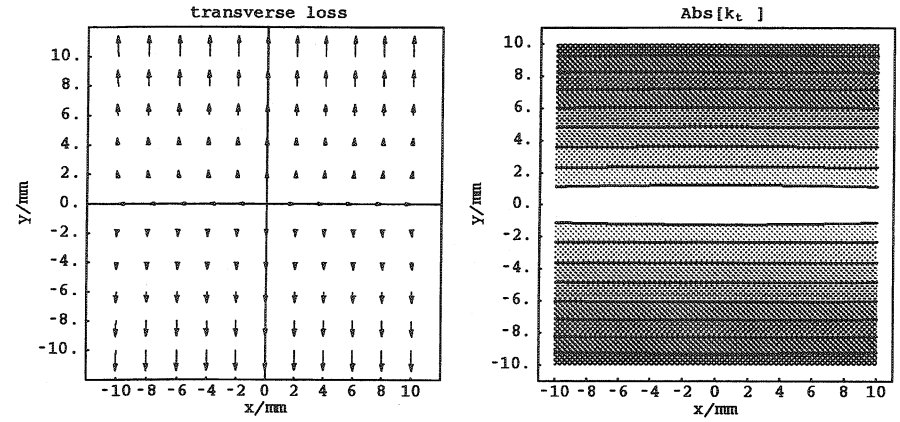

Figure 4.48: Elliptic shielded bellows: vector and contour-plot of the transverse energy loss as function of the beam offset ($\sigma = 5$ mm).

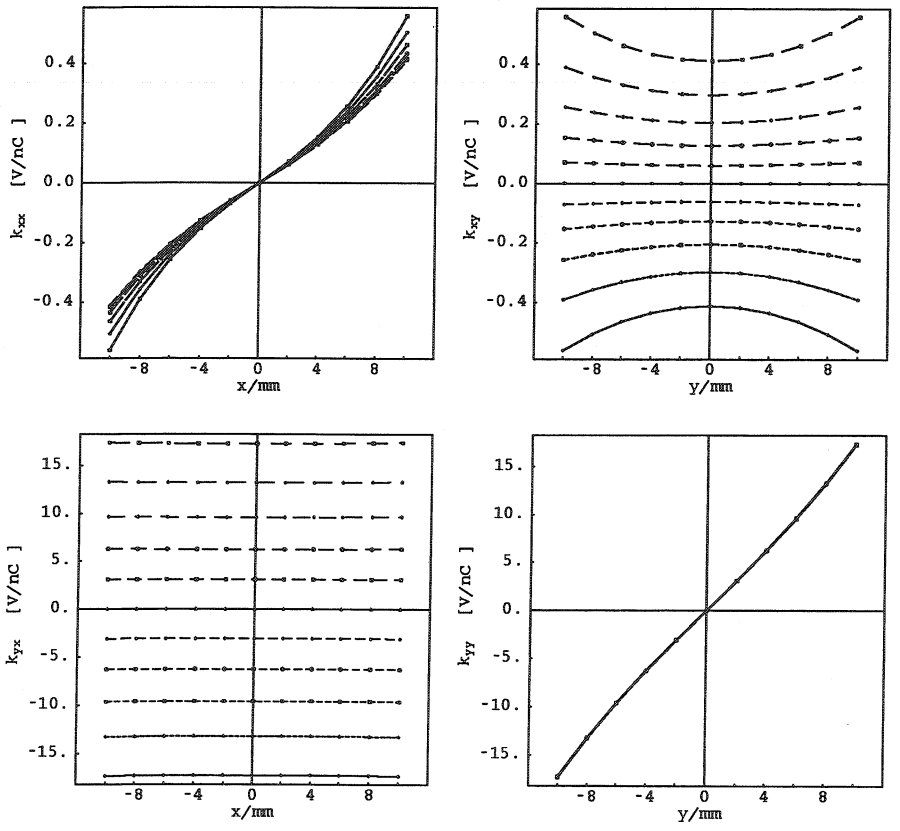

Figure 4.49: Elliptic shielded bellows: horizontal and vertical energy loss as function of the horiz. and vertical beam offset (σ=5 mm).

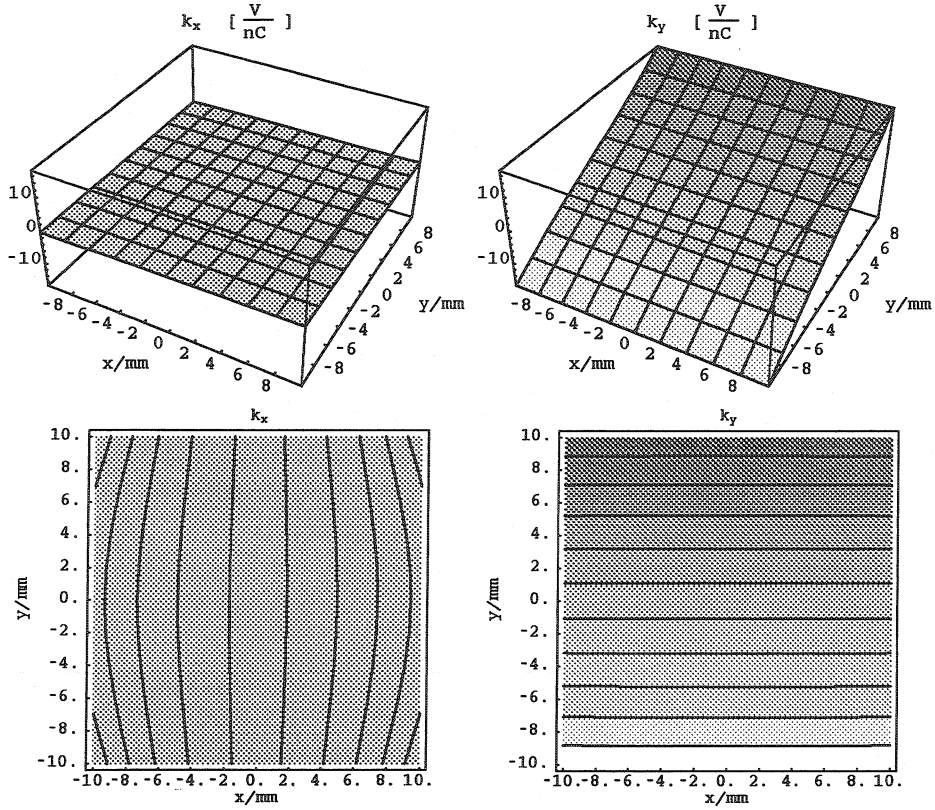

Figure 4.50: Elliptic shielded bellows: horizontal and vertical energy loss as function of the transverse beam position ($\sigma = 5$ mm).

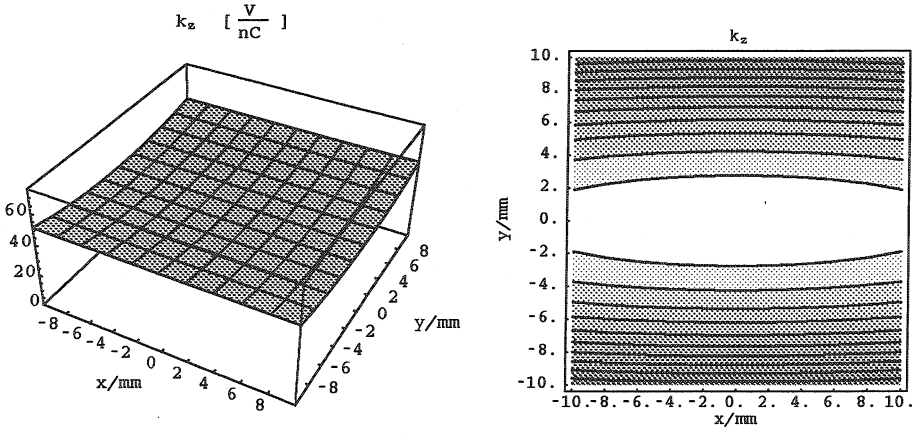

Figure 4.51: Elliptic shielded bellows: longitudinal energy loss as function of the transverse beam position ($\sigma = 5$ mm).

Main components of the loss factors

The main components of the loss factors for the elliptic bellows model are presented in Table 4.15. The values obtained for an axially symmetric model (2-D) are shown as well. They are much smaller than those of the 3-D one. The ratio of vertical to horizontal loss factors is very high. An explanation for these large ratios of the transverse loss factors in non-axially symmetric structures can be found in §5.3.2. The main components for a beam with and (x,y) offset of (4, 4) mm are displayed in the table as well. Even for this rather large beam offset the relative contribution of the largest higher order components is only a few percent. The horizontal-vertical cross coupling term $k^{(x)}_{xy^2}$ is also a few percent, while the vertical-horizontal one $k^{(y)}_{yx^2}$ almost vanishes.

	main loss factor components								
	horizontal			vertical			longitudinal		
geom.	$k^{(x)}_x$	$k^{(x)}_{x^3}$	$k^{(x)}_{xy^2}$	$k^{(y)}_y$	$k^{(y)}_{y^3}$	$k^{(y)}_{yx^2}$	$k_{\parallel}$	$k_{\parallel x^2}$	$k_{\parallel y^2}$
	V/pCm	V/pCm^3	V/pCm^3	V/pCm	V/pCm^3	V/pCm^3	V/pC	V/pCm^2	V/pCm^2
(3-D)	0.0298	117.5	63.17	1.53	1748.2	64.4	0.044	2.54	66.25
(2-D)	—	—	—	0.708	—	—	0.336	—	38.86
	relative contribution for a (x,y) beam offset of (4,4) mm								
(3-D)[%]	90.65	5.71	3.07	98.11	1.79	0.07	97.55	0.09	2.34

Table 4.15: Main components of the energy loss for an elliptic model of the LEP shielded bellows for a $\sigma = 5$ mm Gaussian beam and their relative contribution for a (x,y) beam-offset of (4,4) mm.

4.5 LEP Electrostatic Separators

Other structures expected to contribute strongly to the transverse coupling impedance of LEP are the electrostatic separators. Again a quarter of the structure was used for the wake potential calculations to allow a better transverse description of the geometry. The length of the separator plates was reduced from 4 meters to 30 cm. The dependence of the loss factor on the length of the plates was found to be small, as long as the plates are longer than the range of the wake potential calculation [Sab95a], because the electromagnetic field travelling along with the beam does not change significantly while the beam is between the two plates. The full geometry is shown in Figures 4.52 and 4.53, for the wake field calculations a quarter of the structure was used .

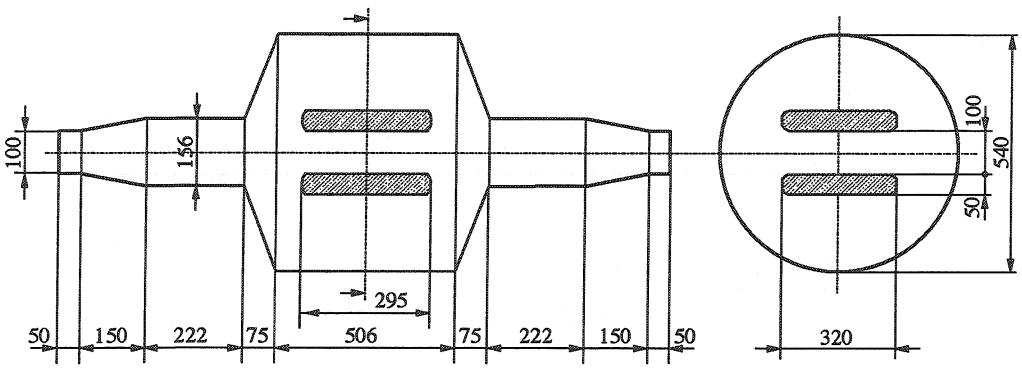

Figure 4.52: Geometry of the LEP separator model with tapers and plates.

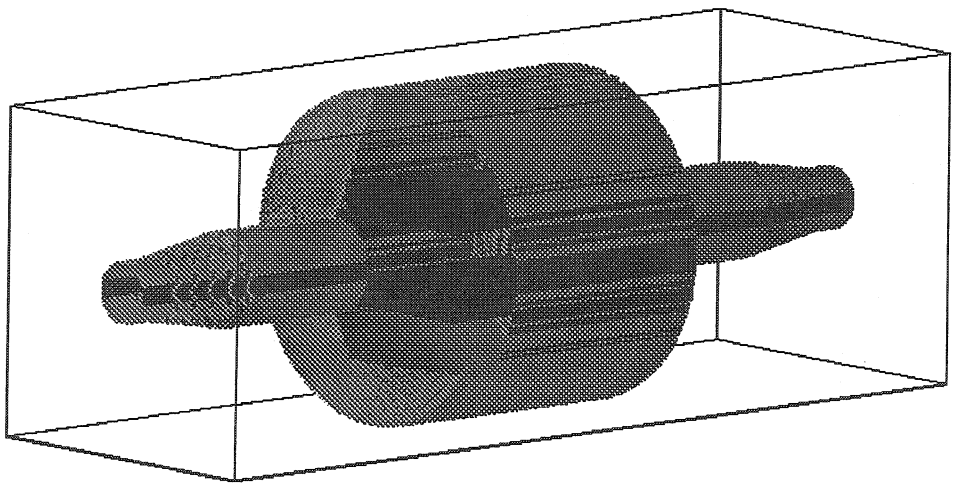

Figure 4.53: LEP separator model with tapers and plates.

4.5.1 LEP-Separators without Plates

The longitudinal and transverse energy loss of a Gaussian beam with $\sigma = 25$ mm for beam-offsets Δx, Δy of $\pm 0, 2.5, 5, 7.5$ mm are listed in Table 4.16, and their graphical representations are shown on pages 78 and 79.

horizontal energy loss vs. transverse beam offset [V/nC]							
offset	x [mm]						
y [mm]	-7.5	-5.0	-2.5	0.0	2.5	5.0	7.5
7.5	-26.46	-16.44	-7.45	0.00	7.45	16.44	26.46
5.0	-24.20	-14.95	-6.80	0.00	6.80	14.95	24.20
2.5	-22.80	-14.13	-6.46	0.00	6.46	14.13	22.80
0.0	-22.44	-13.92	-6.38	0.00	6.38	13.92	22.44
-2.5	-22.80	-14.13	-6.46	0.00	6.46	14.13	22.80
-5.0	-24.20	-14.95	-6.80	0.00	6.80	14.95	24.20
-7.5	-26.46	-16.44	-7.45	0.00	7.45	16.44	26.46
vertical energy loss vs. transverse beam offset [V/nC]							
offset	x [mm]						
y [mm]	-7.5	-5.0	-2.5	0.0	2.5	5.0	7.5
7.5	25.84	23.55	22.15	21.78	22.15	23.55	25.84
5.0	16.09	14.57	13.73	13.52	13.73	14.57	16.09
2.5	7.29	6.62	6.27	6.19	6.27	6.62	7.29
0.0	0.00	0.00	0.00	0.00	0.00	0.00	0.00
-2.5	-7.29	-6.62	-6.27	-6.19	-6.27	-6.62	-7.29
-5.0	-16.09	-14.57	-13.73	-13.52	-13.73	-14.57	-16.09
-7.5	-25.84	-23.55	-22.15	-21.78	-22.15	-23.55	-25.84
longitudinal energy loss vs. transverse beam offset [V/pC]							
offset	x [mm]						
y [mm]	-7.5	-5.0	-2.5	0.0	2.5	5.0	7.5
7.5	-0.311	-0.310	-0.309	-0.309	-0.309	-0.310	-0.311
5.0	-0.310	-0.309	-0.308	-0.308	-0.308	-0.309	-0.310
2.5	-0.309	-0.308	-0.307	-0.307	-0.307	-0.308	-0.309
0.0	-0.309	-0.308	-0.307	-0.307	-0.307	-0.308	-0.309
-2.5	-0.309	-0.308	-0.307	-0.307	-0.307	-0.308	-0.309
-5.0	-0.310	-0.309	-0.308	-0.308	-0.308	-0.309	-0.310
-7.5	-0.311	-0.310	-0.309	-0.309	-0.309	-0.310	-0.311

Table 4.16: LEP separator without plates: Longitudinal and transverse energy loss vs. transverse beam offset for a Gaussian bunch with $\sigma = 25$ mm.

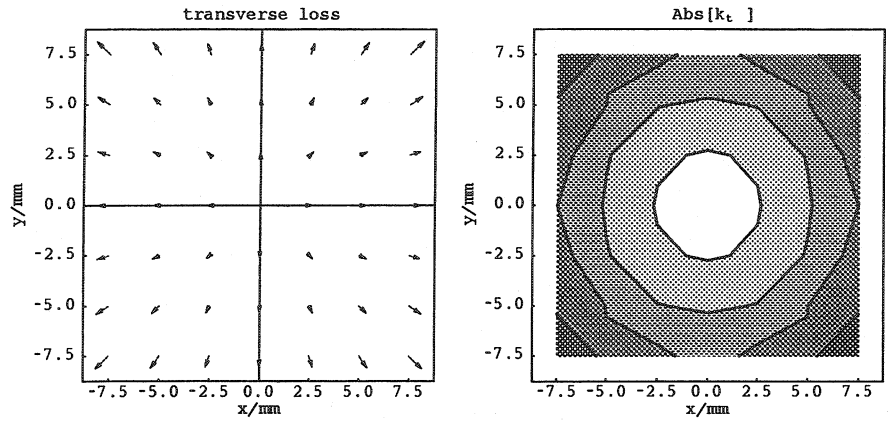

Figure 4.54: LEP separator without plates: vector and contour-plot of the transverse energy loss as function of the beam offset (σ = 25 mm).

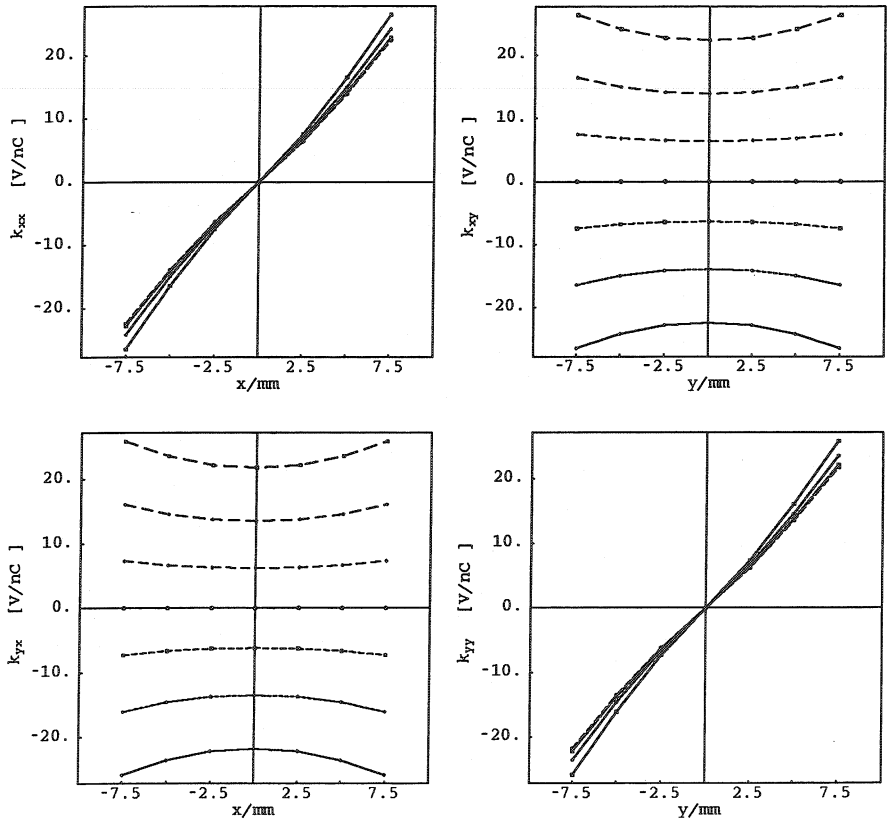

Figure 4.55: LEP separator without plates: horizontal and vertical energy loss as function of the horiz. and vertical beam offset (σ = 25 mm).

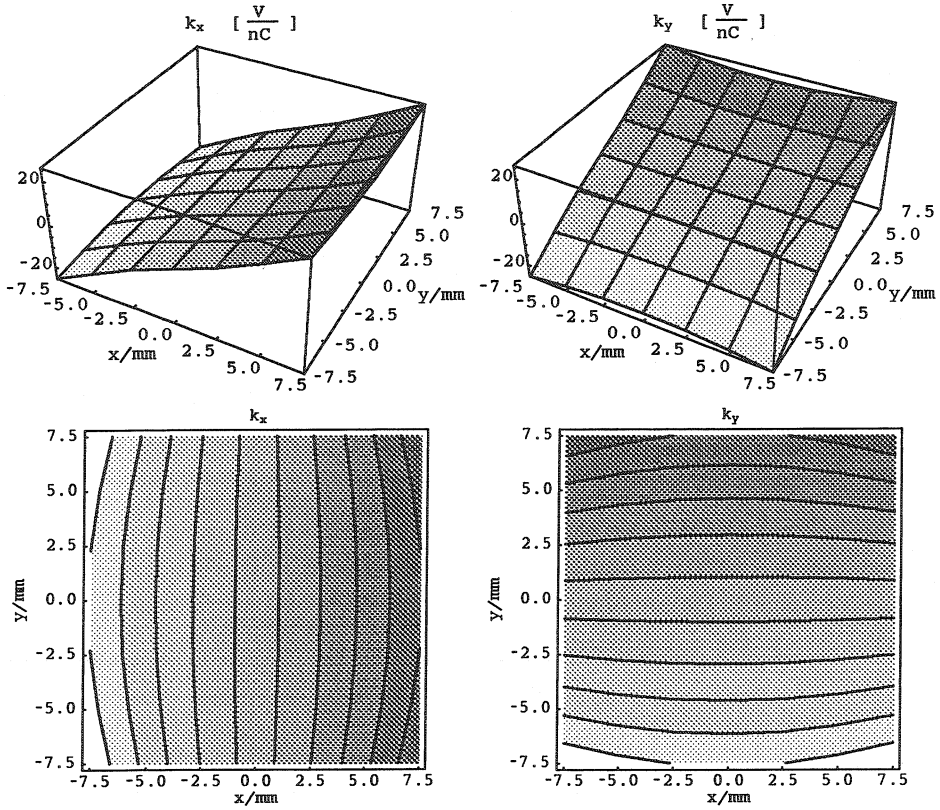

Figure 4.56: LEP separator without plates: horizontal and vertical energy loss as function of the transverse beam position ($\sigma = 25$ mm).

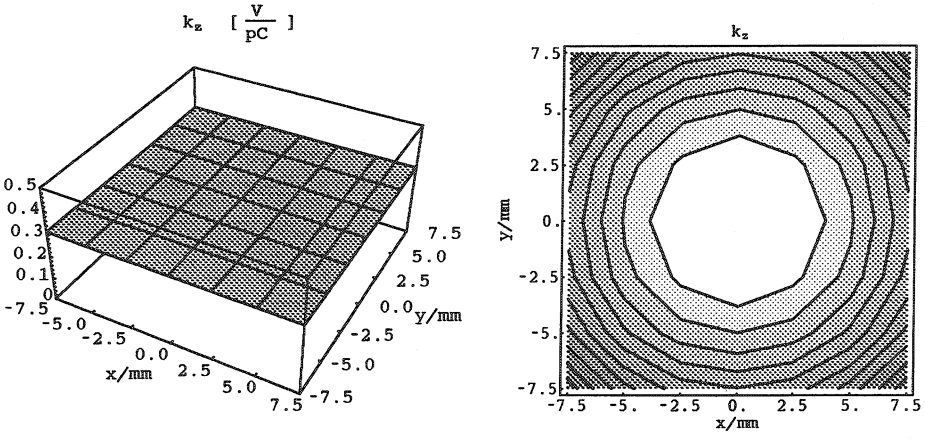

Figure 4.57: LEP separator without plates: longitudinal energy loss as function of the transverse beam position ($\sigma = 25$ mm).

4.5.2 LEP-Separators with Plates

The longitudinal and transverse energy loss of a Gaussian beam with $\sigma = 25$ mm for beam-offsets Δx, Δy of $\pm 0, 2.5, 5, 7.5$ mm are listed in Table 4.17, and their graphical representations are shown on pages 81 and 82.

horizontal energy loss vs. transverse beam offset [V/nC]							
offset	x [mm]						
y [mm]	-7.5	-5.0	-2.5	0.0	2.5	5.0	7.5
7.5	-23.05	-13.90	-6.02	0.00	6.02	13.90	23.05
5.0	-20.04	-11.94	-5.17	0.00	5.17	11.94	20.04
2.5	-18.17	-10.86	-4.72	0.00	4.72	10.86	18.17
0.0	-17.71	-10.60	-4.62	0.00	4.62	10.60	17.71
-2.5	-18.17	-10.86	-4.72	0.00	4.72	10.86	18.17
-5.0	-20.04	-11.94	-5.17	0.00	5.17	11.94	20.04
-7.5	-23.05	-13.90	-6.02	0.00	6.02	13.90	23.05
vertical energy loss vs. transverse beam offset [V/nC]							
offset	x [mm]						
y [mm]	-7.5	-5.0	-2.5	0.0	2.5	5.0	7.5
7.5	47.39	44.59	42.88	42.44	42.88	44.59	47.39
5.0	29.75	27.88	26.86	26.60	26.86	27.88	29.75
2.5	13.70	12.90	12.48	12.38	12.48	12.90	13.70
0.0	0.00	0.00	0.00	0.00	0.00	0.00	0.00
-2.5	-13.70	-12.90	-12.48	-12.38	-12.48	-12.90	-13.70
-5.0	-29.75	-27.88	-26.86	-26.60	-26.86	-27.88	-29.75
-7.5	-47.39	-44.59	-42.88	-42.44	-42.88	-44.59	-47.39
longitudinal energy loss vs. transverse beam offset [V/pC]							
offset	x [mm]						
y [mm]	-7.5	-5.0	-2.5	0.0	2.5	5.0	7.5
7.5	-0.295	-0.294	-0.294	-0.294	-0.294	-0.294	-0.295
5.0	-0.292	-0.291	-0.291	-0.290	-0.291	-0.291	-0.292
2.5	-0.290	-0.289	-0.289	-0.289	-0.289	-0.289	-0.290
0.0	-0.289	-0.289	-0.288	-0.289	-0.288	-0.289	-0.289
-2.5	-0.290	-0.289	-0.289	-0.289	-0.289	-0.289	-0.290
-5.0	-0.292	-0.291	-0.291	-0.290	-0.291	-0.291	-0.292
-7.5	-0.295	-0.294	-0.294	-0.294	-0.294	-0.294	-0.295

Table 4.17: LEP separator with plates: longitudinal and transverse energy loss vs. transverse beam offset for a Gaussian bunch with $\sigma = 25$ mm.

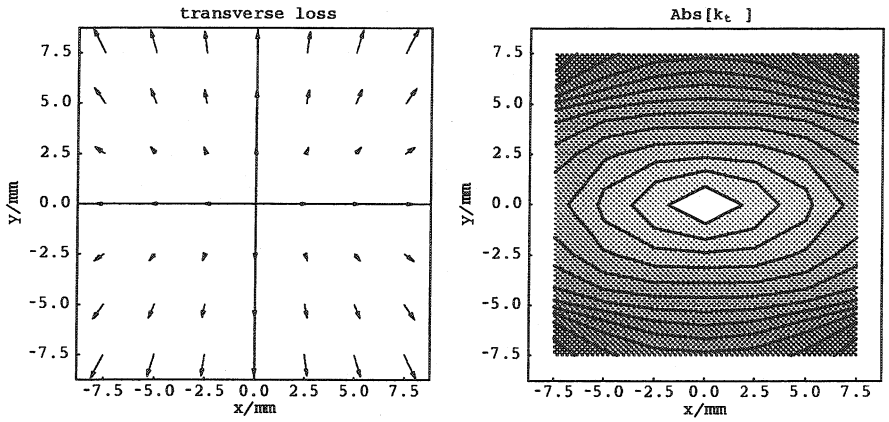

Figure 4.58: LEP separator with plates: vector and contour-plot of the transverse energy loss as function of the beam offset for a Gaussian bunch with $\sigma = 25$ mm.

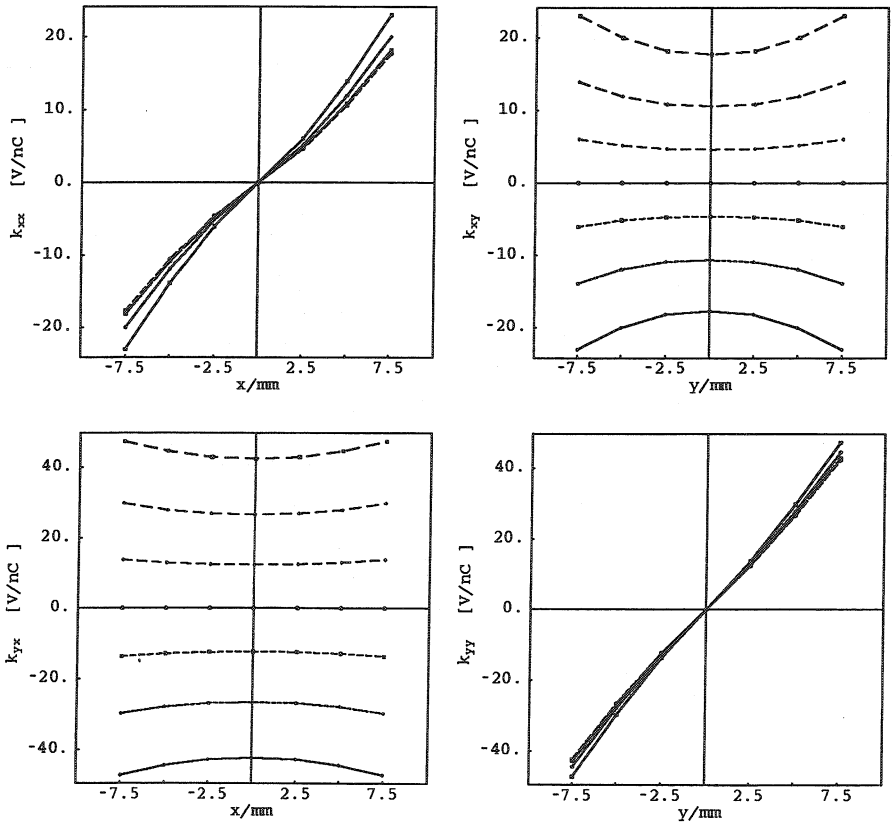

Figure 4.59: LEP separator with plates: horizontal and vertical energy loss as function of the horiz. and vertical beam offset ($\sigma = 25$ mm).

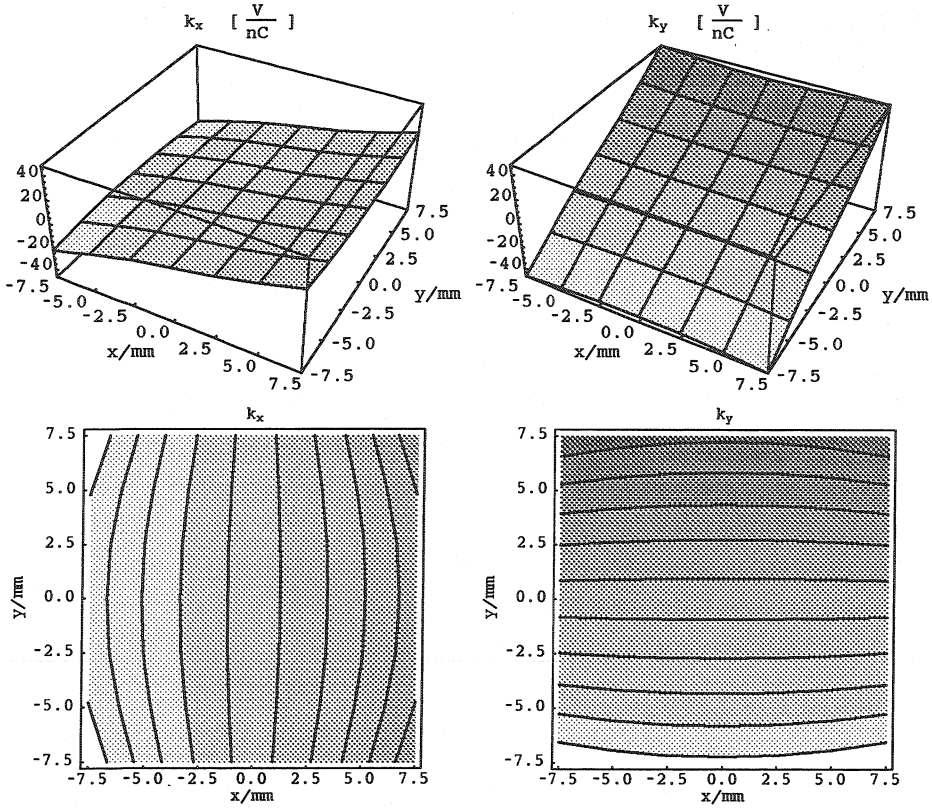

Figure 4.60: LEP separator with plates: horizontal and vertical energy loss as function of the transverse beam position ($\sigma = 25$ mm).

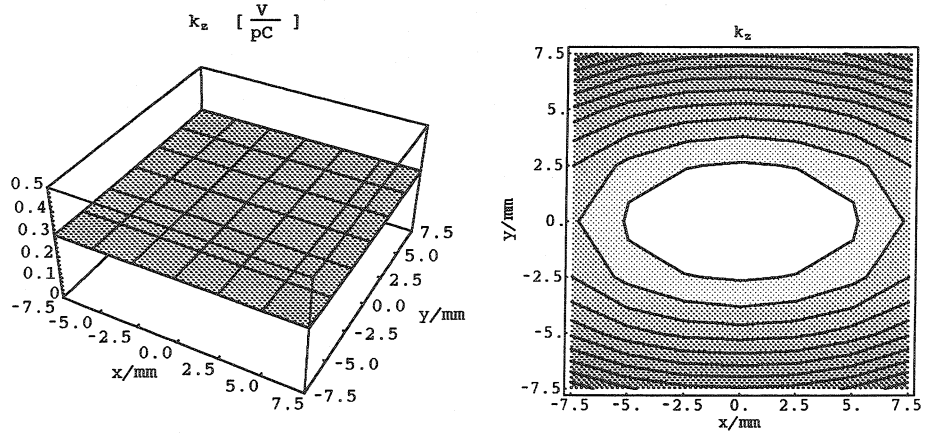

Figure 4.61: LEP separator with plates: longitudinal energy loss as function of the transverse beam position ($\sigma = 25$ mm).

4.5.3 Comparison of Separator Model with and without Plates

The main components of the separator models with and without plates are listed in Table 4.18. For a beam with (5, 5) mm beam offset the third order components k_{x^3} and k_{y^3} yield a quite strong contribution of more than 10 %. Since the values of this components are already high for the model without plates, they are not related to the presence of the separator plates. Due the Cartesian mesh, the large tapers of the separator tanks are not very smooth and result in these higher order field components. On the other hand, the transverse coupling terms k_{yx^2} and k_{yx^2} are small. The presence of the separator plates does not cause a significant increase of the horizontal-vertical wake field coupling in this structure.

	main loss factor components								
	horizontal			vertical			longitudinal		
separator	k_x	k_{x^3}	k_{xy^2}	k_y	k_{y^3}	k_{yx^2}	$k_{\parallel}$	$k_{\parallel x^2}$	$k_{\parallel y^2}$
model	V/pCm	V/pCm^3	V/pCm^3	V/pCm	V/pCm^3	V/pCm^3	V/pC	V/pCm^2	V/pCm^2
no plates	2.454	16114.2	4166.75	2.379	15955.2	4405.05	0.307	15.24	-13.56
plates	1.735	18867.2	4917.51	4.801	25238.8	5013.76	0.289	104.14	-34.19
	relative contribution in % for a (x,y) beam offset of 5, 5 mm								
no plates	82.07	13.47	3.48	81.62	13.69	3.78	99.47	-0.12	-0.11
plates	72.67	19.76	5.15	86.09	11.31	2.25	99.17	-0.89	-0.29

Table 4.18: Lower order components of the energy loss of the LEP separators, with and without plates, for a $\sigma = 25$ mm Gaussian beam and relative contribution for a (x,y) beam-offset of (5,5) mm.

Chapter 5

TRISIM3D

5.1 Equations of motion

The particle distribution in the simulation program is represented by a number of *super-particles*, also called *macro-particles*, typically a few thousand. Each of these *super-particles* represents a large number of real particles in the accelerator, e.g for LEP one super-particle represents of the order of 10^8 electrons or positrons in the real machine.

The accelerator is represented by a ring divided into a number of sections. Each section consists of a point-like machine element followed by an arc section. In the drift sections the motion of the macro-particles is assumed to be linear. The effects of synchrotron radiation damping and quantum excitation are also considered in these sections.

The equations used in TRISIM3D to describe the motion of these super-particles follow the same formalism as used in TRISIM[Sab95a], which were derived basically from its predecessors HERSIM2 [Wan90], HERSIM [Nys87] and SIMTRAC [Bra84], and also include some modifications suggested in [Zot93]. The longitudinal motion is described by the energy deviation ε and time delay t with respect to a synchronous reference particle. For the transverse motion the horizontal and vertical positions x, y and slopes x', y' are used. These transverse coordinates of a particle are represented by the 4-dimensional vector

$$\mathbf{z} = \begin{pmatrix} x \\ x' \\ y \\ y' \end{pmatrix}. \tag{5.1}$$

The transfer matrix therefore becomes a 4 × 4 - matrix M. The different elements of the accelerator are taken into account by point-like interactions, i.e. a kick is applied to the particle while the position remains the same. This approximation is valid if the betatron phase does not change much while the particle traverses the structure and the optical functions are also approximately constant over the length of the element.

The effect of such a point like element on the macro-particles can be written as[1]

$$\begin{aligned} \mathbf{z}_\mathbf{i}^* &= \mathbf{z}_\mathbf{i} + \delta\mathbf{z}_\mathbf{i} \\ \varepsilon_i^* &= \varepsilon_i + \delta\varepsilon_i \\ t_i^* &= t_i \end{aligned} \tag{5.2}$$

where $\delta\varepsilon_i$ is the longitudinal energy change and where

$$\delta\mathbf{z}_\mathbf{i} = \begin{pmatrix} 0 \\ \delta x' \\ 0 \\ \delta y' \end{pmatrix} \tag{5.3}$$

corresponds to the horizontal and vertical kicks caused by these elements. For the drift sections between the elements, a linear transfer matrix M is assumed

$$\mathbf{M} = \begin{pmatrix} \mathcal{M}_{11} & \mathcal{M}_{12} & 0 & 0 \\ \mathcal{M}_{21} & \mathcal{M}_{22} & 0 & 0 \\ 0 & 0 & \mathcal{M}_{33} & \mathcal{M}_{34} \\ 0 & 0 & \mathcal{M}_{43} & \mathcal{M}_{44} \end{pmatrix}, \tag{5.4}$$

with the non-zero components:

$$\mathcal{M}_{11}(\varepsilon_i^*) = \exp\left(-\frac{T_i}{\tau_x}\right)\sqrt{\frac{\beta_{x,i+1}}{\beta_{x,i}}}\cos(\Psi_i(\varepsilon_i^*)) \tag{5.5}$$

[1]The symbols $\mathbf{z}_\mathbf{i}^*$, ε_i^* and t_i^* indicate the coordinates after the interaction with the i-th element, before traversing the i-th arc-section of the ring.

$$\mathcal{M}_{12}(\varepsilon_i^*) = \sqrt{\beta_{x,i+1}\beta_{x,i}}\sin(\Psi_i(\varepsilon_i^*)) \tag{5.6}$$

$$\mathcal{M}_{21}(\varepsilon_i^*) = \exp\left(-\frac{T_i}{\tau_x}\right)\frac{1}{\sqrt{\beta_{x,i+1}\beta_{x,i}}}\sin(\Psi_i(\varepsilon_i^*)) \tag{5.7}$$

$$\mathcal{M}_{22}(\varepsilon_i^*) = \sqrt{\frac{\beta_{x,i}}{\beta_{x,i+1}}}\cos(\Psi_i(\varepsilon_i^*)) \tag{5.8}$$

$$\mathcal{M}_{33}(\varepsilon_i^*) = \exp\left(-\frac{T_i}{\tau_y}\right)\sqrt{\frac{\beta_{y,i+1}}{\beta_{y,i}}}\cos(\Psi_i(\varepsilon_i^*)) \tag{5.9}$$

$$\mathcal{M}_{34}(\varepsilon_i^*) = \sqrt{\beta_{y,i+1}\beta_{y,i}}\sin(\Psi_i(\varepsilon_i^*)) \tag{5.10}$$

$$\mathcal{M}_{43}(\varepsilon_i^*) = \exp\left(-\frac{T_i}{\tau_y}\right)\frac{1}{\sqrt{\beta_{y,i+1}\beta_{y,i}}}\sin(\Psi_i(\varepsilon_i^*)) \tag{5.11}$$

$$\mathcal{M}_{44}(\varepsilon_i^*) = \sqrt{\frac{\beta_{y,i}}{\beta_{y,i+1}}}\cos(\Psi_i(\varepsilon_i^*))\,. \tag{5.12}$$

Here the following definitions have been used:

$$u_i = (E_r + \varepsilon_i^*)\frac{Q_i}{1+Q_i} \tag{5.13}$$

$$Q_i = U_i\frac{E_r + \varepsilon_i^*}{E_r^2} \tag{5.14}$$

$$\Psi_i(\varepsilon_i^*) = \Phi_i^o\left[1 + \left(\frac{\xi_i - \eta}{E_r}\right)\left(\varepsilon_i^* - \frac{1}{2}u_i\right)\right] \tag{5.15}$$

The symbols used in the previous equations are summarised in the following list:

T_0	...	Revolution time of the reference particle,
T_i	...	Transit time of the reference particle through sector i,
E_r	...	Nominal energy of the particles,
σ_ε^o	...	Natural RMS energy spread,
τ_ε	...	Energy damping time,
τ_x, τ_y	...	Horizontal resp. vertical damping time,
U_i	...	Synchrotron radiation energy loss in the i-th sector,

ξ_i ... Chromaticity in the i-th sector, $\xi = (\delta Q/Q)/(\delta p/p) = Q'/Q$
α ... Momentum compaction factor: $\alpha = (\delta C/C)/(\delta p/p)$ (accelerator circumference C),
η ... Momentum slip factor $\eta = \alpha - 1/\gamma^2$,
Φ_i^o ... Betatron phase advance of the reference particle in sector i
$\beta_{x,i}, \beta_{y,i}$ ... horizontal and vertical β-function
$\bar{\beta}_x, \bar{\beta}_y$ ... average horizontal and vertical β-function at the i-th element, $\bar{\beta} = R/Q$.

The equations of motion for the drift sections between the elements can now be written as

$$\mathbf{z}_{i+1} = \mathbf{M}(\varepsilon_i^*) \cdot \mathbf{z}_i^* + \mathbf{R}_i \tag{5.16}$$

$$\varepsilon_{i+1} = \varepsilon_i^* - u_i + 2\sigma_\varepsilon^o \sqrt{\frac{T_0}{\tau_\varepsilon}} R_i^{(5)} \tag{5.17}$$

$$t_{i+1} = t_i^* + \alpha T_i \left[\frac{\varepsilon_i^* + E_r}{E_r} \frac{\ln(1+Q_i)}{Q_i} - 1 \right] \tag{5.18}$$

where

$$\mathbf{R}_i = \begin{pmatrix} \sqrt{\frac{2\epsilon_x \bar{\beta}_x T_0}{\tau_x}} R_i^{(1)} \\ \sqrt{\frac{2\epsilon_x}{\bar{\beta}_x T_0 \tau_x}} R_i^{(2)} \\ \sqrt{\frac{2\epsilon_y \bar{\beta}_y T_0}{\tau_y}} R_i^{(3)} \\ \sqrt{\frac{2\epsilon_y}{\bar{\beta}_y T_0 \tau_y}} R_i^{(4)} \end{pmatrix} \tag{5.19}$$

takes into account the quantum excitation due to synchrotron radiation ($R_i^{(1)}$ - $R_i^{(5)}$ are random numbers used to simulate this quantum effect).

The vertical and horizontal beam emittance ϵ_y, ϵ_y can be determined by the input parameters beam emittance $\mathcal{E}$ and coupling factor κ:

$$\mathcal{E}_x = \frac{\mathcal{E}}{1+\kappa} \tag{5.20}$$

$$\mathcal{E}_y = \frac{\kappa\mathcal{E}}{1+\kappa}. \tag{5.21}$$

If κ is set to zero, the vertical emittance vanishes, unless there are some elements that introduce horizontal-vertical coupling, e.g. skew quadrupoles, solenoids or 3-D impedances causing wake field coupling.

5.2 Machine elements

RF cavity

While traversing the accelerator, the particles lose energy due to synchrotron radiation and wake fields induced in the cavities and various other vacuum components. This energy must be replaced by the RF voltage. Using the following symbols

V_i^{RF} ... amplitude of the RF voltage,
ω_i^{RF} ... angular frequency of the RF wave,
Φ_i^s ... phase angle of the synchronous particle w.r.t. the RF wave,
$\delta\mathbf{z_i}$,$\delta\mathbf{z_i}$ ... longitudinal and transverse kicks due to the wake field,

the interaction of the macro-particles with a cavity can be written as

$$\mathbf{z}_i^* = \mathbf{z_i} + \delta\mathbf{z_i} \tag{5.22}$$

$$\varepsilon_i^* = \varepsilon_i + \delta\varepsilon_i + eV_i^{RF}\sin(\Phi_i^s + \omega_i^{RF}t_i). \tag{5.23}$$

Impedance

At any cross-section variation of the vacuum chamber, e.g. bellows, separators etc., the beam induces wake fields which result in kicks on trailing particles.

The effect of the impedances is like that of RF cavities with RF voltage $V_i^{RF} = 0$, i.e.

$$\mathbf{z}_i^* = \mathbf{z}_\mathbf{i} + \delta\mathbf{z}_\mathbf{i} \tag{5.24}$$
$$E_i = \varepsilon_i + \delta\varepsilon_i. \tag{5.25}$$

where $\delta\mathbf{z}_\mathbf{i}$ and $\delta\varepsilon_i$ are the longitudinal and transverse kicks due to the wake field.

Skew quadrupole

A source of horizontal vertical coupling may be skew quadrupolar fields due to localised magnets, or due to misalignments of normal quadrupoles. Skew quadrupoles can be approximately described using a thin-lens approximation [RS94], where it is assumed that the focal length of them is much larger than their physical length. The transfer matrix for these elements is

$$\mathrm{M} = \begin{pmatrix} 1 & 0 & 0 & 0 \\ 0 & 1 & k & 0 \\ 0 & 0 & 1 & 0 \\ k & 0 & 0 & 1 \end{pmatrix}, \tag{5.26}$$

where the quadrupole strength k has dimensions m^{-1}. It is given by

$$k = \frac{e\,l\,g}{p}, \tag{5.27}$$

when l is the length of the magnet, g the field gradient, and p the average momentum of the particles.

Kicker

Another type of machine elements are the kickers, e.g. used for the simulation of feedback systems.

$$\mathbf{z}_i^* = \mathbf{z}_\mathbf{i} + \delta\mathbf{z}_\mathbf{i} \tag{5.28}$$
$$\varepsilon_i^* = \varepsilon_i \tag{5.29}$$

where

$$\delta \mathbf{z_i} = \begin{pmatrix} 0 \\ \delta x_i' \\ 0 \\ \delta y_i' \end{pmatrix}, \tag{5.30}$$

$\delta x_i'$, $\delta y_i'$ are the horizontal and vertical deflection angle. It is assumed that there is no dependence of the deflection angle on the position or energy deviation of the particle.

5.3 Wake field representation in TRISIM3D

5.3.1 Axially-symmetric structures

The total wake field in an axially symmetric structure can be expressed as a sum over the wake fields of the multipole components of the exciting charge distribution. The fields due to the m-th multipole component have themselves the same azimuthal dependence. Furthermore, the wake force on a trailing particle scales like $(a/b)^{2m}$ in the longitudinal case, and as $(a/b)^{2m-1}$ in the transverse one, where b is the beam-pipe radius and a the transverse beam size, if the force comes from a cavity structure of a size comparable to the pipe radius ([Cha93] §2.1). Since in general the beam pipe radius is much larger than the transverse beam size ($b \gg a$) the longitudinal effects are dominated by the $m = 0$ mode, and the transverse effects by the dipole mode $m = 1$.

Normally the wake force $\mathbf{F}$ is a complicated function of time and spatial position. For high energy particles the trajectory is not much perturbed while traversing a structure. It is therefore useful to introduce the integral over the force along a straight trajectory

$$\mathbf{U} = \int_0^l \mathbf{F} ds\,. \tag{5.31}$$

Given the response W_m of a structure to m-th multipole moment of a point charge, also called *wake-function*, or *δ-function wake*, the integrated force on a trailing particle can be derived. Neglecting contributions from higher-order multipole components of the source charge, and employing a Cartesian coordinate system, one gets ([Cha93] §2.2):

$$\begin{aligned} \mathbf{U}_{\parallel}(z) &= -e\,q\,W_0'(z)\,\mathbf{e}_s\,, \\ \mathbf{U}_x(z) &= -e\,q\,W_1(z)\,\hat{x}\,\mathbf{e}_x\,, \\ \mathbf{U}_y(z) &= -e\,q\,W_1(z)\,\hat{y}\,\mathbf{e}_y\,, \end{aligned} \tag{5.32}$$

where z is the distance between source and test charge, $\hat{x}, \hat{y}$ are the horizontal resp. vertical position of the source charge, q its charge and $\mathbf{e}_x, \mathbf{e}_y$ are the transverse and $\mathbf{e}_s$ the longitudinal unit vector in the moving coordinate system of the source charge. The longitudinal wake field for the $m = 0$ case is independent of the transverse position of both the source and the test charge, while the horizontal and vertical kicks depend linearly on the offset of the source charge. Therefore the horizontal and vertical motion is decoupled for the $m = 1$ transverse wake fields. If the source of the wake field consists not of a single charge but a charge distribution, one has to integrate over this distribution to get the resulting kick on a trailing particle. The integrated impulse (kick) acting on a unit test charge is usually refered to as *wake potential* $\mathbf{w}$, and has the components:

$$\begin{aligned} \mathbf{w}_{\parallel}(\bar{s}) &= -\mathbf{e}_s \int \lambda(s)\, W_0'(\bar{s}-s)\, ds\,, \\ \mathbf{w}_x(\bar{s}) &= -\mathbf{e}_x \int \lambda(s)\, \bar{x}(s)\, W_1(\bar{s}-s)\, ds\,, \\ \mathbf{w}_y(\bar{s}) &= -\mathbf{e}_y \int \lambda(s)\, \bar{y}(s)\, W_1(\bar{s}-s)\, ds\,. \end{aligned} \tag{5.33}$$

Here s is the coordinate of the exciting charge distribution, $\bar{s}$ the position of the test particle, and the following definitions have been introduced:

$$\begin{aligned} \lambda(s) &\equiv \int \rho_c(x,y,s)\, dxdy\,, \\ \bar{x}(s) &\equiv \frac{1}{\lambda(s)} \int x\, \rho_c(x,y,s)\, dxdy\,, \\ \bar{y}(s) &\equiv \frac{1}{\lambda(s)} \int y\, \rho_c(x,y,s)\, dxdy\,. \end{aligned} \tag{5.34}$$

when $\rho_c(x,y,s)$ is the charge distribution. The details of the derivation can be found in [Sab94a]. For a macro-particle distribution the equations are valid, but one has to use an averaged continuous density function.

To illustrate the situation in a axially symmetric structure, the transverse wake potential induced by a beam with a Gaussian longitudinal distribution is shown in Figure 5.1 for a circular "pillbox" cavity with side-tubes. A small circle indicates the position of the beam. The beam has no azimuthal dependence and no transverse spatial extension. For a finite beam offset all multipole components are excited in the structure. As can be seen clearly, the kicks on a trailing particle are practically independent of the transverse position, and are always in radial direction. The transverse kicks for an on-axis beam are negligible.

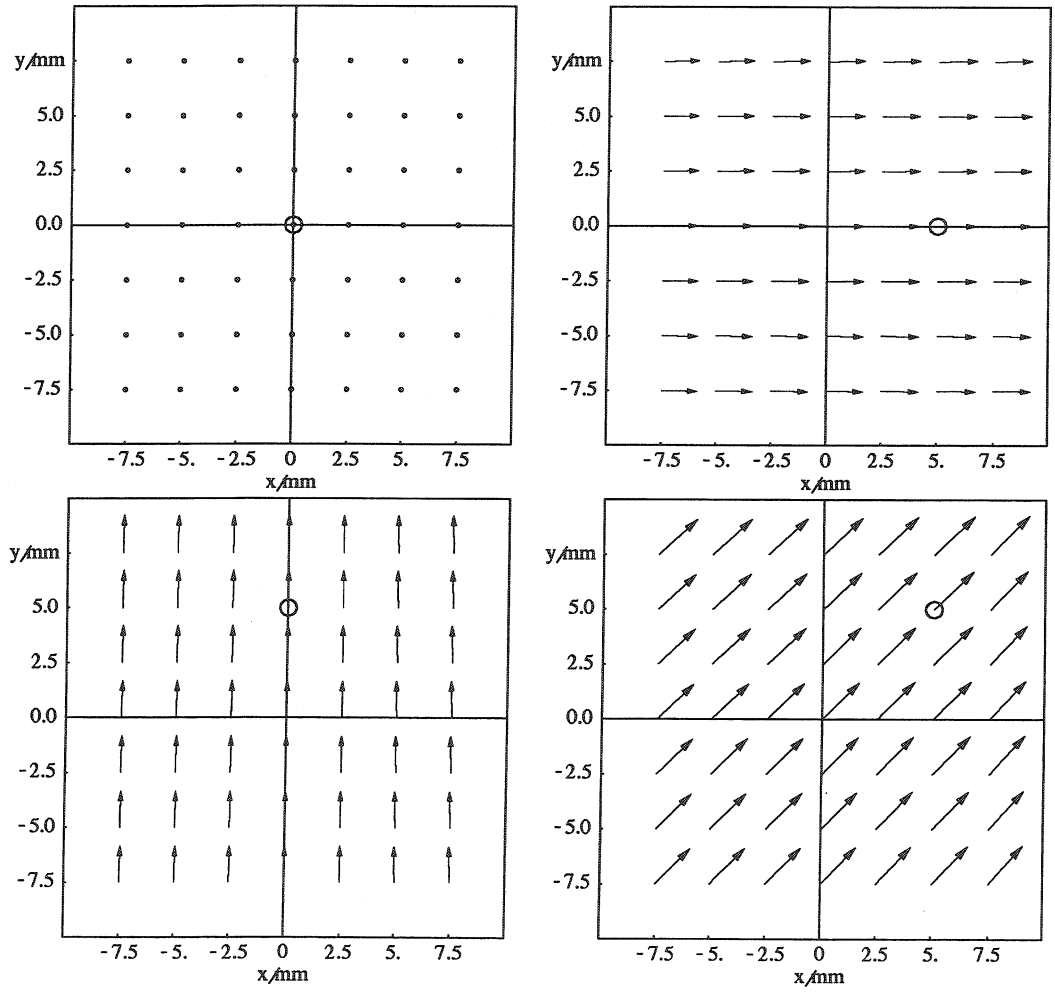

Figure 5.1: Transverse kicks as function of horizontal and vertical position in a axial symmetric structure for different beam offsets, the beam position is indicated by a small circle.

Up to now it has been assumed that the *wake function* of a point charge is known for the structure. Only for a few simplified structures the wake function can be calculated analytically (see e.g. [KZ97]). The numerical computation of the wake function in time domain also does not lead to satisfactory results, despite some approximations which have been suggested [Kei72, BW80, BZ82].

For a simulation program it has therefore been found advantageous to use a set of basis-functions with finite length and to expand the actual charge distribution in terms of them. Since the equilibrium bunch distribution at low intensities is Gaussian, the first choice was a series of Hermite polynomials [Nys87, Wan90]. The wake potential tables for polynomials up to the 6-th order were precalculated for several bunch lengths and for azimuthal orders $m = 0$ and $m = 1$. This yielded 15, look-up tables, each one a 25x640 array, which had to be stored. For higher currents - close to the stability threshold - the bunch distribution becomes usually more and more non-Gaussian. A sufficiently accurate representation of the distribution using Hermitian polynomials would require a larger number of terms of the series expansion.

To overcome this limitation a set of linear basis functions was introduced [Sab95a]. An arbitrary distribution can be well approximated using a suitable number of triangular shaped basis functions. The number of wake potential tables needed can thereby be limited to a single one for each direction, a $m=0$ wake for the longitudinal direction and a $m = 1$ wake for one transverse direction. The expansion of a multi-particle distribution using such triangles is also very efficient in terms of computing time. However, for the simulation of short bunches one needs to calculate the wake potentials of very short triangular bunches. Due to the discontinuity in the first derivative of triangles, high frequencies are excited and their computation demands very small longitudinal mesh step sizes. By using Gaussian basis functions for the simulation of very short bunches it was found that these problems can be avoided [Mei97]. The drawback is a somewhat longer time needed for the expansion of the macro-particle distribution.

In the simulation program TRISIM3D, as can be guessed from its name, triangular shaped basis functions were chosen. This choice was made since CPU time is critical issue for the simulation in all 3 spatial dimensions. However, an option can easily be implemented to allow the choice of Gaussian basis functions.

5.3.2 Non-axially-symmetric structures

To describe the wake potentials in non-axially symmetric structures the introduction of the so called generalised impedance concept is necessary. The magnitude of the wake fields no longer only depends on the offset of the source charge, but also the transverse position of the test charge will influence the magnitude and direction of the kicks [2]. In this case, the wake fields induced in structures which are not axially symmetric can generally be written as a series

$$\mathbf{w}(\mathbf{r},\bar{\mathbf{r}},s) = \sum_{n=0}^{\infty}\sum_{m=0}^{\infty} \mathbf{r}^n \bar{\mathbf{r}}^m \mathbf{w}_{n,m}(\mathbf{r},\bar{\mathbf{r}},s). \tag{5.35}$$

where $\mathbf{r}$ resp. $\bar{\mathbf{r}}$ are the radius vectors of source resp. test charge position and s the distance from the bunch head. In a Cartesian coordinate system the horizontal component of this series can be written as

$$\mathbf{w}^{(x)}(x,y,\bar{x},\bar{y},s) = \sum_{i=0}^{\infty}\sum_{k=0}^{\infty}\sum_{n=0}^{\infty}\sum_{m=0}^{\infty} x^i y^k \bar{x}^n \bar{y}^m \mathbf{w}^{(x)}_{i,k,n,m}(x,y,\bar{x},\bar{y},s)$$

and equivalent expressions for the other directions[3], here x, y resp. $\bar{x}$, $\bar{y}$ are the transverse coordinates of test resp. source charge.

The aim is to find the components of this series which yield the major contribution. Similar as for the axially symmetric case, there are only a few components important to describe the wake field response of a structure sufficient accurately.

As mentioned before, most structures used in accelerators still have one or more symmetry planes. Therefore simply for symmetry reasons many of the terms in Eqn. 5.36 vanish. The LEP shielded bellows model, introduced in §4.4.2, will be employed as an example of an elliptic structure. The dependence of the kicks on the transverse position of source and test distribution is shown in Figure 5.2. A conspicuous difference to the axially symmetric case is that the transverse kicks for an on-axis source beam are no longer negligible. The patterns for a source beam with offset are no longer simple dipole fields, they resemble the field pattern in a quadrupole.

[2] The variation of the longitudinal impedance with transverse displacement can be used to determine the transverse impedance [NS79].

[3] The indices of $\mathbf{w}^{(x)}_{i,k,n,m}(x,y,\bar{x},\bar{y},s)$ refer to the power of the coordinates of source and test charge.

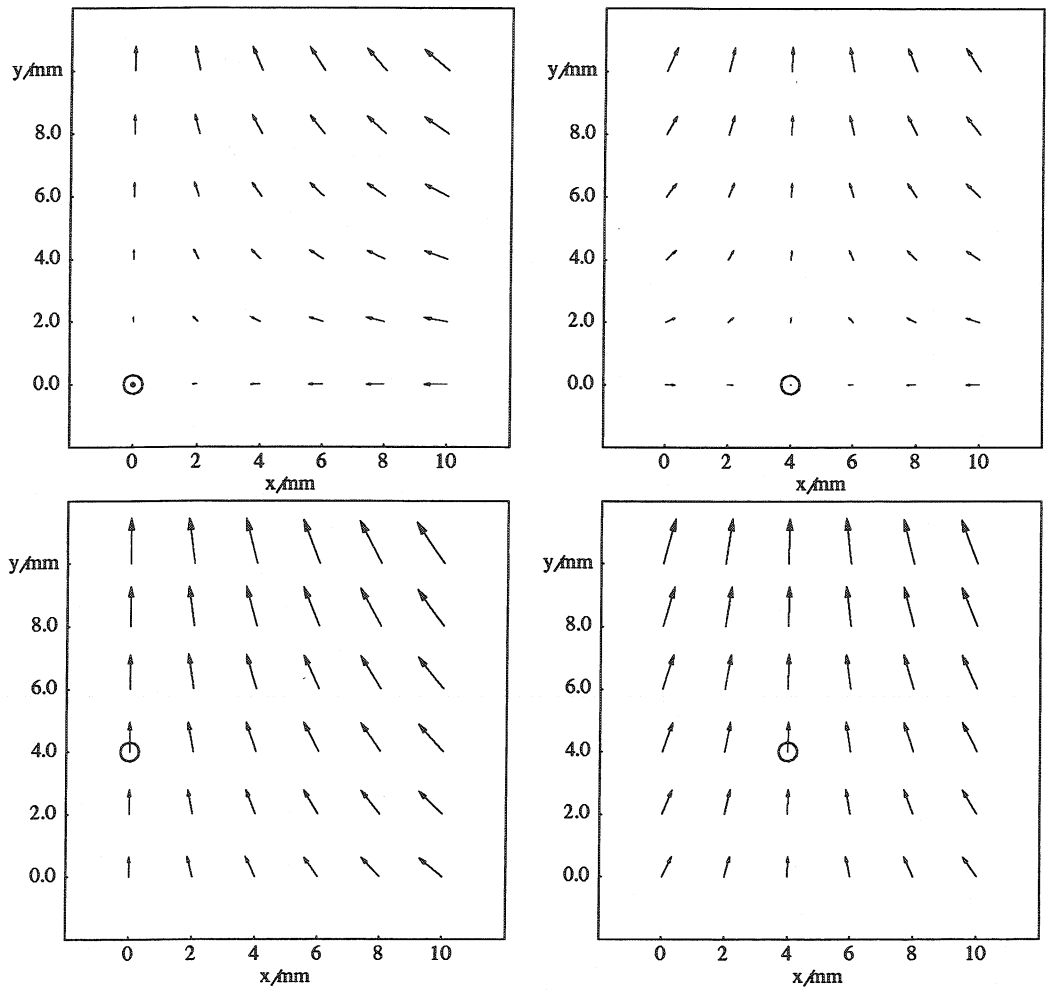

Figure 5.2: Transverse kicks as function of horizontal and vertical position in an elliptic structure (LEP shielded bellows) for different beam offsets, the beam position is indicated by a small circle.

The kick due to the quadrupolar field, induced by an on-axes beam, only depends on the offset of the test charge. One can therefore subtract these fields from the fields for an beam with finite offset. The results are shown in Figure 5.3. Like for the symmetric structures, the patterns resemble now simple dipole fields, similar to those of axially symmetric structures. The magnitude of the dipole component depends mainly on the offset of the source charge, only for very large relative displacement of the test charge there is some distortion of the dipole field visible.

Neglecting higher order components, the transverse wake effects can be well approximated by a superposition of a dipole and a quadrupole wake compo-

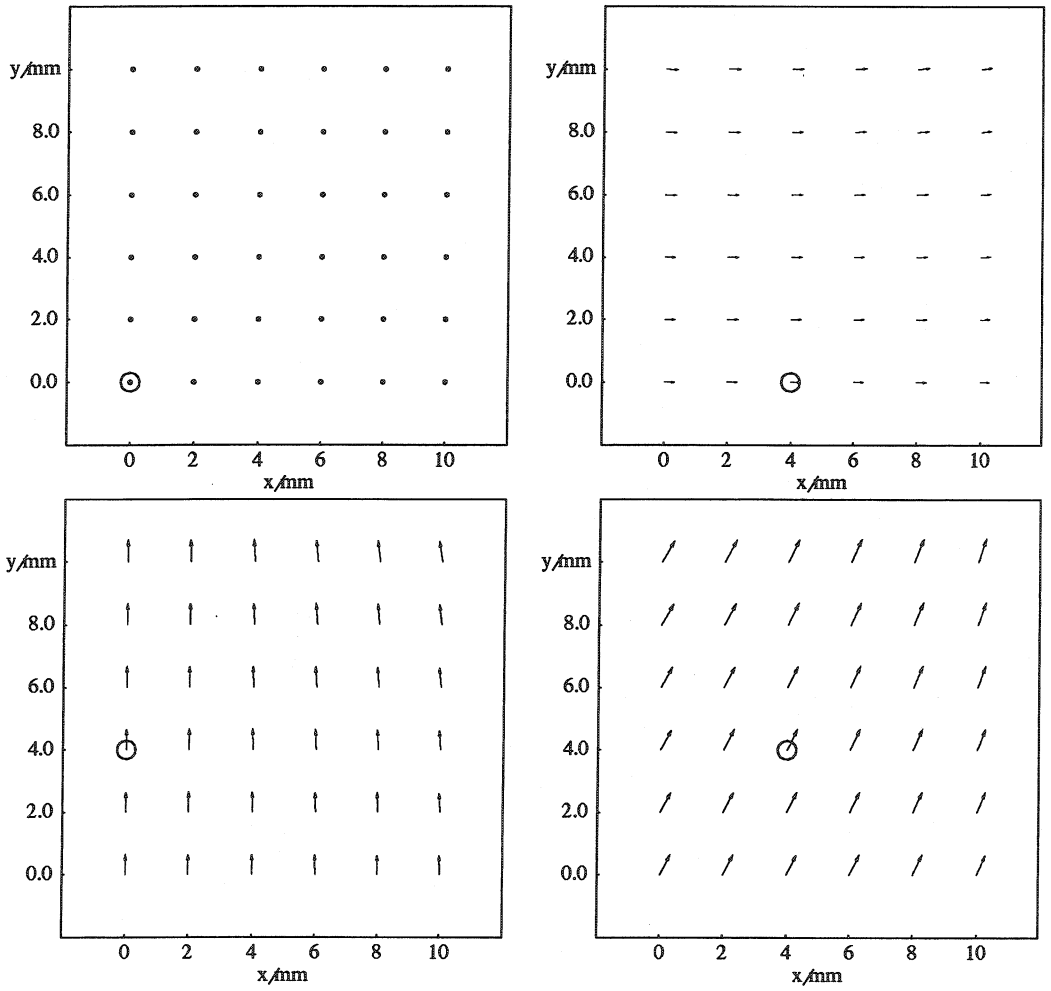

Figure 5.3: Transverse kicks reduced by the kicks due to an on-axis beam in an elliptic structure (LEP shielded bellows) for different beam offsets, the beam position is indicated by a small circle.

nent[4]

$$\mathbf{w}^{(x)}(x,y,\bar{x},\bar{y},s) \approx x\,\mathbf{w}^{(x)}_{1,0,0,0}(x,s) + \bar{x}\,\mathbf{w}^{(x)}_{0,0,1,0}(\bar{x},s), \tag{5.36}$$

$$\mathbf{w}^{(y)}(x,y,\bar{x},\bar{y},s) \approx y\,\mathbf{w}^{(y)}_{1,0,0,0}(x,s) + \bar{y}\,\mathbf{w}^{(y)}_{0,0,1,0}(\bar{x},s). \tag{5.37}$$

For the simulation program there are essentially 5 wake tables per machine element needed to describe elliptic structures with this first order approxima-

[4]The superposition of a quadrupole and a dipole component of the fields is the reason for sometimes very small horizontal loss factor in non-axially symmetric structures (see Chapter 4). When the dipole and the quadrupole component are of the same order of magnitude they may almost cancel each other.

tion, one for the longitudinal and two for each transverse direction. The major difference to axially symmetric structures is this offset dependent quadrupolar wake potential acting on a trailing particle.

The contributions of transverse coupling terms was found to be weak, e.g. an additional vertical offset does not significantly change the horizontal wake potential. Their possible influence on the particle motion will be investigated in chapter 7.

Electrostatic Separator:

The second non-axially symmetric LEP structure used for the TRISIM3D runs, are the electrostatic separators. Even though the structure is not elliptic, the field patterns are quite similar to those of the elliptic bellows (Fig.5.4).

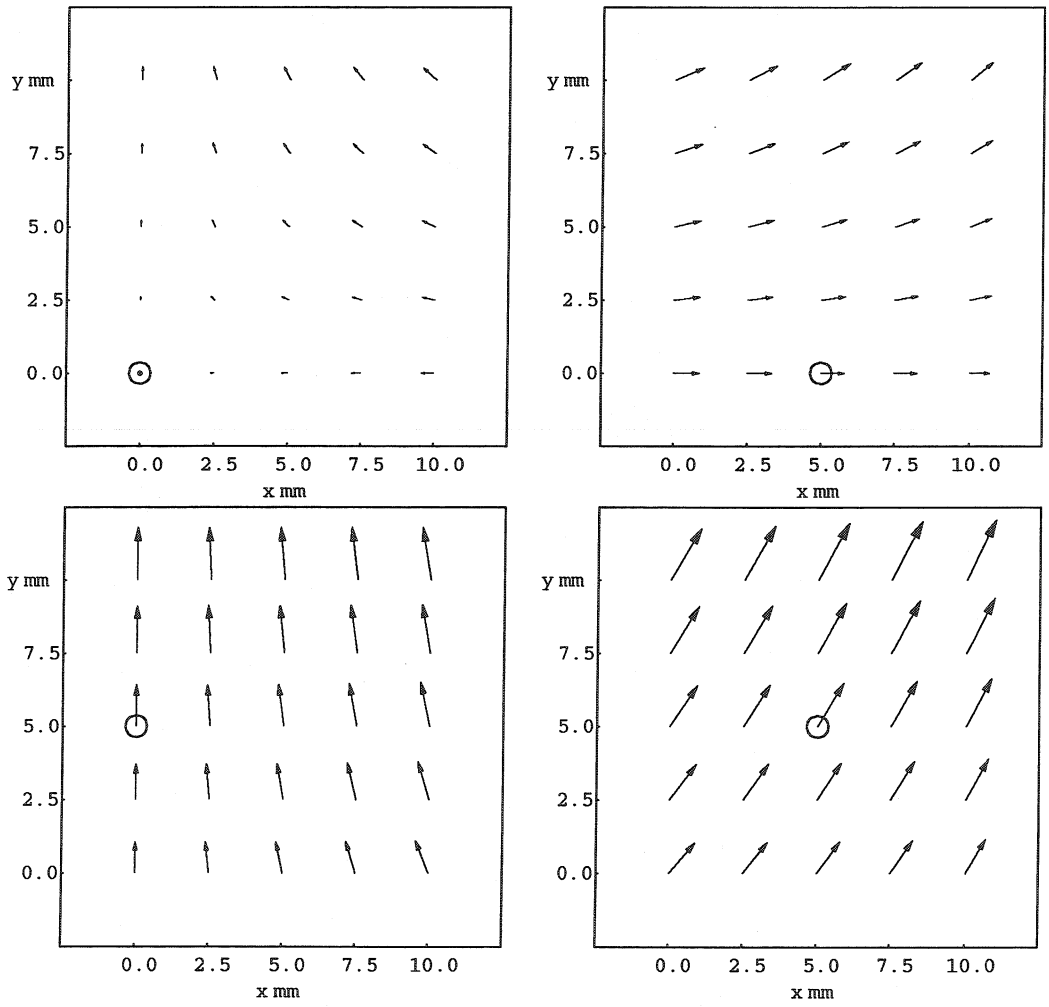

Figure 5.4: Transverse kicks as function of horizontal and vertical position in a LEP electrostatic separator for different source beam offsets, the position of the beam is indicated by a small circle.

If one subtracts the quadrupole component from the fields of a beam with finite offset, the pattern resembles again a simple dipole field (Fig.5.5). In addition there are again some weak higher order components which can be seen clearly for larger beam offsets, but since the contribution of the separators to the

transverse impedance of LEP is only about 10%, these higher order components will not have a strong influence on the particle motion.

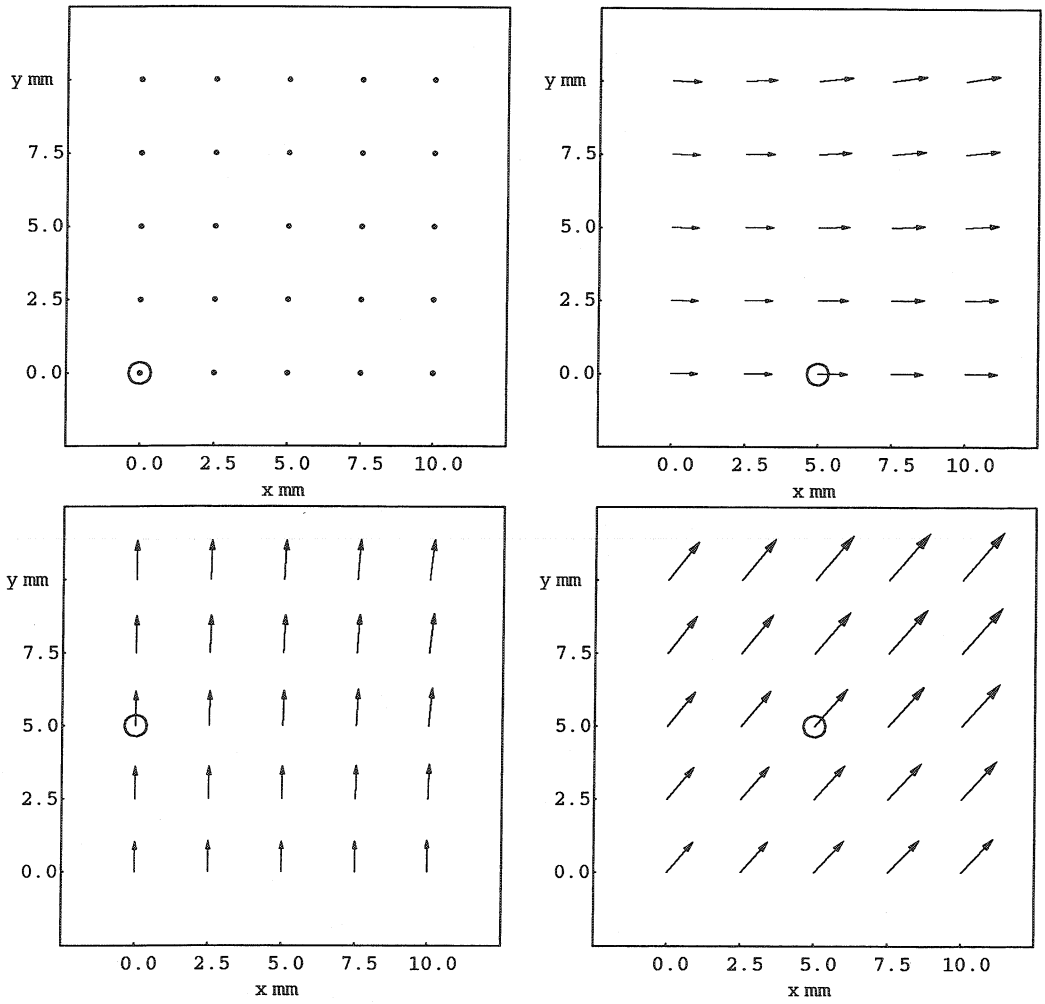

Figure 5.5: Transverse kicks reduced by those due to an on-axis beam as function of horizontal and vertical position in a LEP electrostatic separator for different source beam offsets, the position of the beam is indicated by a small circle.

5.4 Machine model

The number of structures in a large accelerator, whose wake-field kicks have to be taken into account, is too high to consider each one separately. It would lead to very large CPU-time consumption, since it increases linearly with the number of elements. Therefore many elements have to be grouped together in a few, typically less than 10 elements. One thus concentrates the effects of many into a few elements. The dependence of the simulation results on this number of elements is not very strong, as was shown in [Sab95a].

A recent measurement of the longitudinal energy loss in LEP provides a suitable machine model for LEP (Fig. 5.6 [A+97]).

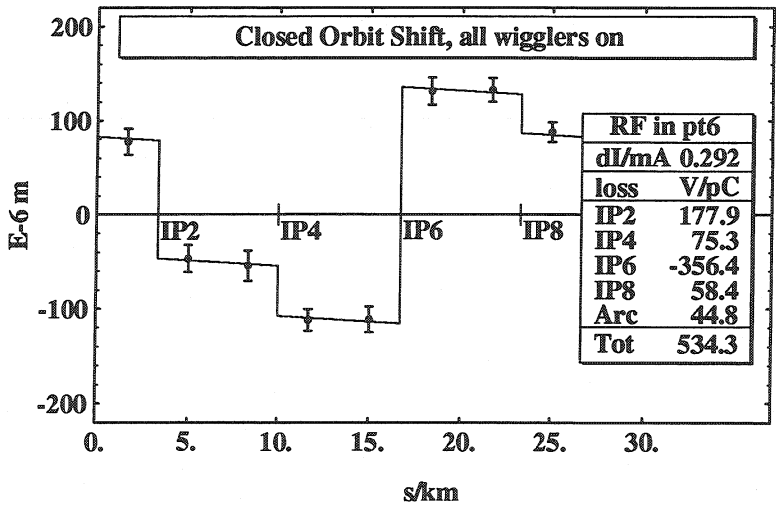

Figure 5.6: Closed orbit shift in LEP

In this experiment the *closed-orbit shift* was measured as function of the bunch current . The RF cavities in LEP are located close to the interaction regions IP2, IP4, IP6 and IP8. Only the cavities in one point were powered (IP6 in Fig. 5.6). Due to many distributed impedances the bunch looses energy, while traversing the arc sections, which can be seen as downwards slope of the curve. At the IP's with the inactive cavities, a sudden drop of the orbit displacement caused by the high energy loss in the cavities in points 2,4 and 8 is clearly visible. All the energy lost along the ring is replaced in the powered cavities in point 6.

The corresponding machine model for the simulation program is shown in Figure 5.7.

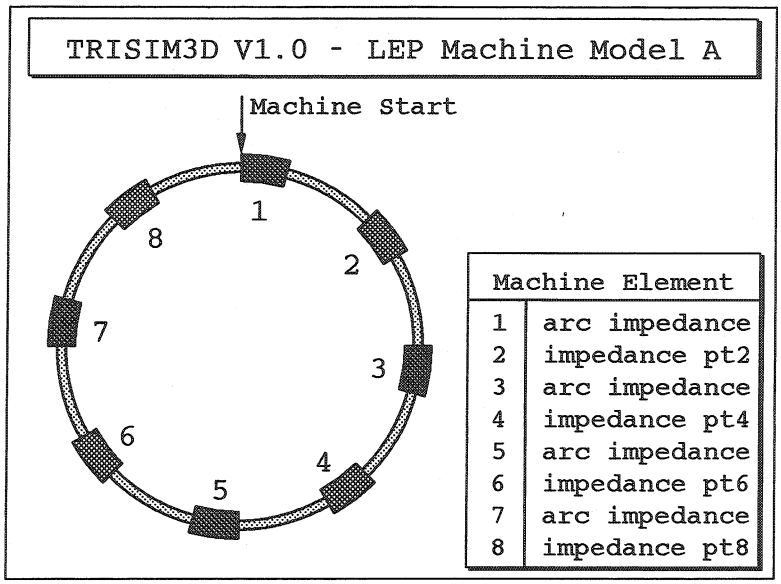

Figure 5.7: Machine Model A: Complete LEP machine model for TRISIM3D

However, for many applications even simpler models can be used. As a general rule, if several elements of a machine model are combined into a single one, the effects are always stronger. This rule can be easily be explained by imagining a machine model with only one element. For certain parameter settings a resonance condition can be fulfilled, i.e. the kicks at successive turns can be in phase with the oscillation of a particle. The integer parts of the transverse tunes do not have any influence in this single element machine model. If one splits the impedance into more elements, the phase advance between elements depends now additionally on the integer tune which may result in avoiding the resonance condition.

Since the CPU time increases linearly with the number of elements, it saves quite some time, if one uses a simple model to make rough scans over parameter settings, and to use a more detailed model later, to make more precise studies.

Chapter 6

Applications and Results

The results presented in this chapter cannot represent a comprehensive analysis of the underlying physics. Only a few qualitative studies of some effects, emerging from the capabilities of a 3-D program, will be presented. They are meant to be examples of possible applications of the simulation program.

6.1 LEP Machine Configuration

The number and type of vacuum components installed in the different sections of LEP are listed in Table 6.1, the values are for the LEP configuration of 1997. The major contribution ($\approx$80%) to the longitudinal impedance comes from the super-conducting and copper cavities, while to the transverse impedance also the shielded bellows contribute with about 30 %. There are only two types of unshielded bellows in the list of elements which are representative for a larger number of different kinds of these bellows in the real machine. The number of installed items was obtained from the impedance database program ZBASE [Brü96]. This database was set up to keep track of the steadily varying number and types of vacuum components installed in LEP and LHC, as far as they are relevant for collective effects.

The machine model employed for the studies in the next sections will be one of the following three models:

- Model A : The machine is represented by 8 elements. The impedance of the elliptic shielded bellows is divided into four arc sections. The cavities and other components are grouped, corresponding to their number, into four different elements representing the straight sections.

LEP					
element	pt2	pt4	pt6	pt8	total
copper cavity cell	130	—	300	—	430
SC - cavity module	16	18	8	18	60
SC - cavity taper	4	5	2	4	15
separator	12	13	12	13	50
unshielded bellows short	40	40	40	40	160
unshielded bellows long	30	30	30	30	120
elliptic shielded bellows	2750				2750

Table 6.1: Number of LEP structures 1997

- Model B : In this 2 element model, all straight section elements are combined into one machine element, also the elliptic shielded bellows will be represented in one element.
- Model C : The simplest model of the three consists only of one machine elements in which all wake potential effects are concentrated.

As mentioned before, the CPU time increases linearly with the number of elements, therefore the simpler models B and C are employed for parameter scans.

The wake potentials of the different structures combined in an element are combined with the subprogram TTAB3D and weighted with the averaged values of the beta-functions at their locations. As an example, the output of this program for the vertical dipole wake potential (m=1) for the single-element model is shown in Figure 6.1.

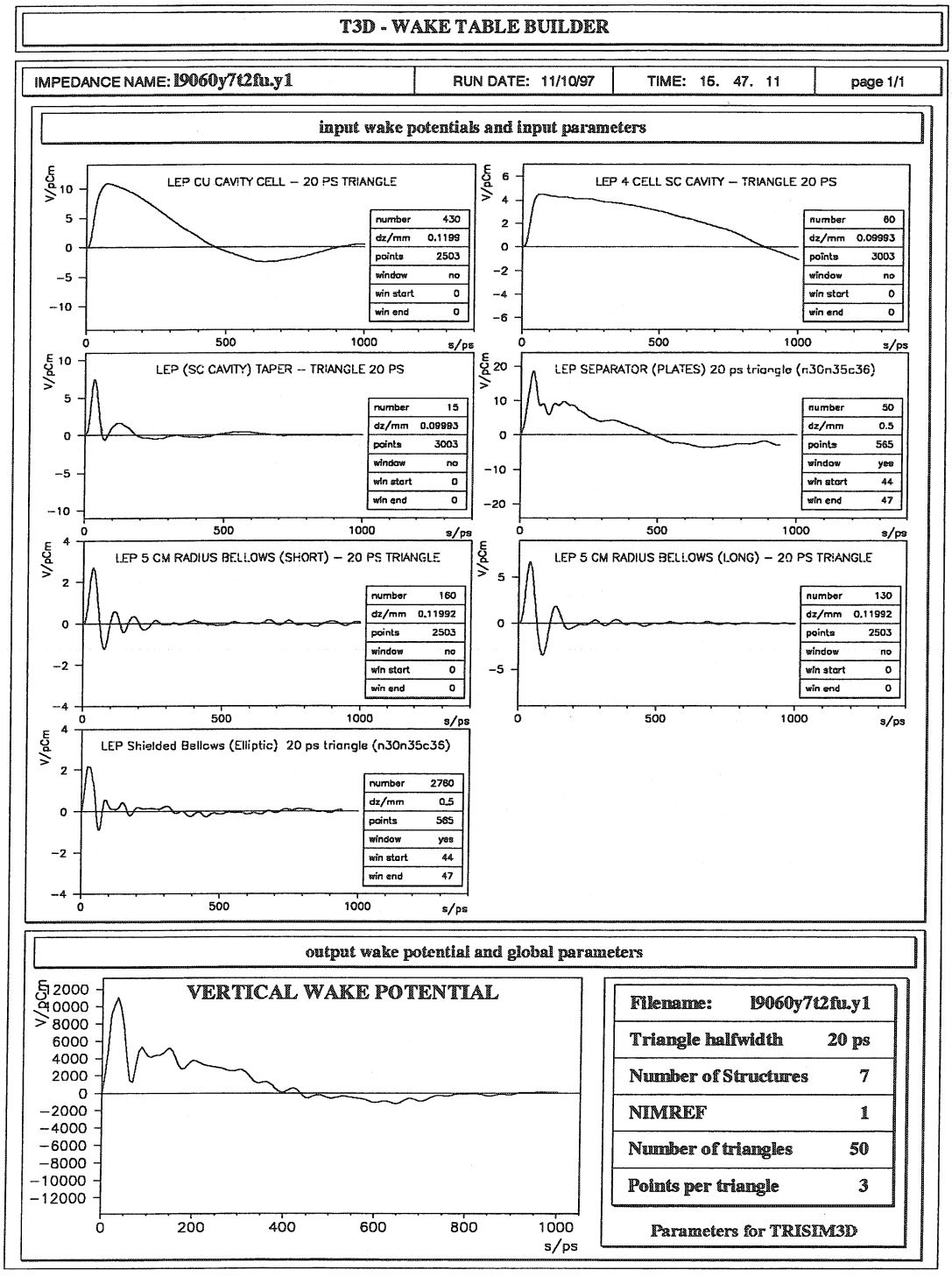

Figure 6.1: Vertical wake potentials combined into one machine element: LEP 90/60 optics, year 1997, 20 ps triangles.

6.2 Horizontal-Vertical Wake Field Coupling

To study the effects of wake field coupling, the machine model C will be used. The wake potential components $\mathbf{w}^{(x)}_{x,y^2}$ and $\mathbf{w}^{(y)}_{x^2,y}$, which were found to be the strongest coupling components, lead to a coupling between the motion in the two transverse planes. We examine the effect of this coupling on the macroscopic motion of the bunch. The first simulation run was started with the horizontal-vertical coupling switched off, after 6000 turns the coupling is switched on, indicated by a dashed line in Figure 6.2, page 107. There are no significant changes visible, neither in the position nor in the beam-sizes. There are some fluctuations of the transverse beam positions, but these are due to the quantum excitation simulated with random numbers. For comparison the results for a run, in which the coupling remains switched off, is shown in Figure 6.3, page 108 (the same set of random numbers was used). The reason for the lack of any influence of the coupling is the magnitude of the resulting kicks (Figure 6.4). The kicks due to the coupling wake-potential are several magnitudes smaller than those of the vertical one. Amplifying the strength of the coupling wake, by multiplying the kicks due the wake potentials with a factor c_{cpl}, is shown in Fig.6.4, page 110. The strength of the kicks is multiplied by a factor of 10 each 5000 turns. When the multiplication factor reaches 10^4, the wake field coupling gets bigger than the dipole one, and the sum of both both added lead to loss of particles.

This large ratio between kick strength due to the dipole and the wake potential coupling is certainly an overestimate, since only the strongest coupling component has been taken into account. Furthermore, it was assumed that all structures are perfectly aligned, since the coupling components scale quadratically with the offset of the beam in the other transverse direction, any misalignment would therefore lead to an large increase of the coupling strength.

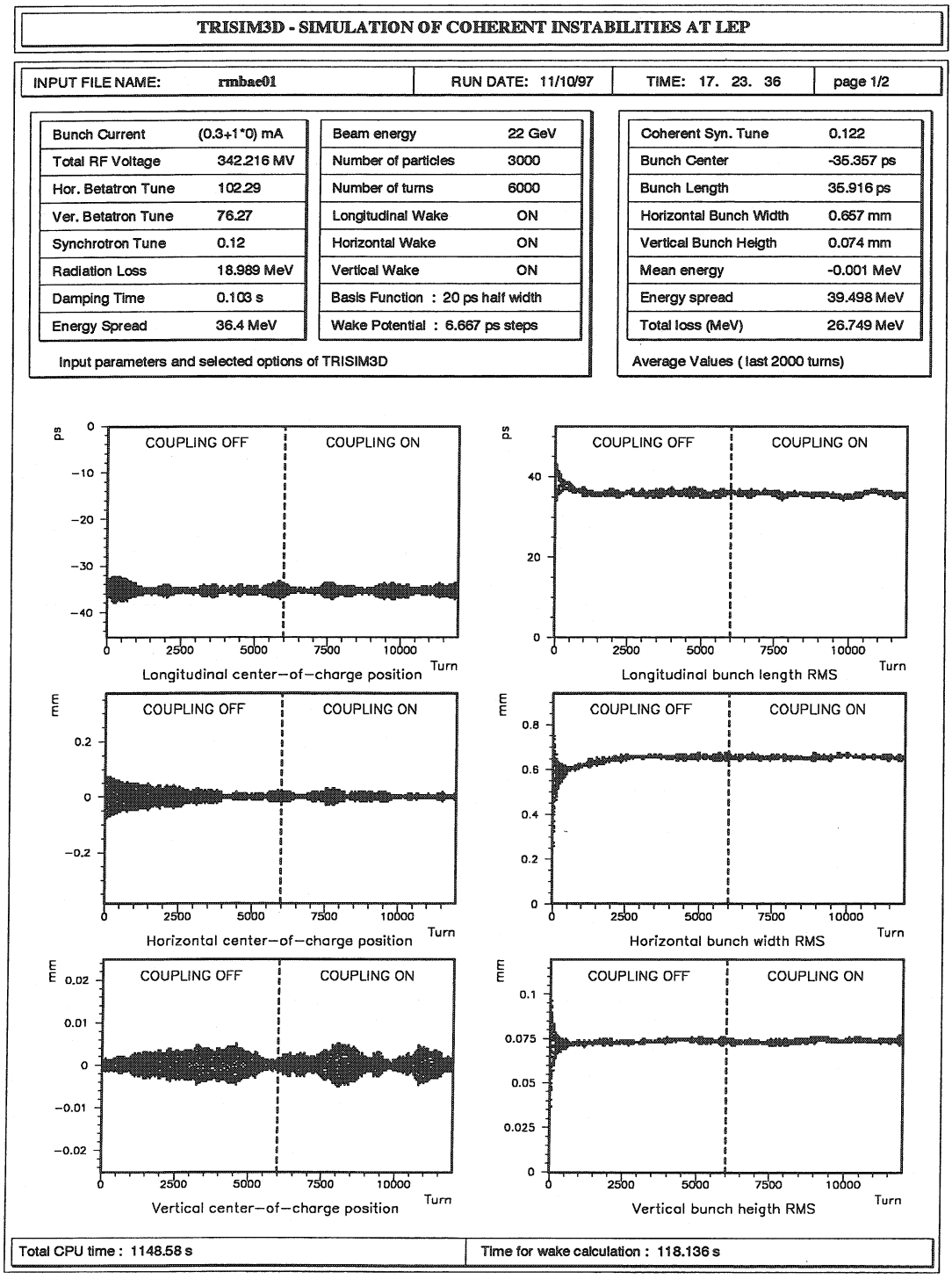

Figure 6.2: Wake potential coupling switched on at 6000 turns: LEP 90/60 optics, year 1997, 20 ps triangles.

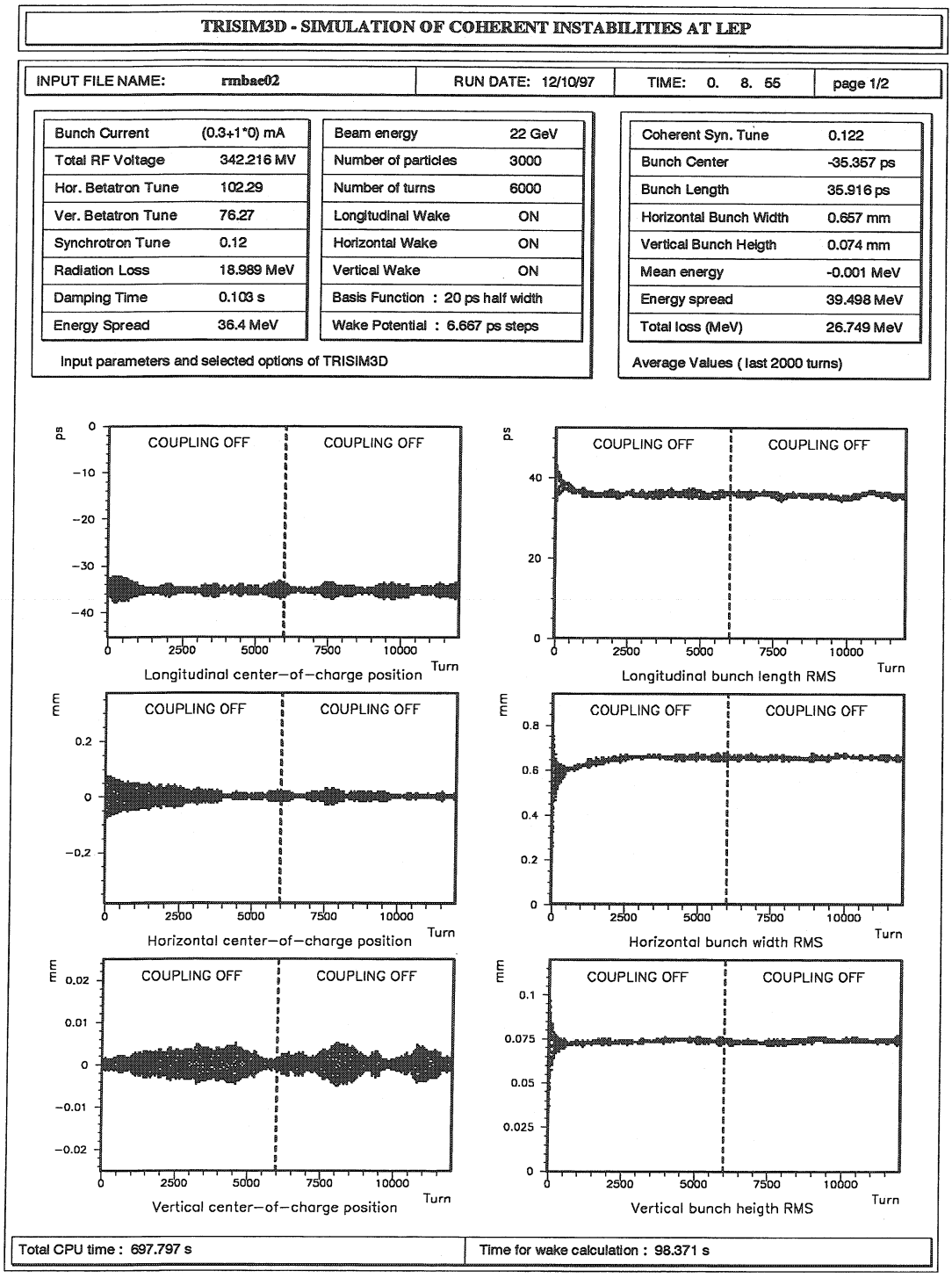

Figure 6.3: Wake potential coupling off: LEP 90/60 optics, year 1997, 20 ps triangles.

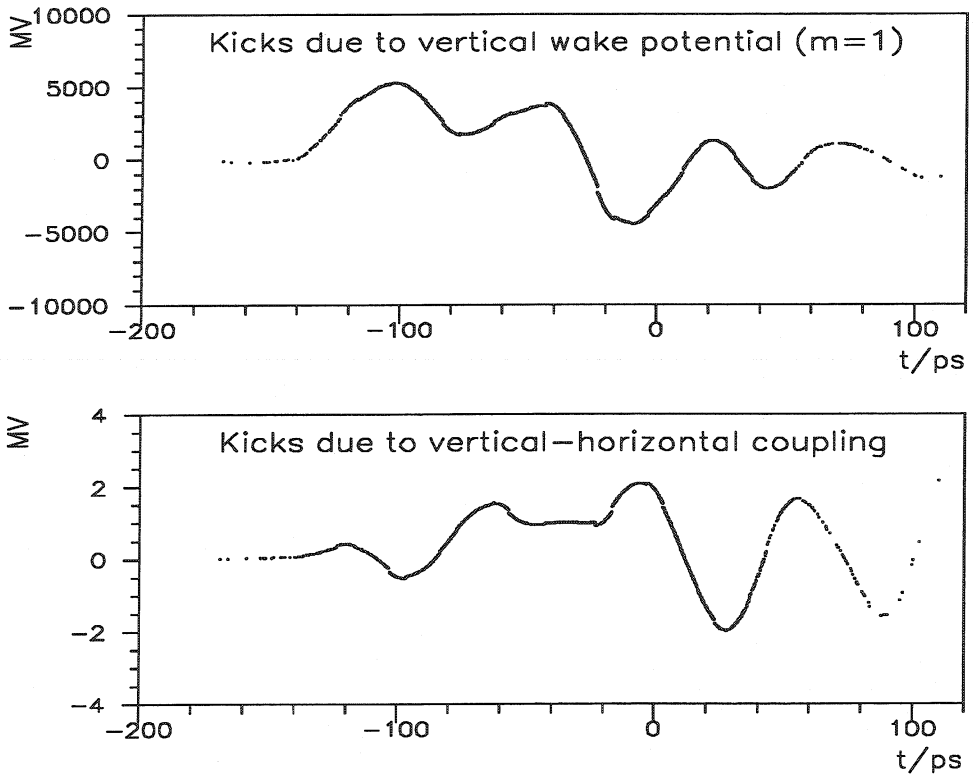

Figure 6.4: Vertical kicks due to the vertical and the vertical-horizontal coupling wake potential.

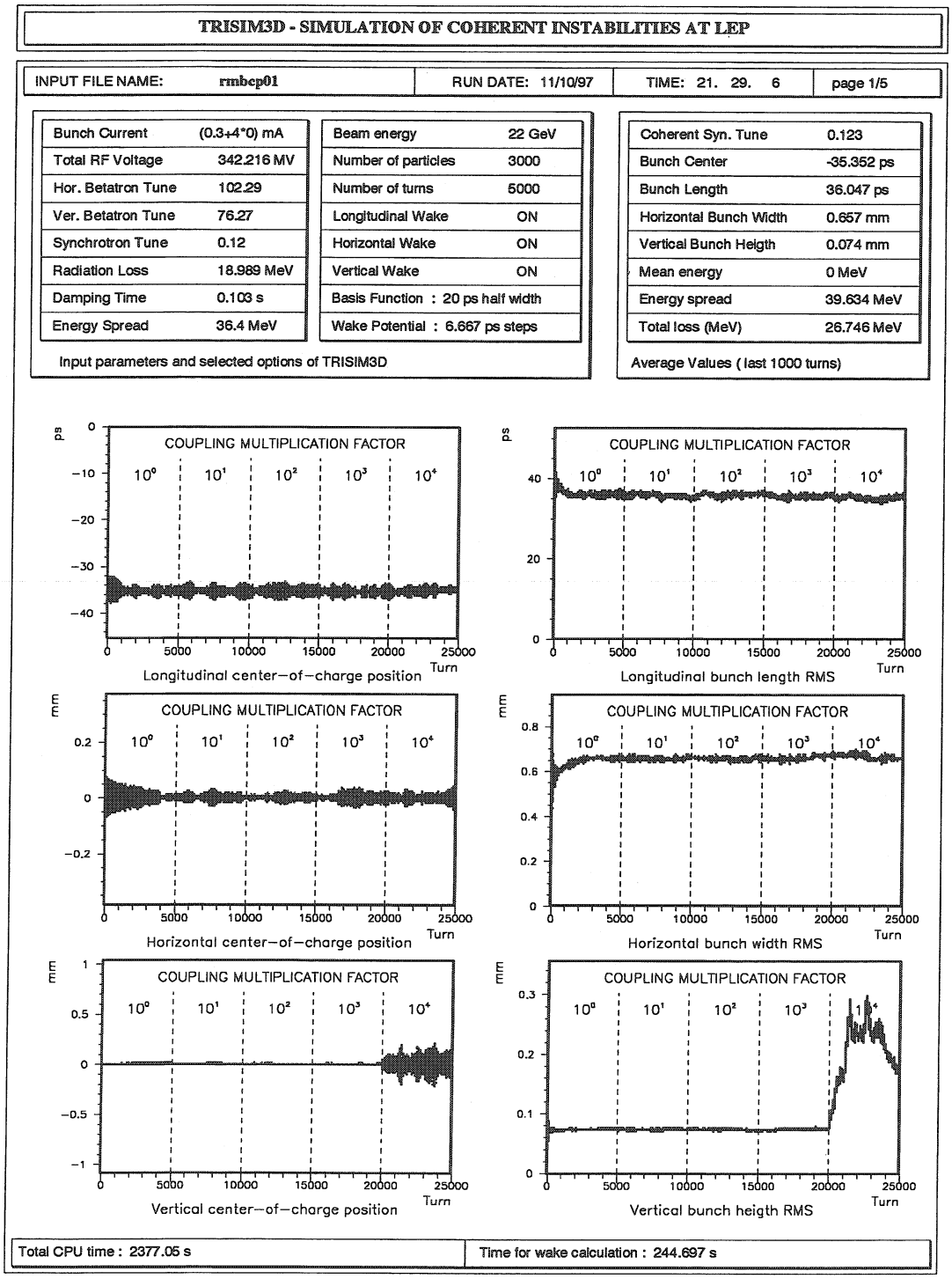

Figure 6.5: Wake potential coupling increased by a factor 0f 10 each 5000 turns.

6.3 Coupling Due to Skew Quadrupoles

The coupling due to wake potentials was found to be weak. Another possible source of horizontal-vertical coupling are skew quadupolar fields. The machine model used is the two element model B with an additional skew quadrupole element. The emittance coupling factor κ will be set to zero, the *natural* vertical emittance will also vanish (Eqn. 5.21). The vertical beam size would, due to radiation damping, also be zero if the skew quadrupole is not powered. For a finite initial vertical beam height, this situation is shown in Figure 6.6, page 112. In the vertical initial conditions are zero also the beam size remains zero (Figure 6.7, 113).

When powering the skew quadrupole the vertical beam size increases depending on its strength. This growth is shown in Fig. 6.7.

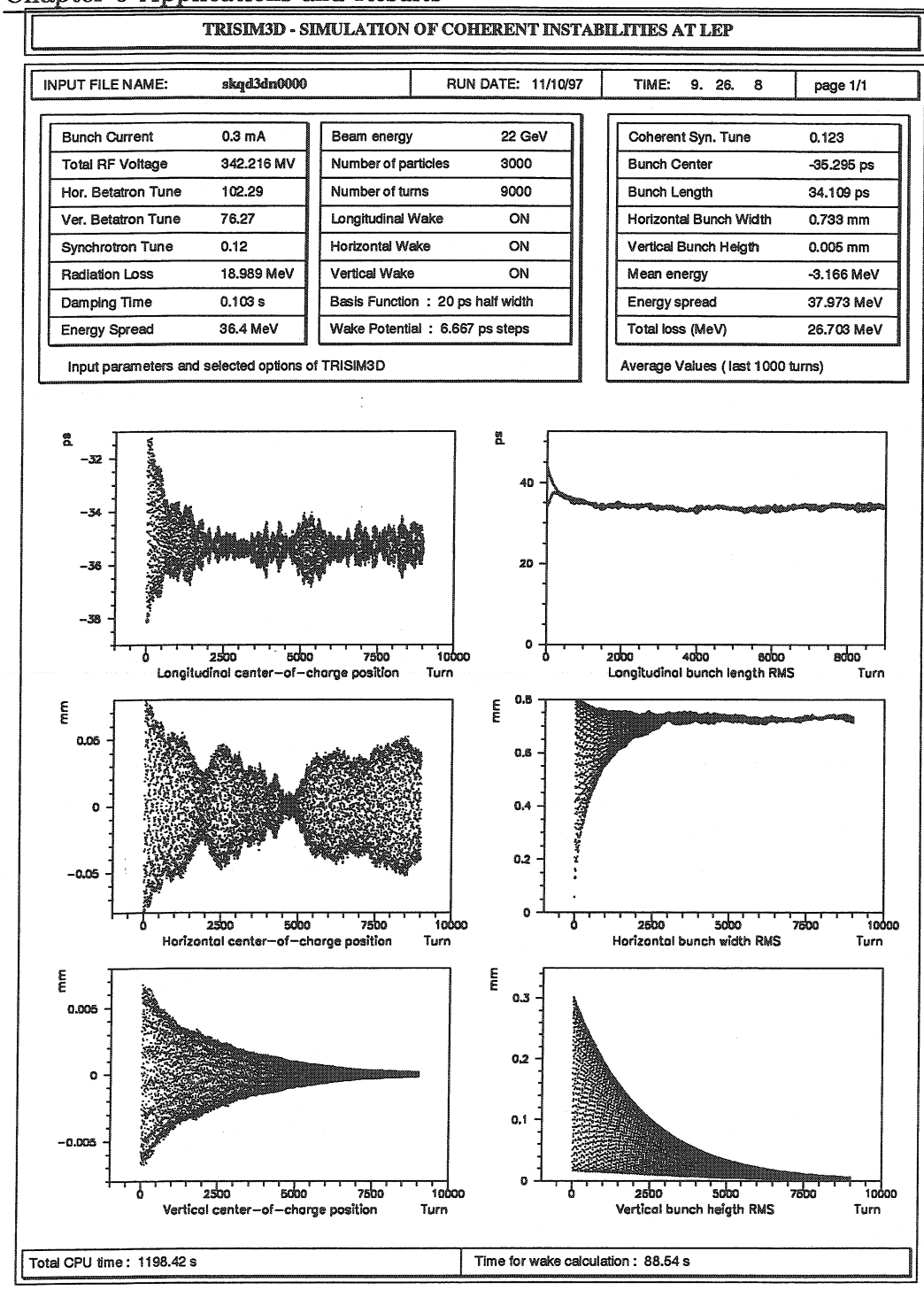

Figure 6.6: Damping of the vertical beam size.

TRISIM3D - SIMULATION OF COHERENT INSTABILITIES AT LEP

INPUT FILE NAME:	skqd3d0b	RUN DATE: 13/10/97	TIME: 1. 53. 57	page 1/1

Bunch Current	0.3 mA	Beam energy	22 GeV	Coherent Syn. Tune	0.123
Total RF Voltage	342.216 MV	Number of particles	3000	Bunch Center	-35.444 ps
Hor. Betatron Tune	102.29	Number of turns	6000	Bunch Length	33.438 ps
Ver. Betatron Tune	76.27	Longitudinal Wake	ON	Horizontal Bunch Width	0.725 mm
Synchrotron Tune	0.12	Horizontal Wake	ON	Vertical Bunch Heigth	0 mm
Radiation Loss	18.989 MeV	Vertical Wake	ON	Mean energy	-3.166 MeV
Damping Time	0.103 s	Basis Function : 20 ps half width		Energy spread	37.257 MeV
Energy Spread	36.4 MeV	Wake Potential : 6.667 ps steps		Total loss (MeV)	26.815 MeV
Input parameters and selected options of TRISIM3D				Average Values (last 1000 turns)	

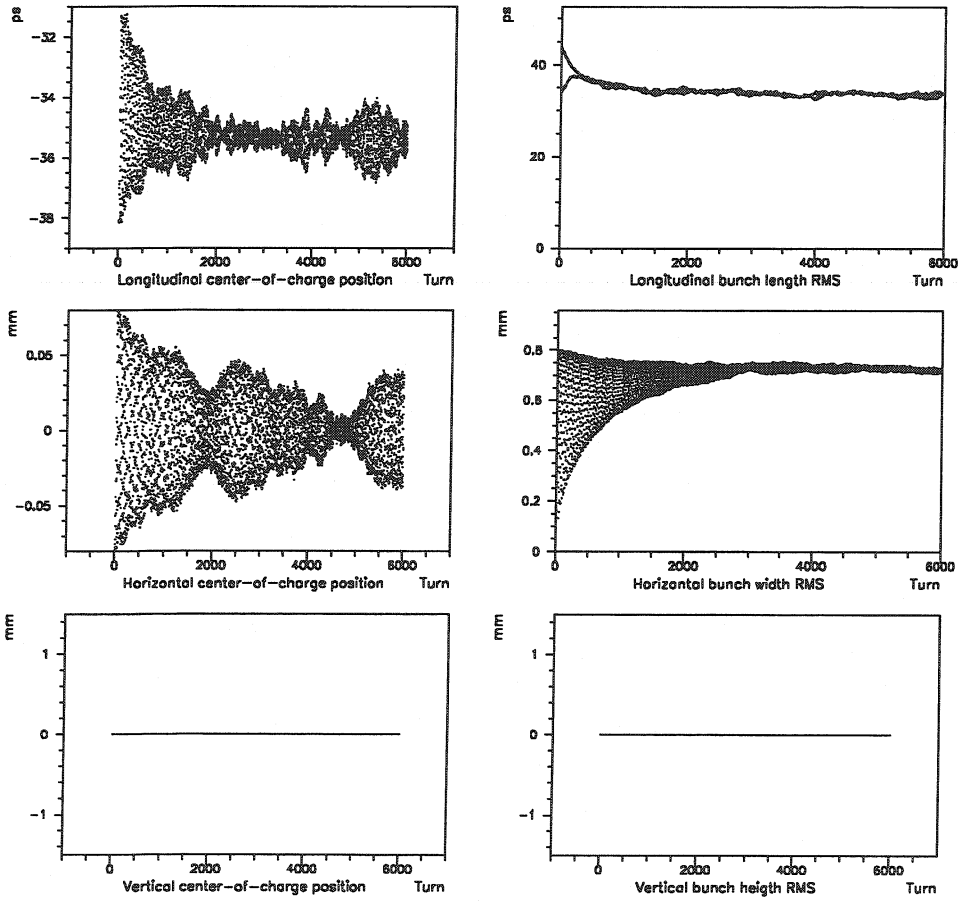

Total CPU time : 797.461 s	Time for wake calculation : 58.967 s

Figure 6.7: Zero vertical beam size.

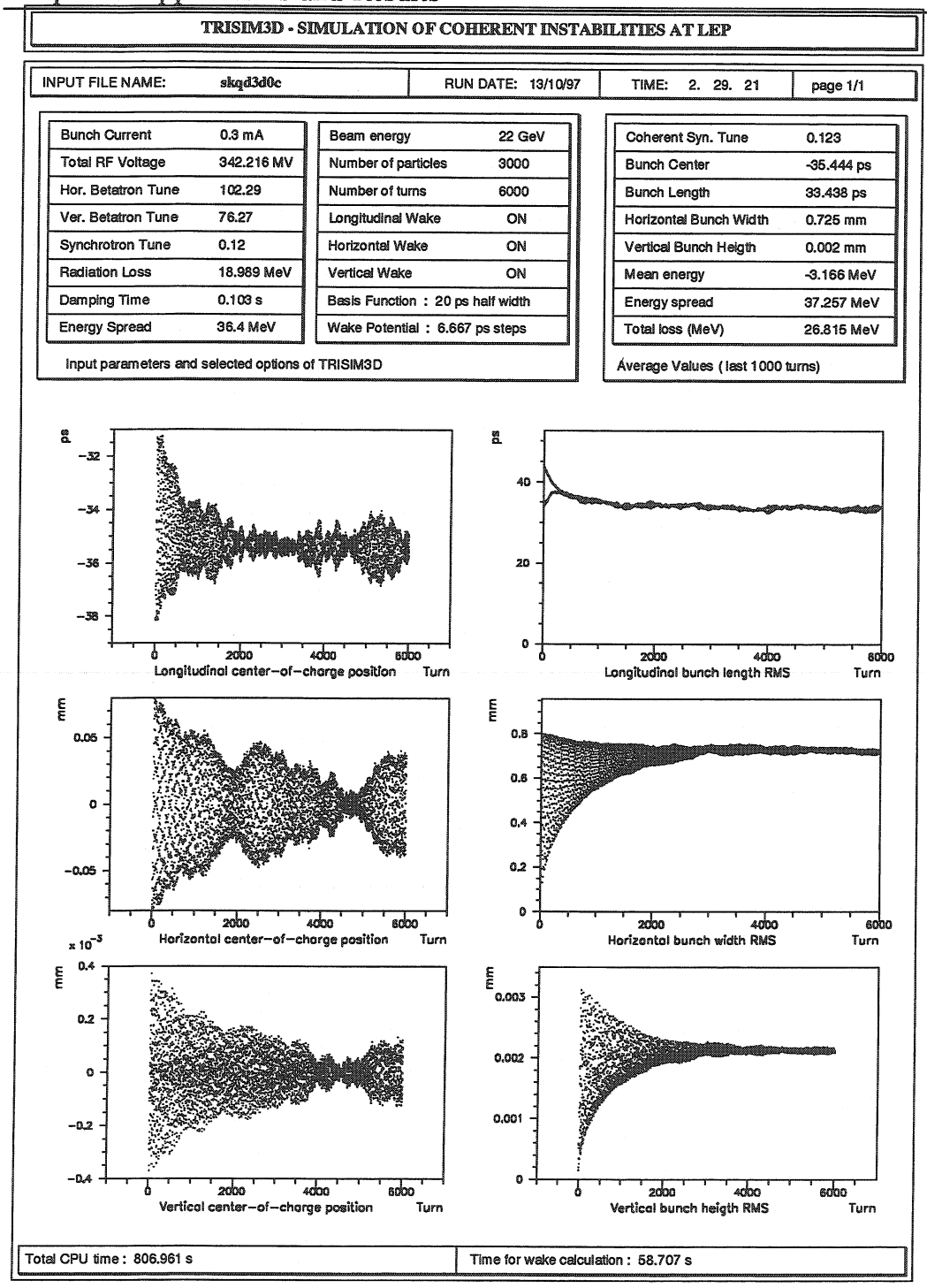

Figure 6.8: Vertical beam size due to skew quadrupole.

6.4 Horizontal and Vertical Tune Shifts

One of the simplest methods to estimate the transverse impedance in an accelerator is to measure the dependence of the transverse betatron tunes on the beam current. The tune slope with current is directly proportional to the effective impedance, i.e. the convolution of the machine impedance with the bunch spectrum. The results of the computer simulation of LEP at injection energy are shown in Figure 6.9. The machine model A with 8 equidistant impedance locations has been used.

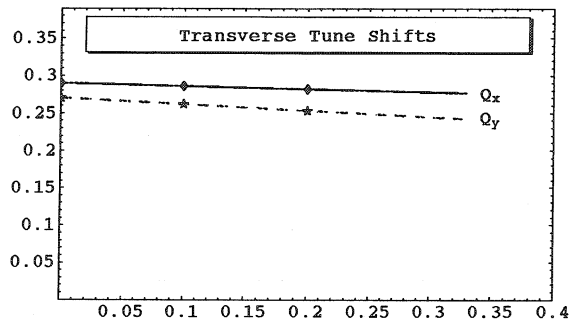

Figure 6.9: Horizontal and vertical tune as function of the beam current.

The slope of the horizontal and vertical tune with values of $\Delta Q_x/\Delta I = 0.036/\text{mA}$ and $\Delta Q_y/\Delta I = 0.08/\text{mA}$ is only about half of the values measured in LEP ($\Delta Q_x/\Delta I = 0.07/\text{mA}$, $\Delta Q_y/\Delta I = 0.135/\text{mA}$), but depend on the number of turns averaged. However the ratio of horizontal to vertical tune is approximately the same as the one measured. A part of the difference between the simulation and measurement is probably due to the neglect of the resistive wall impedance, which causes a large tune shift of the m=0 mode, but has only a moderate effect on the transverse mode coupling threshold. Furthermore, since the effect of the quadrupole wake component depends on the transverse offset of the beam from axis, another part of the difference might be due to unavoidable closed orbit errors in the machine which are not included in the simulation.

Chapter 7

Conclusions

The behaviour of particle motion is studied usually only in the longitudinal and one of the transverse dimensions. The extension to 3 dimensions requires a much more complicated description. New effects such as coupling of the motion in the 2 transverse planes have to be included. This occurs due to axially non-symmetric structures. Their usual replacement with symmetric structures, for which the wake fields can be computed much more easier is not always a sufficient approximation.

The 3-dimensional multi-particle tracking program TRISIM3D was developed. As in its 2-dimensional predecessor TRISIM, triangular shaped basis functions are used to describe the changing bunch shapes in the accelerator. The wake potential tables, used as input for TRISIM3D, have been precalculated for triangles of 10 and 20 ps length.

The minimum bunch length for which wake potentials of LEP structures can be computed with the 3-D mesh program MAFIA on the CERN computers, was limited to bunches of 5 mm r.m.s. length. Therefore a novel method was developed to construct wake potentials of shorter Gaussian and triangular bunches from longer Gaussian ones. The accuracy of this *decomposition method* was found to be excellent, when the parameters are chosen correctly. The agreement with directly computated wake potentials is within a few percent.

The main transverse wake field components of non-axially symmetric structures are the quadrupole and the dipole component. The latter is only proportional to the offset of the exciting bunch, while the first one scales with the displacement of the trailing particle.

The shielded bellows and separators in LEP were investigated intensively. The slots between the sliding finger contacts of the bellows were found to have no

strong influence on the wake potentials for the bunch length of $1 - 2$ cm used in LEP. The cross-terms which introduce coupling between the two transverse planes were found to be rather weak. Therefore their effect in LEP was found to be small in TRISIM3D. Nevertheless such effects could play an important role in high intensity accelerators.

The limitations of computer resources, although steadily improving, do not allow the computation of wake fields in large accelerator structures due to bunches as short as actually used. The newly developed *decomposition method* permits the extension of the results obtained with longer bunches to shorter ones. Although the high frequency information is not obtained in this manner, it is not required when the wakes are used in the expansion of longer bunches.

Bibliography

[A+97] G. Arduini et al. "Parasitic Energy Loss in the LEP Superconducting Cavities". Technical Report CERN-SL-97-34 (AP), CERN, 1997.

[Bra84] D. Brandt. "SIMTRAC - A Simulation Program for Tracking Longitudinal and Transverse Single-Bunch Effects". Technical Report LEP-Note 512, CERN, 1984.

[Brü96] O. S. Brüning. " ZBASE User's Guide Version 1.1, An Impedance Data Base Program ". Technical Report CERN-SL-96-69 (AP), CERN, 1996.

[BW80] K. Bane and P. Wilson. "Longitudinal and Transverse Wake Potentials at SLAC". In *Proc. of the 11th International Conference on High Energy Accelerators.* CERN, 1980.

[BZ82] D. Brandt and B. Zotter. "Calculation of the wakefield with the optical resonator model". Technical Report CERN-ISR/TH/82-13, CERN, 1982.

[Cha93] A.W. Chao. *"Physics of Collective Beam Instabilities in High Energy Accelerators".* John Wiley & Sons Inc., 1993.

[Chi94] Yong Ho Chin. "User's Guide for ABCI, Version 8.7, (Azimuthal Beam Cavity Interaction)". Technical Report CERN-SL/94-02 (AP), CERN, 1994.

[CST96] CST, Computer Simulation Technology . *"MAFIA Version 3.2 User's Guide".* CST, Darmstadt, Germany, 1996.

[Gro90] Los Alamos Accel. Code Group. "Computer Codes for Particle Accelerator Design and Analysis: a Compendium". Technical Report 90-1766, LANL Report LA-UR, 1990.

[Kei72] E. Keil. "Diffraction radiation of charged rings moving in a corrugated cylindrical pipe". *Nuclear Instruments and Methods*, 100(419), 1972.

[KZ97] S. Kheifets and B. Zotter. *"Impedances and Wakes"*. World-Scientific Publishing Co., 1997.

[Mei97] O. Meincke. "Wake Potential Expansion using Gaussian Basis Functions". Technical Report CERN-SL/97-08 (AP), CERN, 1997.

[NS79] G. Nassibian and F. Sacherer. "A Method for Measuring Transverse Coupling Impedance". *Nuclear Instruments and Methods 159*, pages 21–27, 1979. also Report CERN-ISR-TH 77-61.

[Nys87] V. Nys. "Computer Simulation of a transverse single bunch instablility". Technical Report LEP-TH/87-35, CERN, 1987.

[RS94] J. Rossbach and P. Schmüser. "Basic course on accelerator optics". In S. Turner, editor, *CERN ACCELERATOR SCHOOL- Fifth general accelerator physics course1994*. CERN-94-01,Vol1, 1994.

[Sab94a] G. Sabbi. *"Studio dell'Interazione Fascio-Struttura in Macchine Acceleratrici Circolari"*. PhD thesis, University of Genoa, 1994.

[Sab94b] G. Sabbi. "TRISIM User's Guide". Technical Report CERN-SL/94-73 (AP), CERN, 1994.

[Sab95a] G. Sabbi. "Simulation of Single-Bunch Collective Effects in LEP by Linear Expansion of the Distribution Moments". Technical Report CERN-SL/95-25(AP), CERN, 1995.

[Sab95b] G. Sabbi. "TRISIM Version 2 User's Guide". Technical Report CERN-SL/95-124(AP), CERN, 1995.

[Wan90] T.S. Wang. "HERSIM2". Technical Report SL/90-08, CERN, 1990.

[WE96] C. Wyss (Editor). "LEP DESIGN REPORT VOL.III LEP2". Technical Report CERN-AC/96-01(LEP2), CERN, June 1996.

[WZ89] T. S. Wang and B. Zotter. "An Expansion Method for Calculating Wake Potentials". Technical Report CERN/LEP-TH/89-75 Rev., CERN, 1989.

[Zot93] B. Zotter. "Improved Equations of Motion for Multi-Particle Simulation". Technical report, CERN, 1993.